

**Department of Physics and Astronomy  
Heidelberg University**

Bachelor Thesis in Physics  
submitted by

**Kim Melanie Weiskopf**

born in Frankfurt (Germany)

**2022**

---

# **A theoretical model to predict the behaviour of resonant outward migration of two planets**

This Bachelor Thesis has been carried out by Kim Melanie Weiskopf at the  
Institute for Theoretical Astrophysics (ITA) in Heidelberg  
under the supervision of  
Prof. Cornelis P. Dullemond

---

## Abstract

Studies of protoplanetary disks have shown that planets interact with the disk, which leads to planetary migration. In a system with several planets, planets may be locked into resonance which allows them to migrate together. This work focuses on the outward migration of two resonantly locked planets, which follows the Masset and Snellgrove mechanism. This thesis examines where and if the planets stop migrating. For this, a theoretical model is provided, which considers the exerted torques onto the planets and the gap they open. The validity of this model is tested by comparing the results from the theoretical approach to hydrodynamical simulations with FARGO3D.

## Zusammenfassung

Beobachtungen von protoplanetaren Scheiben haben gezeigt, dass die Planeten in diesen mit der Scheibe interagieren und dadurch migrieren. In einem System mit mehreren Planeten ist es möglich, dass diese durch eine Resonanz gekoppelt sind und dann gemeinsam migrieren. Dieser Migrationsmechanismus wird beschrieben durch den Masset und Snellgrove Mechanismus. In dieser Arbeit wird die Frage, wann und ob die Planeten ihre Migration stoppen, untersucht. Dafür wird ein theoretisches Modell vorgestellt, welches die Berechnung der Drehmomente nutzt und die von den Planeten erzeugte Lücke, berücksichtigt. Die Validität dieses Modells wird getestet, indem es mit hydrodynamischen Simulationen verglichen wird, welche mit dem Programm FARGO3D durchgeführt werden.

# Contents

<b>1</b>	<b>Introduction</b>	<b>6</b>
<b>2</b>	<b>Theoretical Background</b>	<b>9</b>
2.1	Protoplanetary disks . . . . .	9
2.2	Hydrodynamic . . . . .	12
2.3	Migration . . . . .	13
2.3.1	The Lindblad resonance Locations . . . . .	14
2.3.2	Expression for the Torque . . . . .	19
2.3.3	Type I migration . . . . .	21
2.3.4	Type II migration . . . . .	22
2.3.5	Type III migration . . . . .	23
2.4	Migration of two planets . . . . .	23
2.4.1	Migration jumps . . . . .	24
2.5	Gaps . . . . .	25
2.5.1	The formation of gaps . . . . .	25
2.5.2	Gaprofile of Kanagawa et al 2017 . . . . .	26
<b>3</b>	<b>Python code of the theoretical approach</b>	<b>29</b>
3.1	Calculation of the total Torque exerted on the Planets established by the author . . . . .	29
3.1.1	Calculation of the Lindblad resonance locations in Python . . . . .	29
3.1.2	Calculations of the net torques in Python . . . . .	31
3.1.3	Migration rate calculation in Python . . . . .	32
<b>4</b>	<b>FARGO3D code and setups</b>	<b>34</b>
4.1	The FARGO3D code . . . . .	34
4.1.1	Smoothing of the planet potential . . . . .	35
4.1.2	Boundary conditions . . . . .	37
4.2	Setup ( <i>BM08</i> )theory . . . . .	38

## CONTENTS

---

<b>5 Results</b>	<b>40</b>
5.1 Setups <i>theory</i> . . . . .	40
5.1.1 Comparison of the general outcome of migration . . . . .	40
5.1.2 Comparison of the migration rates . . . . .	53
5.2 Setups <i>BM08theory</i> . . . . .	60
5.2.1 Comparison of the general outcome of migration . . . . .	60
5.2.2 Comparison of the migration rates . . . . .	69
<b>6 Discussion and Outlook</b>	<b>76</b>
6.1 Migration behavior . . . . .	76
6.2 Migration rate at one locations . . . . .	78
<b>7 Summary</b>	<b>82</b>
<b>8 Appendix A</b>	<b>84</b>
<b>9 Appendix B</b>	<b>85</b>
<b>10 Appendix C</b>	<b>86</b>
<b>11 Acknowledgements</b>	<b>93</b>

# Introduction

Humanities's interest in astronomy can be traced back many thousand years. Star formations were not only fundamental for orientation at sea, but also acquired religious symbolism. Besides the stars, also some planets of our own solar system, namely Mercury, Venus, Mars, Jupiter and Saturn, are visible to the naked eye and have been studied for millennia. While observing our own solar system, the question arose if there were more planetary systems in the universe. The Italian philosopher Giordano Bruno was one of the first to suggest this in the 16th century [Goetz, 1991]. The continuous evolution in technology, and science as a whole, resulted in the first confirmed detection of an exoplanet in 1992. Wolszczan and Frail [1992] describes three planets surrounding the pulsar named Lich, or PSR B1257+12. The planet 51 Pegasi b was discovered soon after in 1995 as the first planet around a sun-like star [Mayor and Queloz, 1995]. They can be considered the first breakthroughs which led to more planetary systems discoveries and the enhancement of methods to find and characterise them. As of the 8<sup>th</sup> September 2022, 3.808 confirmed planetary systems are known, as shown by Schneider [1995].

Today it is possible to observe planetary systems which are still forming. The Atacama Large Millimeter/Submillimeter Array (ALMA) is used to obtain images of disks. The spectral window from millimeter to centimeter allows the observation of disk dynamics, temperatures and the spatial distribution [Paardekooper et al., 2022]. A few images of ALMA are shown in Fig. 1.1. The observed systems consist of one or several stars and a surrounding disk, the protoplanetary disk, in which planets may be created. The examination of some systems in which large planets with masses of at least one Jupiter were found a few dozen astronomical units away from the central star posed questions. One would expect that the formation of those planets at these distances is not possible due to too long dynamical and accretion timescales. Examples are PDS70 and HR 8799, where the in situ formation models of the planets fail the main hypothesis. Those systems suggest that through gravitational interaction and exchange of angular momentum, planets are able to move within the disk, which is called *planetary migration*, or short: *migration*.

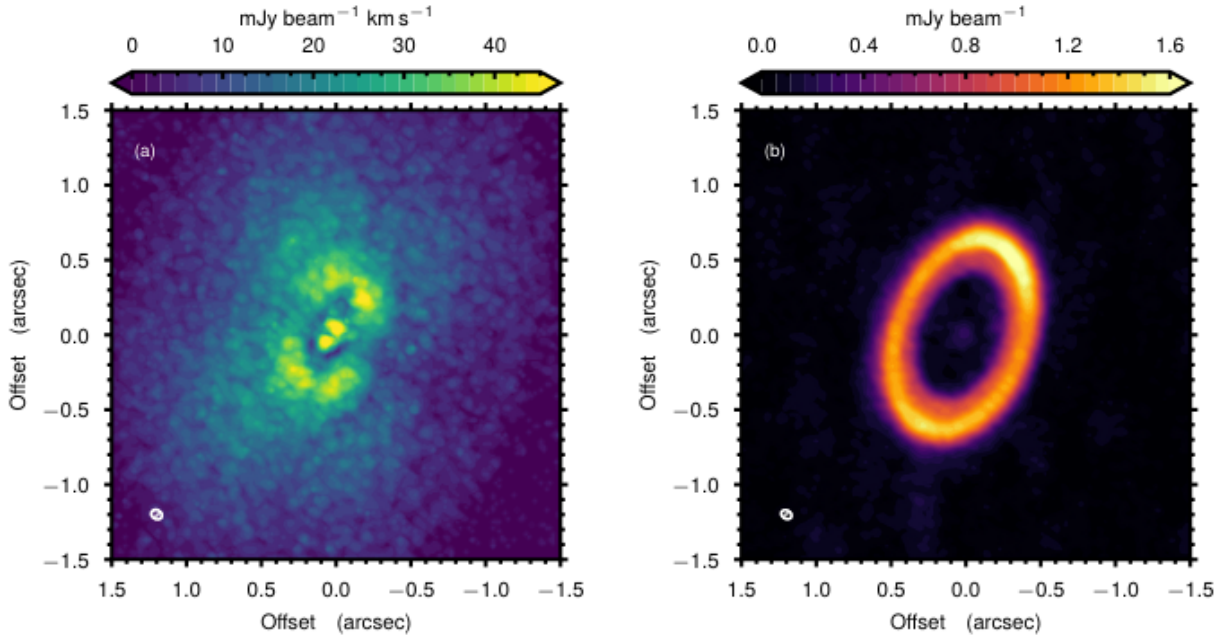


Figure 1.1: ALMA observations of the system PDS70. Observations done of  $^{12}\text{CO}$  (left) and the 350.6 GHz continuum (right) [Keppler et al., 2019]

The evolution and interaction of planets in protoplanetary disks can be examined and simulated by means of hydrodynamical simulations. FARGO3D [Benítez-Llambay and Masset, 2016] is a publicly available program to conduct these simulations. It is the successor of FARGO [Masset, 2000], which is also a public program for hydrodynamic simulations as well. The newer version FARGO3D is used for this thesis, since it is capable of running on a graphics processing unit (GPU), which is faster and more efficient than running on CPUs. Most migrating planets move towards the star [Kley and Nelson, 2012], but this may change for a coupled system of two planets which migrate together. Such systems containing two large planets with a more massive inner planet and a less massive outer planet follow the Masset and Snellgrove mechanism [Masset and Snellgrove, 2001], which gives a possible explanation of how and why planets migrate outwards. The mechanism was tested in various papers including Pierens and Raymond [2011], Crida et al. [2009] and Rometsch et al. [2020] just to name a few. The question which then arises is: when will the planets stop migrating outward and will their position this far away from the star remain stable? The objective of this thesis is to provide a theoretical model to estimate the torque exerted on the planet, and the migration rates, in order to propose an estimate of the stopping point of the migration. Such a framework would have the additional benefit of enabling an estimation of the migration rates and the direction without the use of hydrodynamics simulations. Especially the application on observed protoplanetary disks with two planets could be used to predict if and how much the system will change in the future.

The validity of the theoretical model will be tested using simulations done with FARGO3D.

[Chapter 2](#) provides the theoretical background of protoplanetary disks and planetary migration. Afterwards in [chapter 3](#) the derived theoretical approach is explained and implementation details are described. In [chapter 4](#) the setups of the FARGO3D code are listed and explained. The results are presented in [chapter 5](#) and discussed in [chapter 6](#). Finally the conclusions are summarised in [chapter 7](#).

# Theoretical Background

The sections in this chapter follow Armitage [2009], Dullemond and Springel [2012/13] and Dullemond [2013] closely. Without other citation, the information was taken from these works. Please note is that the overall physical background can't be illustrated here as it would go beyond the scope of this thesis, therefore the author will only present the most important and relevant aspects.

## 2.1 Protoplanetary disks

Protoplanetary disks come into existence after the creation of a star. Stars form out of dense, irregular, rotating and cold molecular clouds. Clumps may form and if they reach a critical mass, they collapse under their own gravity. Due to different factors like irregularity or rotation of the cloud, as well as the conservation of angular momentum, a rotating accretion disk forms around the newborn star. This disk is called the *protostellar disk*. It supplies more mass for the newborn star, and during the next  $10^5$  years most of that mass will fall onto the star due to 'turbulent viscosity'. What remains is a disk with  $M_{\text{disk}} \ll M_*$ , where  $M_*$  is the central stars mass. This disk is called the *protoplanetary disk*, in which planets may form. Protoplanetary disks are optically thick in their early years, which makes observations harder. In this optically thick state, in the disk radiative processes dominate. After 1-2 Myr the disk cools and changes to an isothermal behaviour. Additionally the distance from the star also determines if a region in the disk shows an isothermal behaviour. The further away from the star, the faster cooling is compared to the orbital timescale<sup>1</sup>, the better the assumption of a locally isothermal disk. Thus assuming a locally isothermal<sup>2</sup> disk only assumes, that the disk is in a later stage of its evolution [Pierens and Raymond, 2011] or the looked at region is far away from the star. Due to the low temperatures, dust can survive in the disk besides the gas. During its lifetime, the disk mass is usually a lot smaller than the central star mass. Because of that, the argument can be made, that the disks self-gravity can be neglected. Furthermore, the disk loses its

---

<sup>1</sup>The time an object needs for an orbit

<sup>2</sup>an equation of state where the disk temperature is set and kept fixed, usually as a function of  $r$

mass through accretion of the central star in the next  $10^7$  years.

Observations of protoplanetary disk show geometrically thin disks, meaning the disk pressure scale height is much smaller than the radius  $H \ll r$ , which is also a direct consequence of the low temperature and the consequently low disk pressure. The ratio of  $H$  and  $r$  is the aspect ratio  $h \equiv H/r$ .

The exchange of angular momentum and the orbital motion are the main causes for dynamics in the disk. The angular momentum of the gas is given by:

$$l = \Omega r \quad (2.1)$$

with the orbital frequency  $\Omega$ . For a Keplerian disk  $\Omega \approx \Omega_K$  with the Keplerian frequency

$$\Omega_K = \sqrt{\frac{GM_*}{r^3}} \quad (2.2)$$

Together, Eq. (2.1) and Eq. (2.2) show, that when gas moves towards the star, it loses angular momentum while it gains angular momentum when moving away from the star. There are two main mechanism, which explain the angular momentum distribution since it's a conserved quantity. In the viscous disk model, the angular momentum gets redistributed whereas it also can be acquired by material entangled in either photoevaporative or magnetically driven winds. In this thesis, a viscous disk model is used.

## Viscous disk structure

A viscous disk assumes a viscous gas, where the viscosity is high enough to dominate accretion through the disk. One distinguishes between the gas molecular viscosity and its turbulent viscosity. The first is generated by collision of gas particles but is too small to be the main source of angular momentum redistribution, because it is too low to explain the observed mass accretion rates. The other arises from the turbulence within the disk and contributes largely to a change of the angular momentum distribution within the disk. It is common to adapt the  $\alpha$ -model of the turbulent viscosity

$$\nu = \alpha \Omega H = \alpha \frac{c_s^2}{\Omega} \quad (2.3)$$

introduced by [Shakura and Sunyaev \[1973\]](#) with the effective disk thickness

$$H = \frac{c_s}{\Omega_K} \quad (2.4)$$

and  $c_s$  the gas sound speed:

$$c_s = \sqrt{\frac{T(r)k_B}{\mu m_p}}. \quad (2.5)$$

Here,  $k_B$  is Boltzmann's constant,  $\mu$  is the mean molecular weight and  $m_p$  the proton mass. Note that Eq. (2.4) only is valid in geometrical thin disks. In that case the general orbital frequency  $\Omega$  will replace  $\Omega_K$ . The dimensionless parameter  $\alpha$ , which is a measure of the turbulent viscosities efficiency, can be chosen between 0.0001 and 0.1, but in newer studies  $\alpha$  is chosen to be on the lower side, as in [Rometsch et al. \[2020\]](#) and [Pierens and Raymond \[2016\]](#). The value of  $\alpha$  is usually chosen to be constant for convenience, but this is generally not the case. Furthermore, there could be non-turbulent regions in the disk where the description fails. The gap opening mechanism depends strongly on the viscosity and will be explained in section Sect. 2.5.1.

Based upon the assumption that the disk is locally isothermal the equation of state is:

$$P = c_s^2 \rho \quad (2.6)$$

with the isothermal soundspeed  $c_s$ .

### Radial disk structure

Considering a radial gas distribution, the surface density  $\Sigma(r)$  is assumed to follow a power law:

$$\Sigma(r) \propto r^p \quad (2.7)$$

as well as the temperature  $T(r)$

$$T(r) \propto r^q. \quad (2.8)$$

Then the soundspeed and the aspect ratio can be parameterised with  $r$ :

$$c_s \propto r^{(p-3/2)/2}, \quad h \propto r^{(-q+1)/2} \quad (2.9)$$

where  $p + q = -\frac{3}{2}$ . A realistic model would chose  $-3/4 < q < -1/2$  or an even steeper  $q$  and  $0 > p > -1.5$  [[Williams, Jonathan P. and Cieza, Lucas A., 2011](#)]. The accretion rate through the disk in equilibrium is

$$\dot{M} = 3\pi\Sigma\nu. \quad (2.10)$$

In a steady-state disk, this rate is constant.

### Vertical disk structure

The vertical structure is described by using the coordinate  $z$ . The vertical temperature profile is assumed to be isothermal, so that  $T$  does not change along  $z$ . Then the vertical density profile follows a gaussian

$$\rho(z) = \rho_0 \exp\left(-\frac{z^2}{2H^2}\right). \quad (2.11)$$

Using the definition of the surface density as the line integral of the density:

$$\Sigma(r) \equiv \int_{-\infty}^{+\infty} \rho(r, z) dz \quad (2.12)$$

Eq. (2.11) can be rewritten as:

$$\rho(z) = \frac{\Sigma}{H \sqrt{2\pi}} \exp\left(-\frac{z^2}{2H^2}\right) \quad (2.13)$$

## 2.2 Hydrodynamic

The disk's evolution is generally described by the hydrodynamic equations. The description of gas as an ideal fluid is used very often in astrophysics simulations. Here  $\vec{u}$  defines the velocity of the gas. The motion is described by the three conservation equations: the conservation of mass in tensor form

$$\partial_t \rho + \partial_i (\rho u_i) = 0 \quad (2.14)$$

the conservation of energy

$$\partial_t (\rho e_{tot}) + \partial_k [(\rho e_{tot} + P) u_k] = 0 \quad (2.15)$$

and the conservation of momentum. Under the assumption that the disk is viscous, the conservation of momentum equation can be rewritten into the *Navier stokes equation*:

$$\partial_t (\rho u_i) + \partial_k (\rho u_i u_k + \delta_{ik} P - \sigma'_{ik}) = 0 \quad (2.16)$$

with the viscous stress tensor  $\sigma'_{ik}$  which contains the shear and bulk viscosity. The latter is less important in astrophysics in general, because of the low gas density. Thus, the

gas bulk viscosity is negligible compared to the shear viscosity. Exchange of momentum perpendicular to the flow direction is possible due to viscosity, which acts as a force. This is very important for the disks dynamical evolution.

## 2.3 Migration

Large planets form beyond, but not too far beyond, the ice line, where condensation of water rich materials is possible due to the cold temperatures. The ice line's location in the disk is heavily dependent on the star-disk system properties but for a sun-like star it is located around 2.7 AU when planets start to form. The duration the formation is dependent on the disk's accretion and dynamical timescales at the formation location. The dynamical time scale is given by the orbital period. The accretion time scale  $t_{\text{acc}} = M/\dot{M}$  gives the time it would take to accrete a certain mass with a certain accretion rate [Glover, 2017]. Planetary systems were observed which contain very massive planets at locations far away from the central star which exceed the ice line location. At those radii, both timescales are too big for planet formation to be possible and can even exceed the disk's life time. Hence, it is assumed that the planets formed near the star and then migrated outwards.

The reason why planets are able to migrate within disk is due to the exerted torques which causes an exchange of angular momentum. Two torques are especially important in viscous disks: the Lindblad torques and the corotation torque. The Lindblad torques are exerted at the Lindblad resonance (LR) locations, where one armed spirals are created as wave-like responses of the disk [Paardekooper et al., 2022]. At LR locations the gas has a Doppler shifted frequency<sup>3</sup>  $\omega = m(\Omega(r) - \Omega_p)$  which is equal to the natural disk oscillation frequency [Kley and Nelson, 2012]. This natural disk oscillation frequency is the epicyclic frequency  $\kappa$ . This leads to a strong response of the disk and gravitational coupling. Consequently torques are exerted at these locations. The corotation torque is exerted at the location where  $\kappa$  matches the planets orbital frequency. For the basic example of a planet on a circular orbit in a Keplerian disk, there is only one corotation resonance region, namely the gas which is located at the planet's radius and several additional Lindblad locations. For the migration of massive planets, the coorbital torque is not of importance, since they open a gap and empty their coorbital region.

The exact equations giving the LR locations and torque are dependent on the disk's proper-

---

<sup>3</sup>The Doppler-shifted frequency is the frequency of the perturbation by the planet, in a frame corotating with the gas at the radius  $r$ .

ties. Hence, more than one equation will be presented. The assumptions made in Goldreich and Tremaine [1980], Ward [1997] and Kley and Nelson [2012], which were used to retrieve the LR locations- and Lindblad torque equations, are:

- The sound speed of the gas  $c$  is constrained by  $c_s \ll \Omega r$ , otherwise this would lead to shocks. Also as it is observed in protoplanetary disks. It is equivalent to the assumption of a thin disk since  $h = c_s/(\Omega r)$
- The surface density  $\Sigma$  is constrained by  $G \Sigma \ll \Omega^2 r$ . Thus the disk makes a negligible contribution to the unperturbed gravity field and selfgravity can be neglected.

Furthermore Oort's parameter  $A(r)$ ,  $B(r)$  and the squared epicyclic frequency  $\kappa(r)^2$  are defined by:

$$\kappa(r)^2 \equiv \frac{1}{r^3} \frac{d}{dr} [r^2 \Omega(r)]^2 = 4B(r) \Omega(r) \quad (2.17)$$

$$A(r) \equiv \frac{r}{2} \frac{d\Omega(r)}{dr} \quad (2.18)$$

$$B(r) \equiv \Omega(r) + A(r) \quad (2.19)$$

which are used in the next section.

### 2.3.1 The Lindblad resonance Locations

The most general way to attain the LR locations is to expand the planet's perturbation potential  $\phi^p$ <sup>4</sup> in a Fourier Series:

$$\phi^p(r, \theta, t) = \sum_{l=-\infty}^{\infty} \sum_{m=0}^{\infty} \phi_{l,m}^p(r) \cos \{m\theta - [m\Omega_p + (l-m)\kappa_p] t\}. \quad (2.20)$$

The largest term of  $\phi_{l,m}^p$  scales with  $e^{|l-m|}$  for  $e \ll 1$ . Then the pattern speed of the  $l^{th}$  and  $m^{th}$  component is given by

$$\Omega_{l,m} = \Omega_p + \frac{(l-m)}{m} \kappa_p = \Omega(r) + \varepsilon \frac{\kappa(r)}{m} \quad (2.21)$$

as presented in Goldreich and Tremaine [1980]. Here  $\kappa_p$  is the epicycle frequency and  $\varepsilon = 1(-1)$  for the outer(inner) LR. Due to the dependency of  $\phi_{l,m}^p$  on  $e$ , LR are contributing to an eccentricity growth while corotation resonances contribute to an eccentricity damping. The value of  $m$  has to be an integer and is restricted depending on the value of

---

<sup>4</sup>It is the perturbation of the central star's potential due to a planet with mass  $M_p$  in the disk

$l$  and whether the locations belong to the inner or outer LR. For  $l = m$  the values of  $m$  are restricted to,  $m > 1$  for inner LR and  $m \geq 1$  for outer LR.  $l = m+1$  gives inner LR and the condition  $m > 1$  still holds. For the outer LR with  $l = m-1$ ,  $m$  also has to be larger than 1.

Within the limitation of very small eccentricities, higher orders of  $l$  can be neglected and only  $l = m$  is used. This is often applied in papers as part of idealised orbits. Assuming  $e = 0$  and neglecting the disk pressure, the  $m^{th}$  Lindblad resonances occur where

$$D = \Omega(r) - \Omega_p + \varepsilon \frac{\kappa(r)}{m} = 0 \quad (2.22)$$

[Kley and Nelson, 2012].

Considering the disk pressure, the resonance locations are shifted away from the locations received from  $D$ . Two different expressions for the shifted resonances are presented:

First, Ward [1997] derived:

$$\kappa^2 - m^2 [\Omega(r) - \Omega(r_p)]^2 + \left( \frac{m^2 c_s^2}{r^2} \right) = 0 \quad (2.23)$$

$$\Omega^2 = \Omega_K^2 - (k + l) \frac{c_s^2}{r^2} \quad (2.24)$$

where  $c_s$  is the isothermal gas sound speed and  $\kappa \approx \Omega$ . The parameters  $k$  and  $l$  are defined by:

$$k \equiv -\frac{d \ln \Sigma}{d \ln r}, \quad l \equiv -\frac{d \ln T}{d \ln r} \quad (2.25)$$

If the temperature and surface density are given by power laws, then  $k = -p$  and  $l = -q$  with  $q, p$  defined in Eq. (2.1). While Eq. (2.23) corrects the effects of the gas pressure on the natural oscillation frequency, Eq. (2.24) corrects the pressure effect on the orbital frequency. Eq. (2.24) will be inserted in Eq. (2.23), which will be further referenced as  $D_{*,p}$ . For the sake of argument, Eq. (2.24) will also be inserted in Eq. (2.22), which will now be named  $D_p$ .

Lastly, Kley and Nelson [2012] proposed an equation which considers the disk pressure completely, which only uses parts of  $D_{*,p}$  as presented above, namely Eq. (2.23). To keep a clear structure, Eq. (2.23) will now be referred to  $D_K$ . All the used LR locations and the assumptions they fulfil are listed in Table 2.1.

Table 2.1: List of LR location equation abbreviations

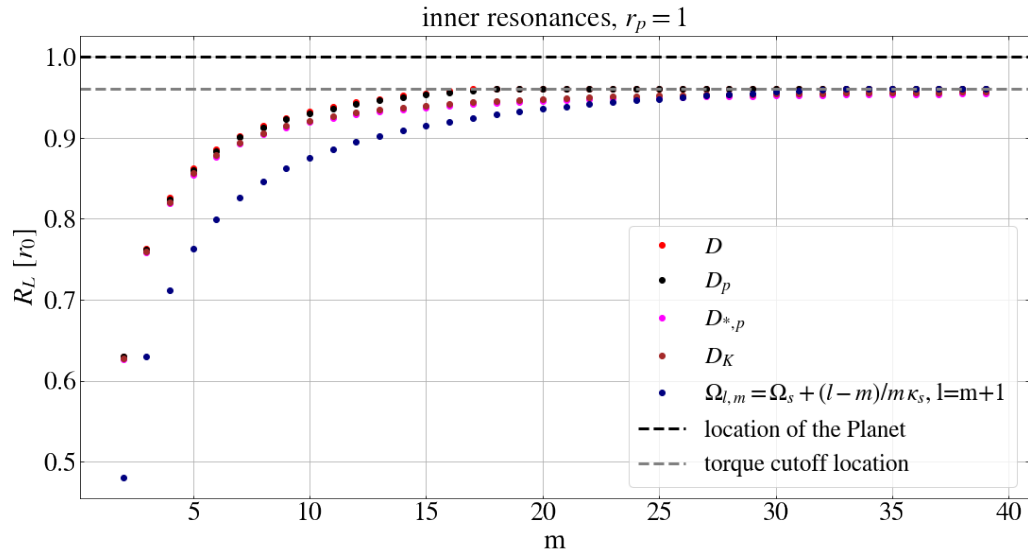
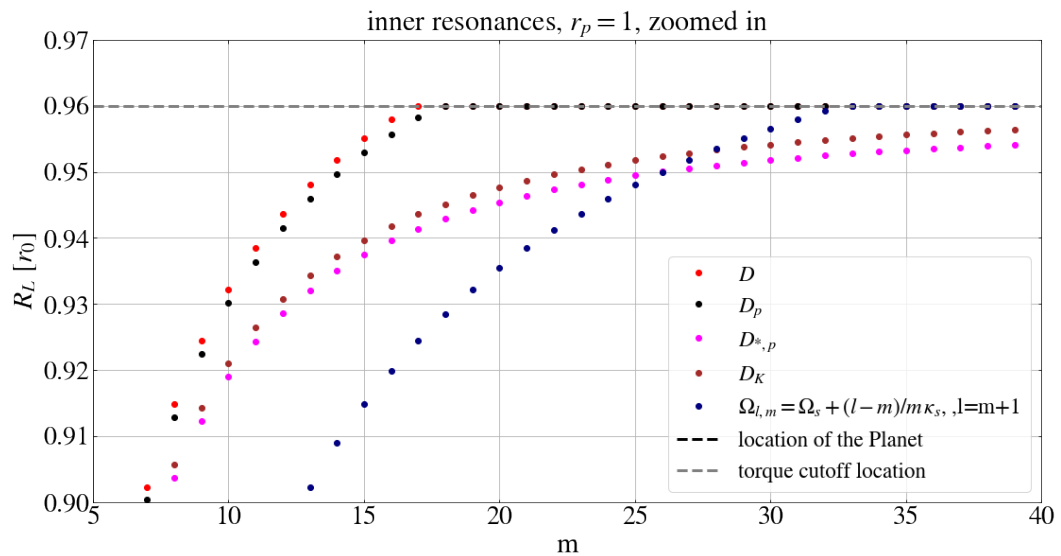
Name	physical assumptions
$D$	Keplerian disk, does not consider disk pressure
$D_p$	no Keplerian disk, does only consider the pressure effect on the orbital frequency
$D_K$	Keplerian disk, does only consider the pressure effect on the natural oscillation frequency
$D_{*,p}$	no Keplerian disk, considers the pressure effect on the orbital frequency and the natural oscillation frequency

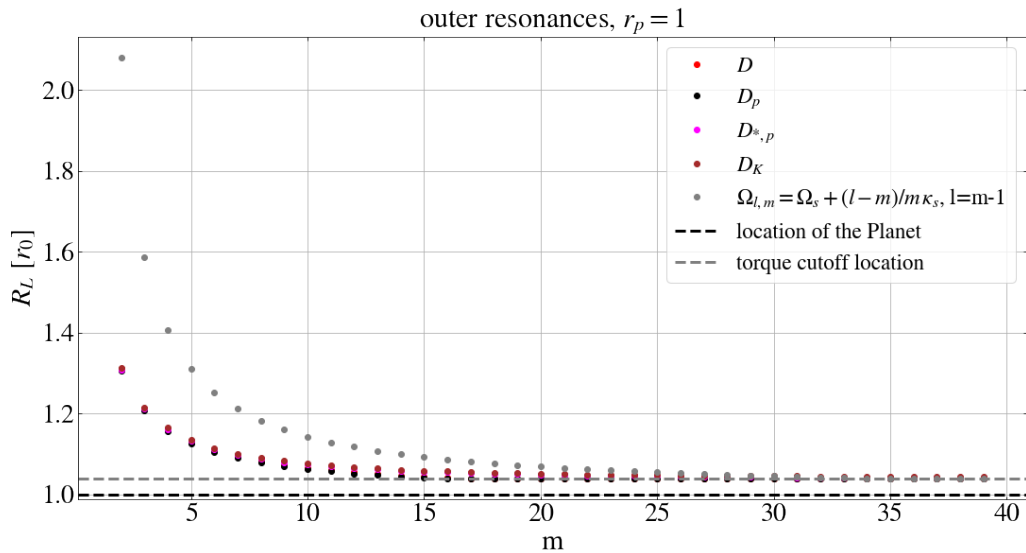
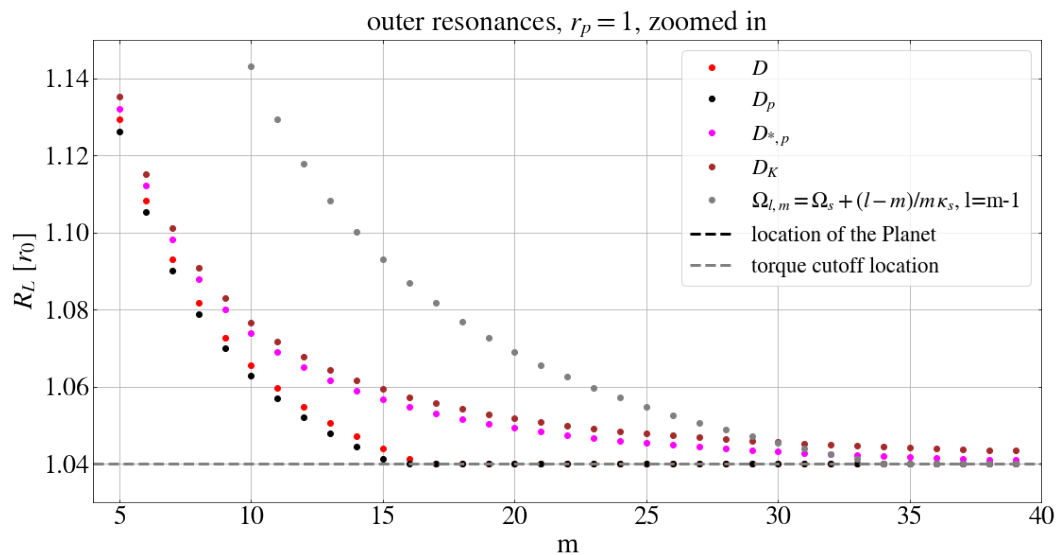
Even though,  $D$  and  $D_{*,p}$  are the most coherent LR locations,  $D_p$  and  $D_K$  will also be analysed to examine the effects of the partial corrections due to the disk pressure. The usage of  $D$  will enable to give an estimate how much the missing disk pressure effects the results.

In theory, some of the presented resonance locations could get arbitrarily close to the planet, especially the ones resulting from  $D$  when assuming a Keplerian disk. A cutoff radius, where the locations accumulate for  $m \gg 1$  was derived in [Goldreich and Tremaine \[1980\]](#):

$$r_{\text{cutoff}} = r_p \pm \frac{2}{3}H \quad (2.26)$$

This is will be considered by restricting the locations of resonances to be at least  $2/3 H$  away from the planet. Lastly it should be mentioned that the self-gravity of the gas is never taken into account. To visualise the varying proposed LR locations, they were plotted for  $r_p = 1$  which is shown in Fig. 2.1 to Fig. 2.4. The exact calculation will be explained in Sect. 3.1.1.


 Figure 2.1: Different inner LR locations in dependence of  $m$ 

 Figure 2.2: Different inner LR locations in dependence of  $m$  zoomed in

Figure 2.3: Different outer LR locations in dependence of  $m$ Figure 2.4: Different outer LR locations in dependence of  $m$  zoomed in

### 2.3.2 Expression for the Torque

Next the different expressions for the Lindblad torque found in different literature are presented. Additionally it is explained if and how the different expressions correlate and what assumptions were made in their derivation.

#### Torque expression derived in Goldreich and Tremaine 1979

The equation from [Goldreich and Tremaine \[1980\]](#) uses the Fourier components  $\phi_{l,m}^p$  of the planets gravitational perturbation potential in Eq. (2.20) as derived in [Goldreich and Tremaine \[1979\]](#). The coefficients to first order in  $e$  are:

$$\phi_{m,m}^p = -\frac{GM_p}{2a} (2 - \delta_{m,0}) (b_{1/2}^m - f\alpha_r \delta_{m,1}) \quad (2.27)$$

$$\phi_{m+1,m}^p = -\frac{GM_p}{2a} e (2 - \delta_{m,0}) \left[ \left( \frac{1}{2} + \frac{m\Omega_p}{\kappa_p} + \frac{\alpha_r}{2} \frac{d}{d\alpha_r} \right) b_{1/2}^m - f\alpha_r \left( \frac{3}{2} - \frac{2B_p}{\Omega_p} + \frac{\Omega_p}{\kappa_p} \right) \delta_{m,1} \right] \quad (2.28)$$

$$\phi_{m-1,m}^p = -\frac{GM_p}{2a} e (2 - \delta_{m,0}) \left[ \left( \frac{1}{2} - \frac{m\Omega_p}{\kappa_p} + \frac{\alpha_r}{2} \frac{d}{d\alpha_r} \right) b_{1/2}^m - f\alpha_r \left( \frac{3}{2} - \frac{2B_p}{\Omega_p} - \frac{\Omega_p}{\kappa_p} \right) \delta_{m,1} \right] \quad (2.29)$$

Here,  $\alpha_r \equiv \frac{r}{r_p}$  and  $f \equiv \frac{\Omega_p^2 a^3}{GM_*}$ . The Laplace coefficients  $b_{1/2}^m(\alpha_r)$  is defined by:

$$b_{1/2}^m(\alpha_r) \equiv \frac{2}{\pi} \int_0^\pi \frac{\cos m\theta d\theta}{\sqrt{1 - 2\alpha_r \cos \theta + \alpha_r^2}} \quad (2.30)$$

for  $\alpha_r \neq 1$  ([Ward \[1997\]](#) sometimes misprinted  $\alpha_r$  as  $\alpha$ ).

The torque given for general  $l$  and  $m$  is:

$$\Gamma_{l,m}^L = -m\pi^2 \left[ \Sigma \left( \frac{rdD}{dr} \right)^{-1} \left( \frac{rd\phi_{l,m}^p}{dr} + \frac{2\Omega}{\Omega - \Omega_{l,m}} \phi_{l,m}^p \right)^2 \right]_{r_L} \quad (2.31)$$

This torque will now be named GT79. Furthermore, [Goldreich and Tremaine \[1980\]](#) points out the importance of the condition  $m \ll \frac{\Omega r}{c} = \frac{1}{h}$  with the aspect ratio  $h$ . Violating this condition leads to an interference of density waves on both sides of the planet's vicinity.

Since a flared disk is used in this work, given by

$$h = \frac{H}{r} = h_0 \left( \frac{r}{r_0} \right)^\beta \quad (2.32)$$

with the flaring index  $\beta > 0$ , effectively only the torques of  $m=1$  or/and  $m=2$  can be used. Thus GT79 is not suitable to calculate the torque with the given conditions proposed by Goldreich and Tremaine [1979]. But merely out of interest, GT79 is used to calculate the torque, in order to see how inaccurate the result due to the violation of  $m \ll \frac{\Omega r}{c} = \frac{1}{h}$  is. The exact torque calculation is presented in Goldreich and Tremaine [1980], but exceeds the scope of this thesis.

### Torque expressions in Ward 1997

The following torque expression derived in Ward [1997] is a generalised version of GT79:

$$\Gamma_m = \frac{\pi^2 m \Sigma \Psi_m^2}{r dD_{*,p}/dr} \quad (2.33)$$

with the function

$$\Psi_m = \frac{rd\phi_m/dr + 2mf\phi_m}{\sqrt{1 + 4\xi^2}} \quad (2.34)$$

Here  $\phi_m$  is the amplitude of the  $m^{th}$  order Fourier component of the disturbing function:

$$\phi_m = -\frac{GM_p}{r_p} b_{1/2}^m(\alpha_r) \quad (2.35)$$

This is equal to Eq. (2.27) for  $m \neq 1$ . This torque will be named Ward3.

Ward [1997] then continues to further simplify Ward3, resulting in:

$$\Gamma_m = \varepsilon \frac{4}{3} \mu^2 (\sum r_p)^2 (r_p \Omega_p)^2 \frac{m^2 \alpha_r^{3/2} \psi^2}{q \sqrt{1 + \xi^2} (1 + 4\xi^2)} \quad (2.36)$$

with

$$\psi = \frac{\pi}{2} \left[ \frac{1}{m} \left| \frac{db_{1/2}^m(\alpha_r)}{d\alpha_r} \right| + 2\sqrt{1 + \xi^2} b_{1/2}^m(\alpha_r) \right] \quad (2.37)$$

and

$$q(\xi) = 1 - \varepsilon \frac{(1-l)h}{3\alpha_r^{3/2}} \frac{\xi}{\sqrt{1 + \xi^2}} \quad (2.38)$$

where  $\xi = mc_s/(r\kappa)$ . The torque in Eq. (2.36) will now be named Ward8. Here, the disk

pressure is taken into consideration. In addition, a nearly Keplerian disk is assumed. The two torque expressions lead to different results, hence both will be used in the further analysis. This also provides the opportunity to evaluate the simplification of Ward3.

Since the different locations and expressions for the torque exerted by the LR were shown, the classical types of migration may be explained.

### 2.3.3 Type I migration

Low mass planets only interact weakly with the disk. Nevertheless, the torques emerging from them on the disk are strong enough to perturb the surface density, which results in spiral arms. These spiral arms are the same presented at the beginning of Sect. 2.3. While the gas is gravitationally coupled due to the relation

$$m(\Omega(r) - \Omega_p) = 0 \text{ or } \pm \kappa \quad (2.39)$$

there are two torque types. If Eq. (2.39) is equal to 0, then the (coorbital) corotation torque is exerted by the gas which passes the planet's corotation region. After passing by, the gas ends up on a different orbit [Masset, 2001]. Due to the change in radius, the gas lost or gained angular momentum and therefore the planet gained or lost angular momentum, too, since it is a conserved quantity. This gas can become trapped in the coorbital region, which is shown in Fig. 2.5. The corotational torque remains unsaturated due to the viscosity [Paardekooper et al., 2022]. If Eq. (2.39) is equal to  $\kappa$ , it results in the LR locations. At these LR locations, the Lindblad torque exerts onto the planet. Their values are usually bigger than the corotation torque, consequently the Lindblad torque's asymmetry mainly drives the migration. The sum of all torques onto the planet is given by

$$\Gamma_{\text{tot}} = \sum_{m=1}^{\infty} \Gamma_{\text{OLR}}(m) + \sum_{m=2}^{\infty} \Gamma_{\text{ILR}}(m) + \Gamma_{\text{CR}} \quad (2.40)$$

Planets that migrate within this mechanism have a fast migration rate and usually migrate inwards. Especially the corotation torque's contribution greatly influences the migration rate, which makes its contribution very important.

Saturn size planets may move within the disk according to Type I migration because they are still light enough to only create a partial gap and in consequence, don't clear out their coorbital region.

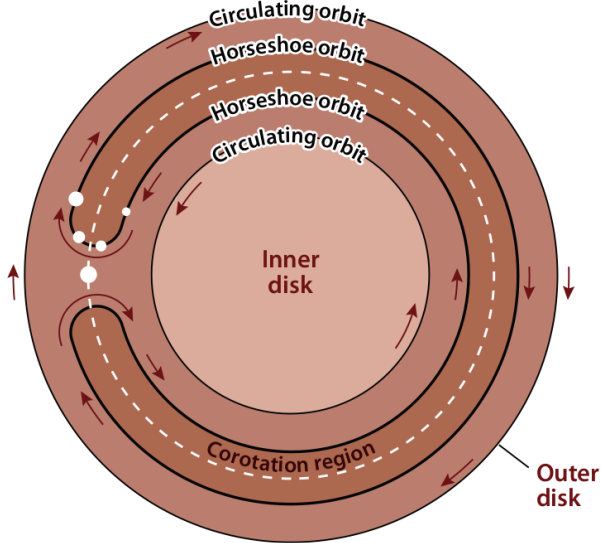


Figure 2.5: Schematic picture of the horseshoe region and the gas flow around the planet referring to the corotating frame. It divides the disk into three regions: the outer disk, the corotation/ horseshoe region and the inner disk. Gas trapped in the horseshoe region librates while gas in the outer and inner disk circulates. [Kley and Nelson, 2012]

### 2.3.4 Type II migration

Massive planets open a (deep) gap and couple themselves to the disk's viscous evolution, which means that they are locked inside their gap and evolve with it [Paardekooper et al., 2022]. Due to the existence of a gap only the Lindblad torques are exerted on the planet. The rate is given by:

$$\dot{a}_p = \frac{2 \Gamma_{LR,all}}{\Omega_p a_p (m_p - \delta m)} \quad (2.41)$$

[Kley and Nelson, 2012]. Here,  $\delta m$  is the "vorticity-weighted coorbital mass deficit" which can be approximated as the difference between the actual mass in the horseshoe-region and the fictitious mass in that region if the planets wouldn't perturb the disk. For Type II migration the condition  $m_p > \delta m$  hold, which when inserted into Eq. (2.41) leads to a damping of semi-major axis disturbances [Masset and Papaloizou, 2003]. As a consequence of the damping and the missing corotation torque, Type II migration is slower than Type I migration. The migration is usually towards the star in this regime, but can also be directed away from the star, depending on the disk's physical properties.

In the past few years, more works have shown that planets may migrate independently of their gap as well as gas may flow across the gap. The classical Type II migration could be replaced by the model proposed in Kanagawa et al. [2018], which is based on a more accurate gap structure. Nevertheless, the exact contents of Kanagawa et al. [2018] are

beyond the scope of this thesis.

### 2.3.5 Type III migration

The last migration regime is often referred to as "runaway migration", because of the extremely high migration rates. It occurs for planets which open a gap, but fulfill the condition  $m_p < \delta m$ . Then small semi-major axis perturbations are growing exponentially, as shown when inserting the condition in Eq. (2.41) [Masset and Papaloizou, 2003]. Runaway migration will slow down as soon as the horseshoe region loses mass during the migration, which leads to the decline of  $\delta m$ . For inward migration  $a$  is a declining function, therefore  $\delta m$  decreases, leading to a stall as well [Kley and Nelson, 2012]. This behaviour is very nonlinear.

## 2.4 Migration of two planets

There is also the possibility that two planets migrate together, which is very likely in a planetary system with several planets. If the planets are massive enough to open a gap, their behavior is described by the *Masset and Snellgrove mechanism*

The planets are gravitationally coupled due to the *mean motion resonance*. Their orbital periods given by Kepler's third law:

$$T = 2\pi \sqrt{\frac{r^3}{GM_*}} \quad (2.42)$$

have a ratio which fulfils:

$$\frac{T_{\text{inner}}}{T_{\text{outer}}} \simeq \frac{p}{p+q} \quad (2.43)$$

Then they are in a  $(p+q) : p$  mean motion resonance, where the planets exert a periodical gravitational force onto each other, allowing an exchange of angular momentum. Planets are in MMR if the resonance migration time is smaller than the resonance libration time [Kley and Nelson, 2012].

It is further assumed in this thesis that the more massive planet is closer to the star, as well as that they both open a deep gap before they start interacting with each other. The smaller planet will migrate inwards faster while the inner disk pushes the inner planet outwards, until they are resonantly locked. In Masset and Snellgrove [2001], the planets don't form a gap before they migrate and then the inner planet also migrates inwards,

but with a slower rate than the outer planet, until they are resonantly locked. Whether the assumption that the planets are not interacting when first forming a gap is valid, can be debated but is beyond the scope of this thesis. If their common gap is deep enough when they are resonantly locked, it results in the cutting of the inner, larger planets outer Lindblad resonance (OLR) and the outer, smaller planets inner Lindblad resonance (ILR). This is fulfilled if

$$\frac{\mu_{p,\text{outer}}}{\mu_{p,\text{inner}}} < \left( \frac{C_{\text{ILR}}}{C_{\text{OLR}}} \right)^{1/2} \left( \frac{p}{p+q} \right)^{1/3} \quad (2.44)$$

from [Masset and Snellgrove \[2001\]](#). All the simulations done for this thesis fulfil this condition for  $C_{\text{ILR}} = C_{\text{OLR}}$  and the more conservative approach  $C_{\text{ILR}} = 0.5 C_{\text{OLR}}$  for a 2:3 as well as a 2:1 MMR. Since the inner planet is more massive, the planets ILR will be larger than the outer planets OLR, leading to a net positive torque, starting outward migration. As gas flows through the gap, it gives its angular momentum to the planets, which further migrate outwards. (Without this gas flow, the migration would stall.) On the contrary, a more massive outer planet would lead to inwards migration.

Whether the assumption that the planets are not interacting when first forming a gap is valid, can be debated but is beyond the scope of this thesis.

### 2.4.1 Migration jumps

While two planets migrate outwards, a migration jump may occur. These jumps were first defined by [Rometsch et al. \[2020\]](#) and are characterised as follows. The outer of the two planets starts a rapid outward migration over a few thousand years. The planet may cover as much as a few dozen AU during this time, while the inner planet maintains its migration behaviour. The outer planet then stays in the region a few thousand years and afterwards migrates back inwards, also very rapidly. Eventually it catches up in MMR with the inner planet.

Migration jumps occur in [Rometsch et al. \[2020\]](#) in massive disk, where a system of two or more planets migrates outwards and vortexes form outside the gap. The combination of these conditions results in more eccentric planets, which is a precondition for rapid outward migration. This rapid outward migration seems to be self-enhancing, and likely falls into the Type III regime. An exemplary semi-major axis evolution is shown in Fig. 2.6.

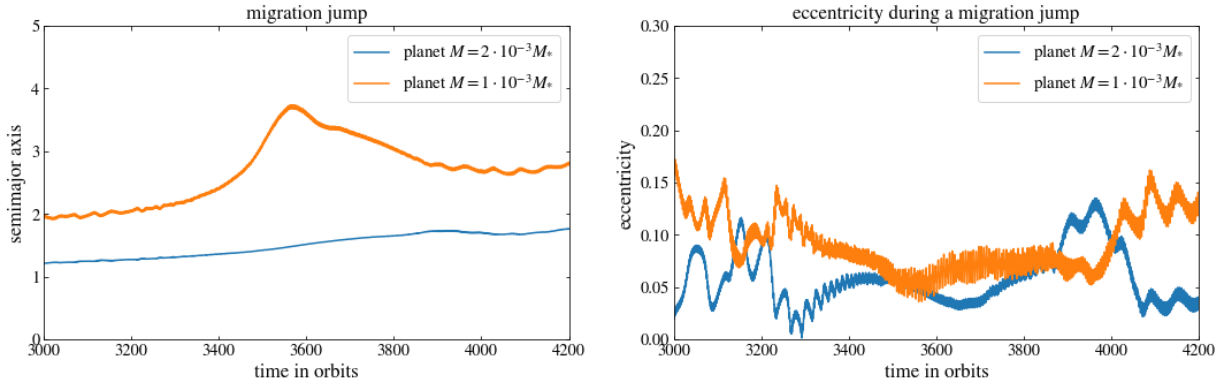


Figure 2.6: Semi-major axis and eccentricity evolution during a migration jump. The simulation was run with the parameters:  $M_{\text{inner}} = 2 \cdot 10^{-3} M_*$ ,  $M_{\text{outer}} = 1 \cdot 10^{-3} M_*$ ,  $\alpha = 10^{-3}$ , flaringindex = 0.25,  $\Sigma_0 = 10^{-3}$  and  $h_0 = 0.06$

## 2.5 Gaps

As explained in the sections before, migration is influenced by angular momentum exchange. Furthermore, the outward migration of two planets is possible using the Masset and Snellgrove mechanism. This mechanism relies on the existence of a common gap where the outer planet's ILR and the inner planet's OLR fall, into and hence don't contribute to the net torque. This leads to the following question: Is the gap of one planet deep enough to also eliminate one of the torques which would normally contribute to the net torque (those being the outer planet's OLR and the inner planet's ILR)? For this, an analysis of the gap width and depth has to be made. But first, an explanation on how gaps form is given below.

### 2.5.1 The formation of gaps

A gap is a low density annulus around a planet. For the formation of gaps to occur in a disk, two criteria have to be fulfilled. First the planet's Hill sphere<sup>5</sup> has to satisfy:

$$r_H = r \left( \frac{M_p}{3 M_*} \right)^{1/3} \gtrsim H. \quad (2.45)$$

The second criterion yields:

$$\left( \frac{M_p}{M_*} \right) \gtrsim \left( \frac{c_s}{\Omega(r_p)r_p} \right)^2 \alpha^{1/2}. \quad (2.46)$$

---

<sup>5</sup>which is the sphere around the planet which the planet gravitationally dominates

In consequence, planets which exceed a Saturn mass may open a gap or at least a partial gap, depending on the physical properties of the disk.

The actual gap opening process can be explained as follows. The planet exerts a torque onto the disk in its vicinity, while the disk exerts a torque onto the planet at the LR locations. With growing planet mass, this torque exerted from the planet grows to a point where angular momentum is removed from the gas at the inner vicinity and added to the gas in the outer vicinity. This results in the gas being transported away from the planets vicinity, and a gap has been opened. Opposing to the torque is the turbulent viscosity, which works against sharp radial gradients and fills up the gap. The final gap width and depth is therefore determined by a balance of those opposing forces.

Different models which describe the surface density distribution of a gap have been made and successively improved. One of the most well known is given by [Kanagawa et al. \[2015\]](#) and [Kanagawa et al. \[2017\]](#).

### 2.5.2 Gaprofile of Kanagawa et al 2017

In this section, the information will be taken from [Kanagawa et al. \[2017\]](#) and [Maike Voelkel \[2022\]](#) if not stated otherwise.

[Kanagawa et al. \[2015\]](#) proposed different one-dimensional models of planetary gaps, which are further enhanced by [Kanagawa et al. \[2017\]](#). The model of [Kanagawa et al. \[2017\]](#) adds nonlinear effects and wave propagation, fitting the results of simulations more precisely. Those nonlinear effects are especially important for planets with  $M_p/M_* \gtrsim h(r_p)^3$  and are accounted by introducing a factor  $f_{NL}$ . Normally, it is multiplied with the excitation torque density ([Kanagawa et al. \[2015\]](#) Eq. (17)), but the same effect can also be achieved by multiplying it with parts of the surface density profile. This surface density profile is given by

$$\Sigma(r) = \begin{cases} \Sigma_{min} \cdot f_{NL} & \text{for } |r - r_p| < \Delta r_1 \\ \Sigma_{gap}(r) & \text{for } \Delta r_1 < |r - r_p| < \Delta r_2 \\ \Sigma_0 & \text{for } |r - r_p| > \Delta r_2 \end{cases} \quad (2.47)$$

where the minimal surface density and the gap's surface density are given by:

$$\frac{\Sigma_{min}}{\Sigma_0} = \frac{1}{1 + 0.04K} \quad (2.48)$$

$$\frac{\Sigma_{gap}(r)}{\Sigma_0} = 4 K'^{-1/4} \frac{|r - r_p|}{r_p} - 0.32 \quad (2.49)$$

with

$$K = \left( \frac{M_p}{M_*} \right)^2 \left( \frac{H}{r_p} \right)^{-5} \alpha^{-1} \quad (2.50)$$

$$K' \equiv \left( \frac{M_p}{M_*} \right)^2 \left( \frac{H}{r_p} \right)^{-3} \alpha^{-1} \quad (2.51)$$

and  $f_{NL} = 0.4$ .

Moreover,  $\Delta r_1$  and  $\Delta r_2$  are defined by

$$\Delta r_1 = \left( \frac{\Sigma_{min}}{4\Sigma_0} + 0.08 \right) K'^{1/4} r_p \quad (2.52)$$

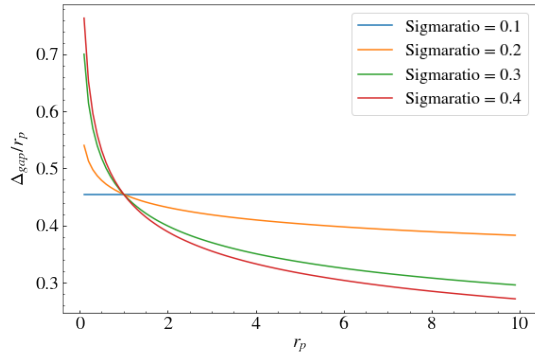
$$\Delta r_2 = 0.33 K'^{1/4} r_p. \quad (2.53)$$

Kanagawa et al. [2017] proposed, that the gap width at a certain ratio of the surface densities  $\frac{\Sigma_{th}}{\Sigma_0}$ , which will now be named Sigmaratio, is given by:

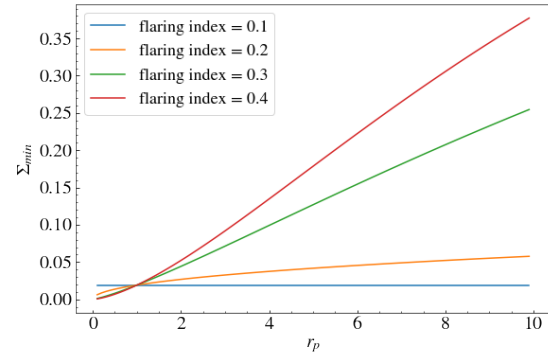
$$\frac{\Delta_{gap}(\Sigma_{th})}{r_p} = \left( 0.5 \frac{\Sigma_{th}}{\Sigma_0} + 0.16 \right) K'^{1/4} \quad (2.54)$$

with the scale height  $H$  and the  $\alpha$  parameter of the alpha viscosity.

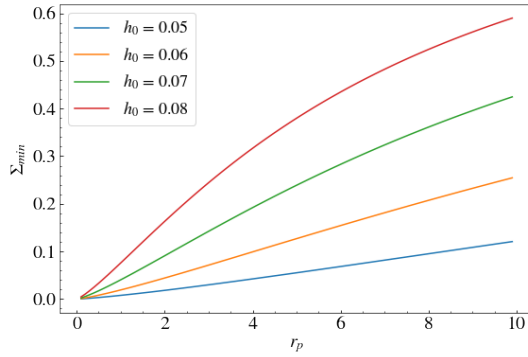
The elimination of the Lindblad torques will happen in very deep gaps. Since there is no precise Sigmaratio given, at which this occurs, a range of Sigmaratios will be tested. The gap width also determines how many locations are eliminated. Both are dependent on the aspect ratio and are changing while the planets migrate outwards. Their evolution during planetary migration are shown in Fig. 2.6a, Fig. 2.6b and Fig. 2.6c.



(a) gap width for different Sigmaratios in dependence of  $r_p$



(b) Kanagawa gap depth for different flaring indexes in dependence of  $r_p$



(c) Kanagawa gap depth for different aspect ratios in dependence of  $r_p$

# Python code of the theoretical approach

This section provides the ideas and steps of the theoretical model derived by the author. The model was implemented in the programming language Python [Van Rossum and Drake, 2009] in form of Jupyter Notebooks [Kluyver et al., 2016] was used. It was accessed via Anaconda [ana, 2020]. The packages NumPy [Harris et al., 2020], Matplotlib [Hunter, 2007] and SciPy [Virtanen et al., 2020] were used for visualisation and calculations. From SciPy `scipy.integrate` and `interp1d` were used. Additionally the code from Maike Voelkel [2022] was used to receive the exact Kanagawa profile.

The assumptions which were presented in Sect. 2.3, are still valid in the following section.

## 3.1 Calculation of the total Torque exerted on the Planets established by the author

The expressions for the LR location and torques in Sect. 2.3.1 and Sect. 2.3.2 are combined to calculate the net torque which is exerted onto the planet. In total sixteen combinations of torque and LR location are presented. All sixteen combinations were implemented in Python script which calculates the net torque and migration rate. The steps taken in the scripts and the main ideas are presented next. In the following chapter the validity of the theoretical approach is tested by comparing the theoretical migration rates to ones from hydrodynamics simulations.

### 3.1.1 Calculation of the Lindblad resonance locations in Python

Not every LR location equation presented in Sect. 2.3.1 has an analytical solution. While assuming a Keplerian disk  $\kappa = \Omega_K$ ,  $D$  can be rewritten

$$r_L = \left(1 + \frac{\varepsilon}{m}\right)^{2/3} r_p \quad (3.1)$$

with  $\varepsilon = 1(-1)$  for the outer(inner) LR. Additionally, Eq. (2.21) also has an analytical solution

$$r_L = \left( \frac{m + \varepsilon}{l} \right)^{2/3} r_p \quad (3.2)$$

for  $l = m, m \pm 1$  while assuming a Keplerian disk.

While  $D_{*,p}$  and  $D_p$  do not assume a Keplerian disk,  $D_K$  does. For those equations, for each  $r_p$  an array with values of the LR locations equations was created for a range of  $0.1 r_0 < r < 20 r_0$  with at least one Million entries. Here  $r_0$  is a characteristic length. With the np.where function, the values of  $r$  were determined, where a sign flip occurred. Between the two  $r$  values, the LR location equation has a root. The two roots of the LR location equation give the outer and inner resonance location. The decision to use np.where rather than solvers for roots, especially those given by SciPy, was made because the solvers need an estimated guess for the locations or a range, in which they occur. This often led to them not finding solutions at all or their solutions deviate significantly from the ones np.where would find.

The planets in this work are massive enough to open at least a partial gap. When they are in MMR and migrate together, the two gaps fuse into a common gap in between the planets. Besides extinguishing the inner planets OLR and the outer planets ILR, this common gap may weaken or even extinguish some outer planets OLR and some inner planets ILR, depending on its depth. The applied gap profile follows Eq. (2.54), giving the possibility to calculate the gap's size at a given depth. The depths for which the torques would be eliminated were chosen between  $0.1 \leq \text{Sigmaratio} \leq 0.3$ . The resonances which fulfil

$$r_L > r_p + \frac{\Delta_{gap}(\Sigma_{th})}{2} \quad \text{outer Resonances} \quad (3.3)$$

$$r_L < r_p - \frac{\Delta_{gap}(\Sigma_{th})}{2} \quad \text{inner Resonances} \quad (3.4)$$

are exerting a torque onto the planet. Consequently all resonance locations given by the five resonance locations equations, which are eliminated by the gap, do not contribute to the net torque. In Python this was achieved by setting the value of the resonance location to np.none.

Additionally, the torque cutoff from Goldreich and Tremaine [1980] has to be considered. Without the cutoff radius some locations may get arbitrarily close to the planet. With it, they accumulate at the cutoff radius for  $m \gg 1$ . Thus for radii closer to the planet than

this accumulation location:

$$r_L < r_{\text{cutoff}} \quad \text{outer Resonances} \quad (3.5)$$

$$r_L > r_{\text{cutoff}} \quad \text{inner Resonances} \quad (3.6)$$

$r_L$  is set to  $r_{\text{cutoff}}$ .

The combination of the described steps results in a 2D-array of LR locations for each planet location. The effects of different Sigmaratio are discussed in [chapter 4](#).

### 3.1.2 Calculations of the net torques in Python

The different Lindblad torque expressions GT79, Ward3 and Ward8 were implemented in Python. For this, a lookup table for the Laplace coefficients  $b_{1/2}^m(\alpha_r)$  and their first two derivatives  $db_{1/2}^m(\alpha_r)/d\alpha_r$  and  $d^2 b_{1/2}^m(\alpha_r)/d\alpha_r^2$  was created by Thomas Rometsch.

The torques could then be retrieved by evaluating them at the locations given by Sect. 3.1.1. Some locations still fall into the planetary gap but not in the region, where they would be eliminated. Nevertheless, this weakens the torques of those locations. For this reason, the torques are weighted with the dimensionless surface density profile presented in Eq. (2.47). In the scripts, this profile is defined section-wise and is therefore not smooth. A smooth version is provided by the code of [Maike Voelkel \[2022\]](#), but the code does not always find a solution for the surface density profile for certain disk configurations. For the configurations used in [chapter 4](#), the code almost never found a solution and consequently the section wise definition will be applied. A comparison between the exact profile and the section-wise definition is shown in Fig. 3.1

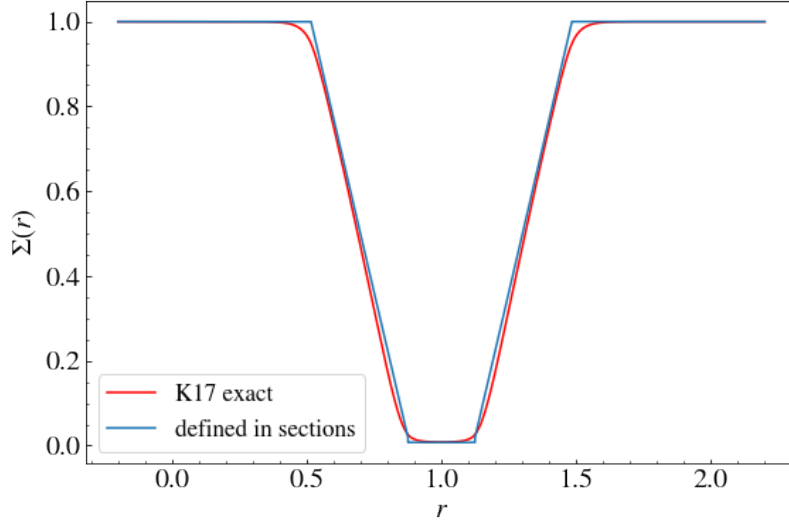


Figure 3.1: Comparison of the exact and section-wise defined surface density profile by Kanagawa et al. [2017]

This shows that the difference between the profiles is small enough to justify the usage of the section-wise definition.

By summing up all contributions for different  $m$ , the inner and outer torque can be determined. While migrating, the planets are locked in an MMR, which allows the calculation of one planet's location when given the other, using

$$\left( \frac{r_{p,\text{inner}}}{r_{p,\text{outer}}} \right)^{-3/2} = \text{MMR} . \quad (3.7)$$

Hence

$$\Gamma_{\text{ILR}}(r_{p,\text{inner}}) + \Gamma_{\text{OLR}}(r_{p,\text{inner}} \text{ MMR}^{2/3}) = \Gamma_{\text{LR}} \quad (3.8)$$

provides the correct net torque.

### 3.1.3 Migration rate calculation in Python

The calculation's validation is checked by comparing the Python script results to the simulations. The migration rate has to be used for comparison, since the net torque on the system cannot be retrieved easily from the simulations. By assuming a negligible

eccentricity, the migration rate can be approximated to:

$$\dot{a}_p = \frac{2 \Gamma_{\text{LR, all}}}{\Omega_p a_p (M_{p,\text{inner}} + M_{p,\text{outer}})}. \quad (3.9)$$

The steps for this approximation are listed in Appendix A. It is also the general migration rate which occurs, when torques are exerted when neglecting the eccentricity. The calculation for this is shown in Appendix B. With this, the rate for different  $r_p$  can be given or the general evolution of the migration can be evaluated.

# FARGO3D code and setups

The simulations presented in this thesis were performed with FARGO3D [Benítez-Llambay and Masset, 2016], the successor of FARGO [Masset, 2000]. It is a parallel hydrodynamics and magnetohydrodynamics code, which allows simulations of protoplanetary disks in several dimensions (1D, 2D and 3D), as well as the usage of different geometries (like cylindrical, spherical or Cartesian) and inertial frames. The planets are handled by a fifth order Runge-Kutta integrator. The capability to be run on a graphics processing unit (GPU), which additionally can run in parallel mode, greatly decreases the time needed to complete simulations. Therefore simulations with large disk and/or high resolution can be performed in at a reasonable time. The simulations were run on the bwForCluster BinAC.

In this thesis, 2D simulations of gaseous disks were run. In the following section the basic structure of the FARGO3D code will be explained, especially how the physics presented in Sect. 2.1 are actualised. Afterwards, the specific setups of the method to calculate the migration's stopping radius will be listed.

## 4.1 The FARGO3D code

In this thesis, the disk is assumed to be locally isothermal, but it is also possible to choose an adiabatic equation of state. The code offers to run the simulations using dimensionless units, the CGS or the MKS unit systems. The dimensionless option was used, which is specified when explaining the specific setups. A cylindrical, 2-dimensional frame with its center fixed to the star was chosen. It co-rotates with the system with a constant angular velocity set by  $\text{OmegaFrame}$  defined at  $r_0$ . The value  $\text{OmegaFrame} = 1.0003$  has been used. With  $\text{OmegaFrame} = 1$  the frame would rotate with the Keplerian velocity at  $r_0$ . In the code, the azimuthal velocity of the gas at  $r_0$  is then close to zero. The frame has an outer and inner radius, given by  $r_{out}$  and  $r_{in}$  respectively, while the mesh covers a full circle in azimuth direction. Hence, the disk has the shape of a circle with a hole in the middle. The mesh is divided into cells with logarithmic spacing. A constant spacing would oversample the outer and undersample the inner disk. To have cells with a quadratic shape,

the number of cells are chosen for given  $r_{out}$ ,  $r_{in}$  and  $h_0$  accordingly.

The disk's physical properties are implemented as follows: The equation of state, which the disk follows, is isothermal and given in Eq. (2.6). The surface density of the gas follows

$$\Sigma(r) = \Sigma_0 \times \left( \frac{r}{r_0} \right)^{-p}. \quad (4.1)$$

Here,  $\Sigma_0$  defines the surface density at  $r_0$  and  $p$  a dimensionless parameter defining the density slope.

The scale-height is given by:

$$H = \frac{c_s}{\Omega} \quad (4.2)$$

while satisfying  $H \ll r$ . The disks temperature profile follows:

$$T(r) = T_0 \left( \frac{r}{r_0} \right)^q. \quad (4.3)$$

With this, the aspect ratio can be expressed as:

$$h = \frac{H}{r} = h_0 \left( \frac{r}{r_0} \right)^\beta \quad (4.4)$$

with the flaring index  $\beta = (q + 1)/2$ .

The gas is initialised on Keplerian orbits with the Keplerian velocity defined by:

$$v_K = \Omega_K \cdot r; \quad \Omega_K = \sqrt{\frac{GM_*}{r^3}} \quad (4.5)$$

using the Keplerian frequency  $\Omega_K$ . Furthermore, the viscosity is prescribed, using the  $\alpha$  viscosity model from [Shakura and Sunyaev \[1973\]](#) given in Eq. (2.3).

#### 4.1.1 Smoothing of the planet potential

The potential is calculated at the cell's centre

$$\Phi = -\frac{GM_*}{r} - \frac{GM_p}{\tilde{r}} \quad \tilde{r} = \sqrt{(x_{\text{cell center}} - x_p)^2 + (y_{\text{cell center}} - y_p)^2} \quad (4.6)$$

where  $r$  is the distance from the planet to the star. This diverges for planets located at or very close to the cell centre. Consequently a smoothing length is added to Eq. (4.6), which is called *smoothing*. Two smoothing methods are provided: the RocheSmoothing (or HillSmoothing) and the ThicknessSmoothing. In either case the second part of the planet's potential is modified

$$\Phi = -\frac{GM_p}{r} \longrightarrow \Phi_S = -\frac{GM_p}{\sqrt{r^2 + s^2}} \quad (4.7)$$

with the potential smoothing length  $s$ . This smoothing length is defined differently by the smoothing methods.

### RocheSmoothing

Using RocheSmoothing,  $s$  is defined by:

$$s = \text{RocheSmoothing factor} \cdot r_H \quad (4.8)$$

with the Hill radius defined in Eq. (2.45). The RocheSmoothing factor not used in this thesis. According to Müller et al. [2012] Roche-smoothing estimates a value for the gravitation, which is too high. They established that the smoothing length should be proportional to  $H$ . This is given by the ThicknessSmoothing.

### ThicknessSmoothing

Here,  $s$  is defined by:

$$s = \text{ThicknessSmoothing factor} \cdot H \quad (4.9)$$

with  $H$  defined by Eq. (4.4). The ThicknessSmoothing factor is also chosen to be 0.6.

Moreover, when a planet is placed into the disk it will create density waves. They could distort the results, if those waves interact with the boundaries. Therefore, a damping zone is incorporated. This damping zone uses the so-called Stockholm damping [Val-Borro et al., 2006] which exponentially damps the waves and has a smooth transition into the disk. The orbital frequency ratio of the damping zones inner radius and the mesh's outer boundary is 1.5.

Furthermore, another correction of the potential has to be made. The star gets accelerated by the planet, which leads to a non-inertial frame. The IndirectTerm corrects this acceleration and consequently has to be turned on during the whole simulation. Additionally

to the IndirectTerm, a GasIndirectTerm exists. It considers the force of the disk onto the planet and thus needs to be turned on, too, whenever the planets interact with the disk, which is when migration starts

Lastly, the module BM08 [Baruteau and Masset, 2008] corrects a discrepancy between acting forces. While the gas only feels the star's potential, the planet feels the star's and gas potential. This leads to an LR location shift and can be corrected using BM08. The correction is achieved by removing the azimuth averaged density prior to the force calculation. Since the torque is dependent on the used surface density, the module also changes their values. The effect of the shift and the change of torque will be examined in chapter 4 by comparing the simulations results with and without the module to the theoretical model.

### 4.1.2 Boundary conditions

Since it is not possible to implement an infinitely large disk, boundary conditions need to be introduced. The main types of boundary conditions in FARGO3D are anti-symmetrical, symmetrical and Keplerian. In addition to those, outflow and viscous boundaries were defined for the setups in this thesis. Every used boundary conditions will be shortly discussed and the code for them will be provided in a GitHub repository (LINK!).

Cells outside the mesh are ghost cells, with which the boundary conditions are implemented. They are not part of the active mesh. Here the zone outside the active mesh, which is called the buffer zone, is 3 ghost cells wide in radial direction. The mesh is periodic in  $\phi$  direction, therefore no ghost cells are needed there.

#### Boundary conditions for $v_r$

In the disk, gas with a negative radial velocity moves towards the star, and away from the star with a positive radial velocity. This allows the creation of custom boundary conditions.

#### Outflow on the inside

The values of the active mesh cells bordering the boundary are also mapped to the ghost cells, if the velocity of the mesh cells below is zero. Otherwise the ghost cell value is zero. This allows outflow at the inner boundary.

#### Outflow on the outside

The values of the active mesh cells bordering the boundary are also mapped to the ghost

cells, if the velocity of the mesh cells above is zero. Otherwise the ghost cell value is zero. This allows outflow at the outer boundary.

### Boundary conditions for $v_\phi$

#### Keplerian

These boundary conditions are used in radial direction for the azimuthal velocity and assigned the Keplerian velocity at the radius of the ghost cells.

## 4.2 Setup (*BM08*)theory

Before discussing the simulations ran for the theoretical approach in detail, the parameters which apply for all of them are presented. For the simulations, a scale free system is used, which can later be re-scaled. Table. 4.1 shows the fixed parameters.

Table 4.1: fixed parameters for the (*BM08*)theory setup

Dimensions	$r_0$	$a_1$	$a_2$	$M_*$	$p$
dimensionless	1	1	2	1	1.5

The disk extents from  $0.4 r_0$  to  $59 r_0$  with cells that scale logarithmically with the radius. The resolution was chosen to be 10 cells per scale height, meaning each cell has an extend of one tenth of the local scale height. For the different scale heights, the number of cells are listed in Table 4.2.

Table 4.2: cells needed in each spatial dimension for a resolution of 10 cells per scale height, with squared cells [Rometsch]

$n_r$	$n_\theta$	$h_0$
1001	1257	0.05
835	1047	0.06
716	898	0.07
627	785	0.08
557	698	0.09

Additionally the cells are squared. Simulations with and without the BM08 modules were stared. All of them were evolved for 1000 orbits during which the gravitational interaction

between the planets and the disk is not enabled. After that, the systems were evolved for 18.000 additional orbits during which the interaction was enabled. The distinction of those two phases is needed to prevent an non-physically migration of Type I, which could occur for large planets in the simulations. The gap of both planets needs enough time to develop, hence the 1000 orbits were chosen. Since the outcome of the theoretical approach assumes a fully stationary gap, this step is crucial. All setups have outflow inner and outer boundary conditions, and ThicknessSmoothing was used.

The setups created to test the validity always differ from each other in only one aspect are listed in Table 4.3

Table 4.3: Simulation names and parameters for the rough testing of the torque calculations

name	$M_{p,\text{inner}} [M_*]$	$M_{p,\text{outer}} [M_*]$	$\alpha$	$\Sigma_0$	$h_0$	$\beta$	BM08
(BM08) <i>theory_1</i>	$3 \cdot 10^{-3}$	$1 \cdot 10^{-3}$	$10^{-3}$	$10^{-3}$	0.06	1/3	(Yes) No
(BM08) <i>theory_2</i>	$3 \cdot 10^{-3}$	$1 \cdot 10^{-3}$	$10^{-3}$	$10^{-3}$	0.06	0.2	(Yes) No
(BM08) <i>theory_3</i>	$3 \cdot 10^{-3}$	$1 \cdot 10^{-3}$	$10^{-3}$	$10^{-3}$	0.06	0.25	(Yes) No
(BM08) <i>theory_4</i>	$3 \cdot 10^{-3}$	$1 \cdot 10^{-3}$	$10^{-3}$	$10^{-3}$	0.07	0.25	(Yes) No
(BM08) <i>theory_5</i>	$3 \cdot 10^{-3}$	$1 \cdot 10^{-3}$	$10^{-3}$	$10^{-4}$	0.06	0.25	(Yes) No
(BM08) <i>theory_6</i>	$2 \cdot 10^{-3}$	$1 \cdot 10^{-3}$	$10^{-3}$	$10^{-3}$	0.06	0.25	(Yes) No
(BM08) <i>theory_7</i>	$4 \cdot 10^{-3}$	$1 \cdot 10^{-3}$	$10^{-3}$	$10^{-3}$	0.06	0.25	(Yes) No
(BM08) <i>theory_8</i>	$5 \cdot 10^{-3}$	$1 \cdot 10^{-3}$	$10^{-3}$	$10^{-3}$	0.06	0.25	(Yes) No
(BM08) <i>theory_9</i>	$3 \cdot 10^{-3}$	$1 \cdot 10^{-3}$	$10^{-4}$	$10^{-3}$	0.06	0.25	(Yes) No
(BM08) <i>theory_10</i>	$3 \cdot 10^{-3}$	$1 \cdot 10^{-3}$	$10^{-5}$	$10^{-3}$	0.06	0.25	(Yes) No

The term  $M_{p,1}$  gives the inner planet's mass while  $M_{p,2}$  gives the outer planet's mass. The flaring index is denoted by  $\beta$ . Each simulation was also processed with the BM08 module, which is indicated by the BM08 in apprentices. The usage of the model is the only difference between these two sets.

If the disk is too heavy, e.g due to a large  $\Sigma_0$ , it may be possible that the planets migrate with migration Type III [Masset and Papaloizou, 2003]. To avoid this,  $\Sigma_0 \leq 10^{-3}$ .

# Results

After running the simulations presented in Sect. 4.3, they were evaluated. For each of them, the semi-major axis, eccentricity and the ratio of the orbital frequencies were plotted and examined. The comparison of the simulations to the theoretical calculations presented in Sect. 3.1 covers two aspects: evaluating the overall migration behaviour as well as comparing the migration rate at one  $r_p$ . The behaviour includes the direction of the migration, and whether they stopped migrating completely. The theoretical approach is not capable of predicting behaviour whenever the planets are not locked in MMR resonance, which includes migration jumps and close encounters. Moreover, vortexes outside the gap may form and further influence the migration are not included in the theory.

The setups presented in Sect. 4.2 are further divided into 2 sets: one set with the BM08 module and one without.

## 5.1 Setups *theory*

### 5.1.1 Comparison of the general outcome of migration

First, the general migration behaviour of the simulations and the theoretical approach are evaluated. In order to keep a better overview, the evaluation is divided: the setups compared have used the same LR location equation and differ in the torque equation used. When using Eq. (2.21) for higher orders of  $l$ , the torque equation does not change, since GT79 is always used, but the eccentricity is a variable parameter. The average eccentricity for each simulation was determined during the time the planets were in MMR. Then the simulations were compared to the one of the 4 available options,  $e = 0.025, 0.05, 0.075$  or  $e = 0.1$ , for which the simulations mean eccentricity was closest to.

The comparisons are written down into tables, which can be found in Appendix C.

## Evaluation of the Simulations

Most simulations ended with a close encounter after experiencing one or more migration jumps. The simulations in this thesis have shown, that in case of a smaller jump the inner planet maintains its migration behaviour, but for larger jumps, where the outer planet covers a large distance, the inner planet is pushed inwards when the outer planets catches up with it. Furthermore, they are mostly locked in 2:1 MMR, which indicates that the planets do not migrate very rapidly. As an example of this migration evolution, the semi-major axis, eccentricity as well as the logarithmic surface density from *theory\_2* are shown in Fig. 5.1 to Fig. 5.3.

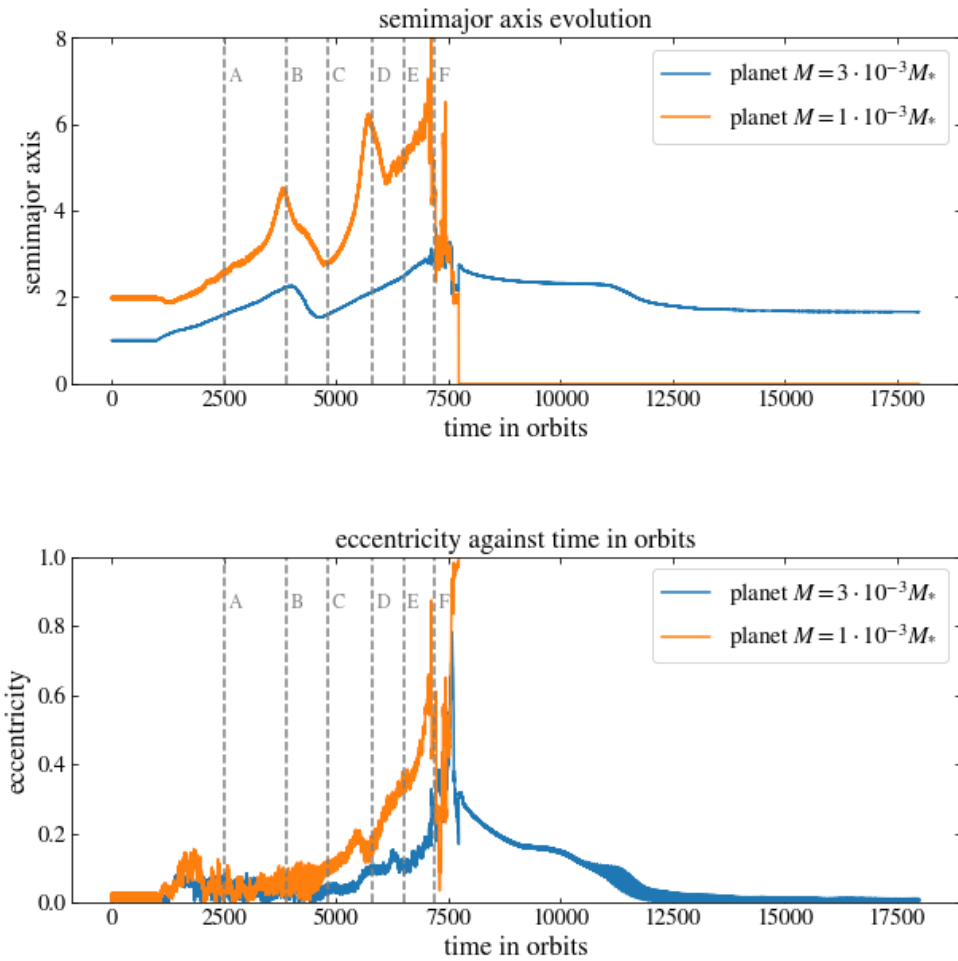


Figure 5.1: Semi-major axis and eccentricity evolution over 18.000 orbits. The dashed lines mark the number of orbits, where the surface density is plotted.

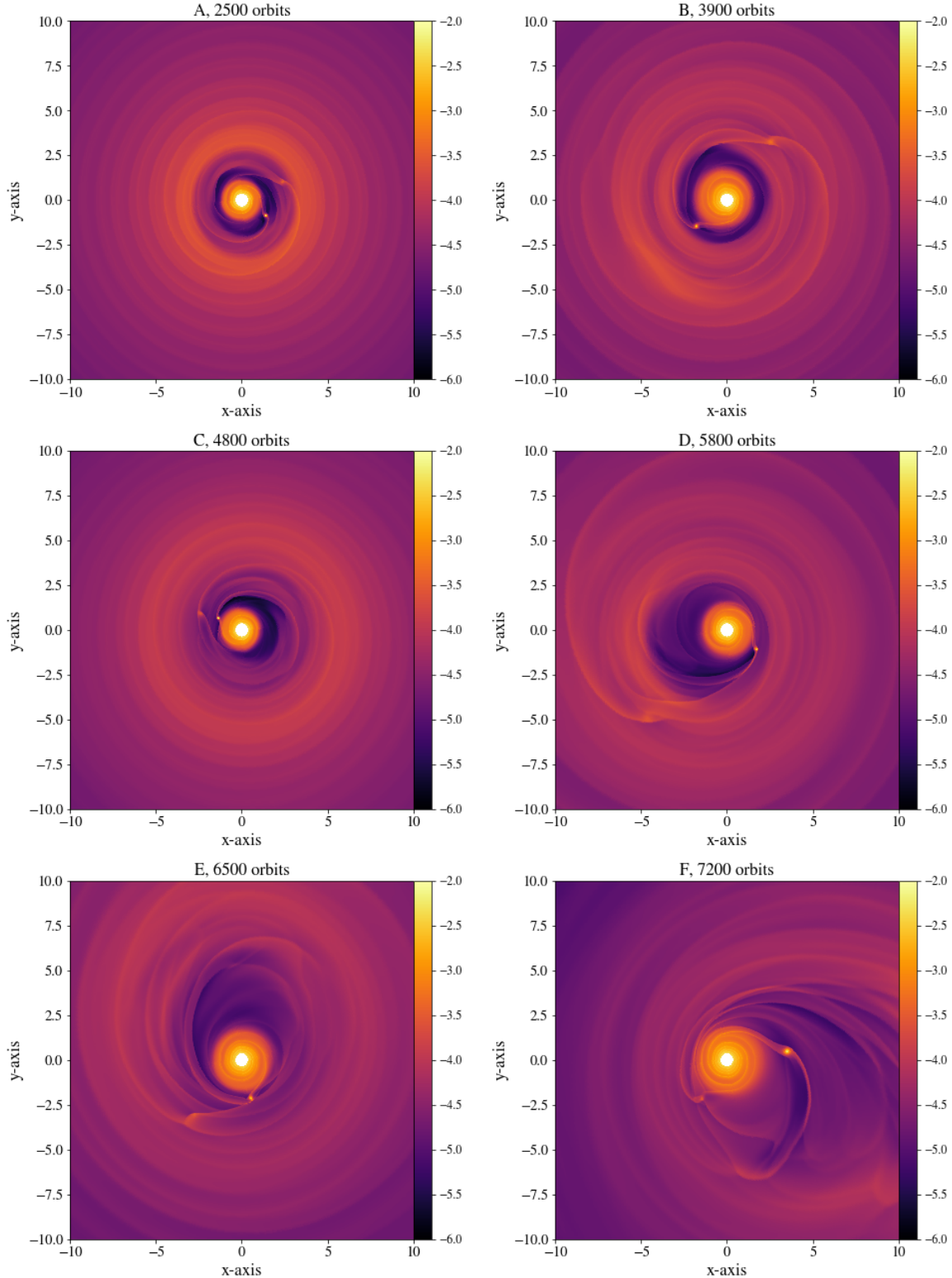


Figure 5.2: Disk surface density in a region from  $[-10,10]$  in x and y direction after different orbits. The surface densities value is indicated by the color range, whose values are the exponents for a logscale with the base 10. After 4800 orbits, it is first notable that the gap is very asymmetric. The close encounter happened around 7200 orbits, which is shown in plot F.

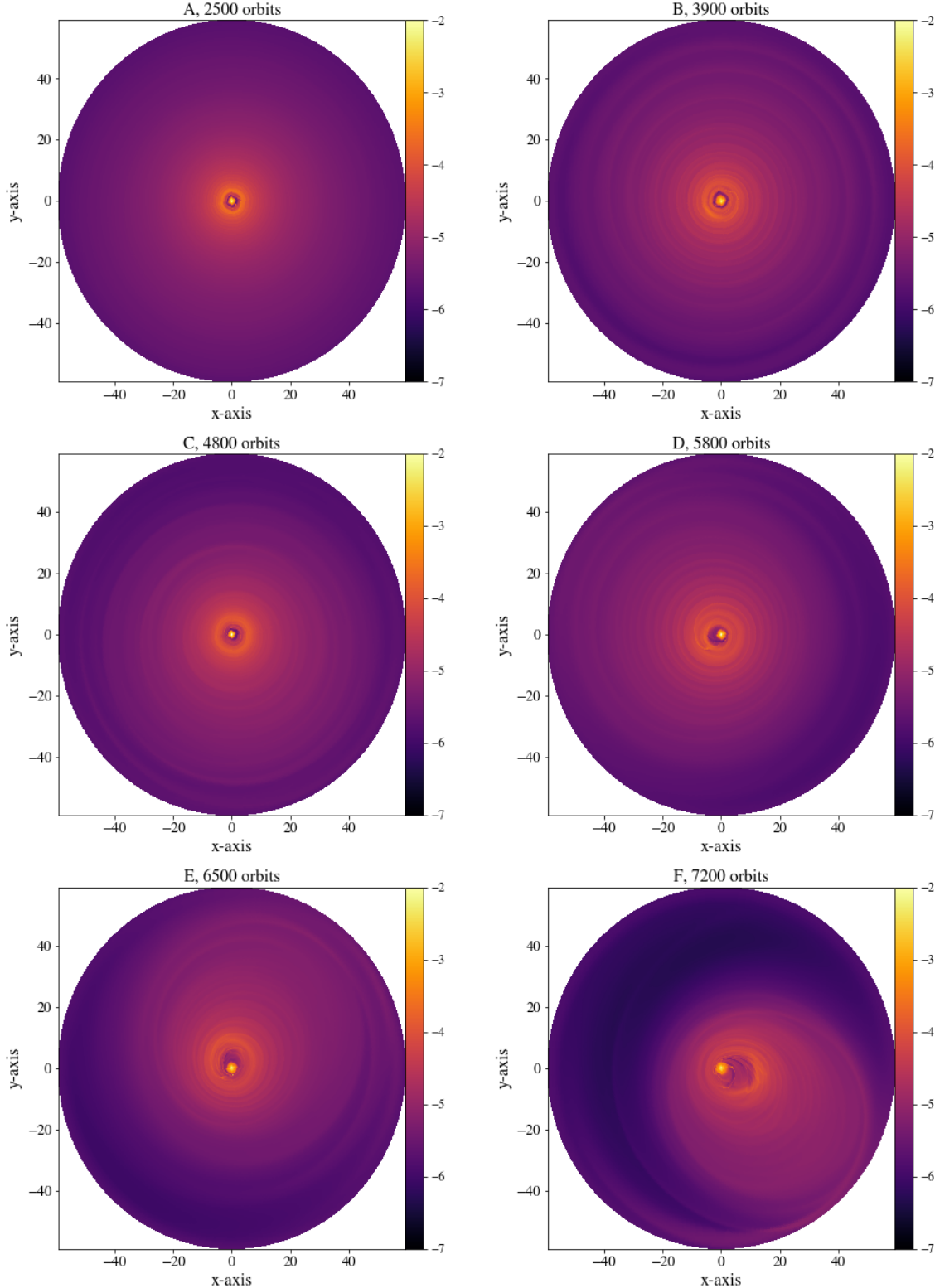


Figure 5.3: Disk surface density after different orbits. The surface densities are indicated by the color range, whose values are the exponents for a logscale with the base 10. After 4800 orbits, it is first notable that the gap is very asymmetric. The close encounter happened around 7200 orbits, which is shown in plot F.

After both planets evolved their gap for 1000 orbits, they start to interact with each other and with the disk. In this setup, the outer planet migrated inward, most likely with Type I migration, while the inner planet migrated outward with Type 2 migration. Due to the common gap, the outer planet is pushed outwards while the inner planet is pushed inwards. They catch up in 2:1 MMR after 1200 orbits, which they maintain until 2000 orbits. During this time they get more eccentric. The eccentricity of both planets moves very rapidly between two values, which results in the planets being in and out of MMR from 2000 to 3500 orbits. The eccentricity is most probably influenced by the disk, because also the gap gets asymmetric during this period as well. They experience their first migration jump around 3500 orbits. During this jump, they are not in a MMR resonance. As the outer planet comes back from the jump, they do not immediately catch up in an MMR again, which results in them both migrating inwards. They catch up again around 5000 orbits and migrate outwards again. During this time, a second migration jump happens while the disk is unstable, leading to a growing eccentricity of both planets. Even though their eccentricity is very high, the eccentricity does not move between two values but stays relatively constant. This allows the planets to catch up in a 2:1 MMR again over the period from 6300 to 7000 orbits. Then, as a consequence of their very eccentric orbits, they experience a close encounter.

The migration stops in simulation *theory\_8* without a migration jump, while *theory\_10* experiences a very small and short jump. As an example for a stalling migration, the eccentricity, semi-major axis and surface density of *theory\_8* is shown in Fig. 5.4 to Fig. 5.6.

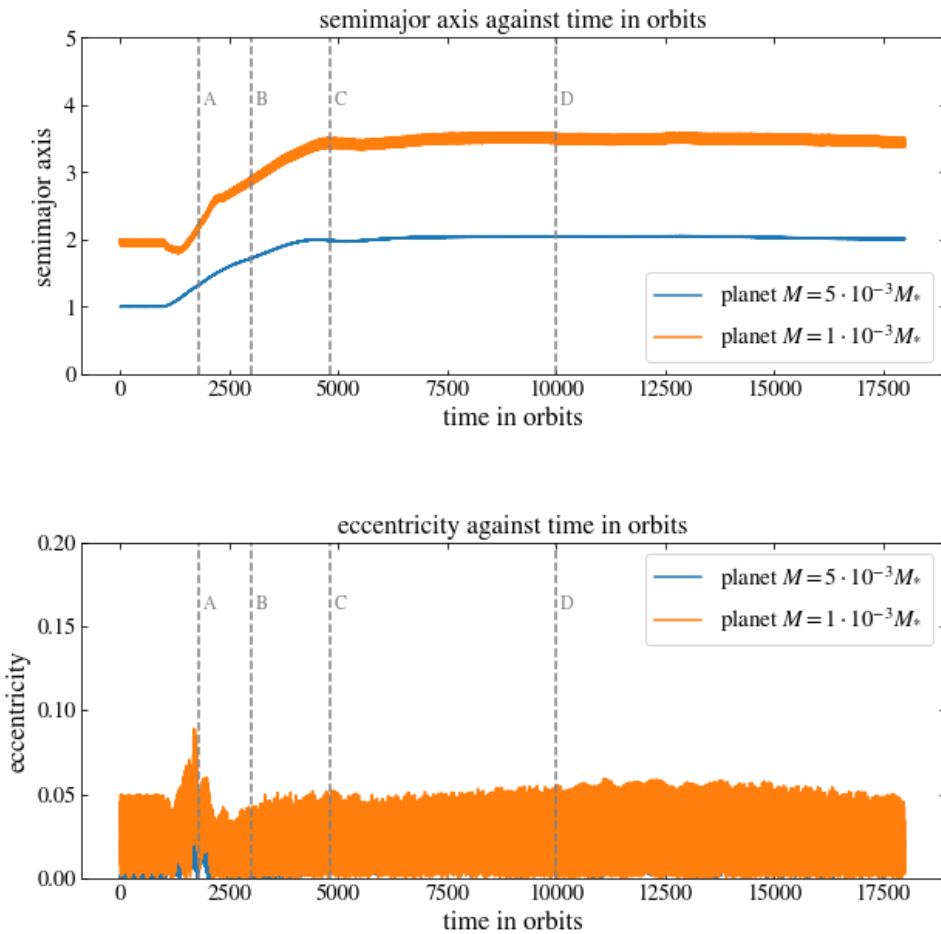


Figure 5.4: Semi-major axis and eccentricity evolution over 18,000 orbits. The dashed lines mark the number of orbits, where the surface density is plotted.

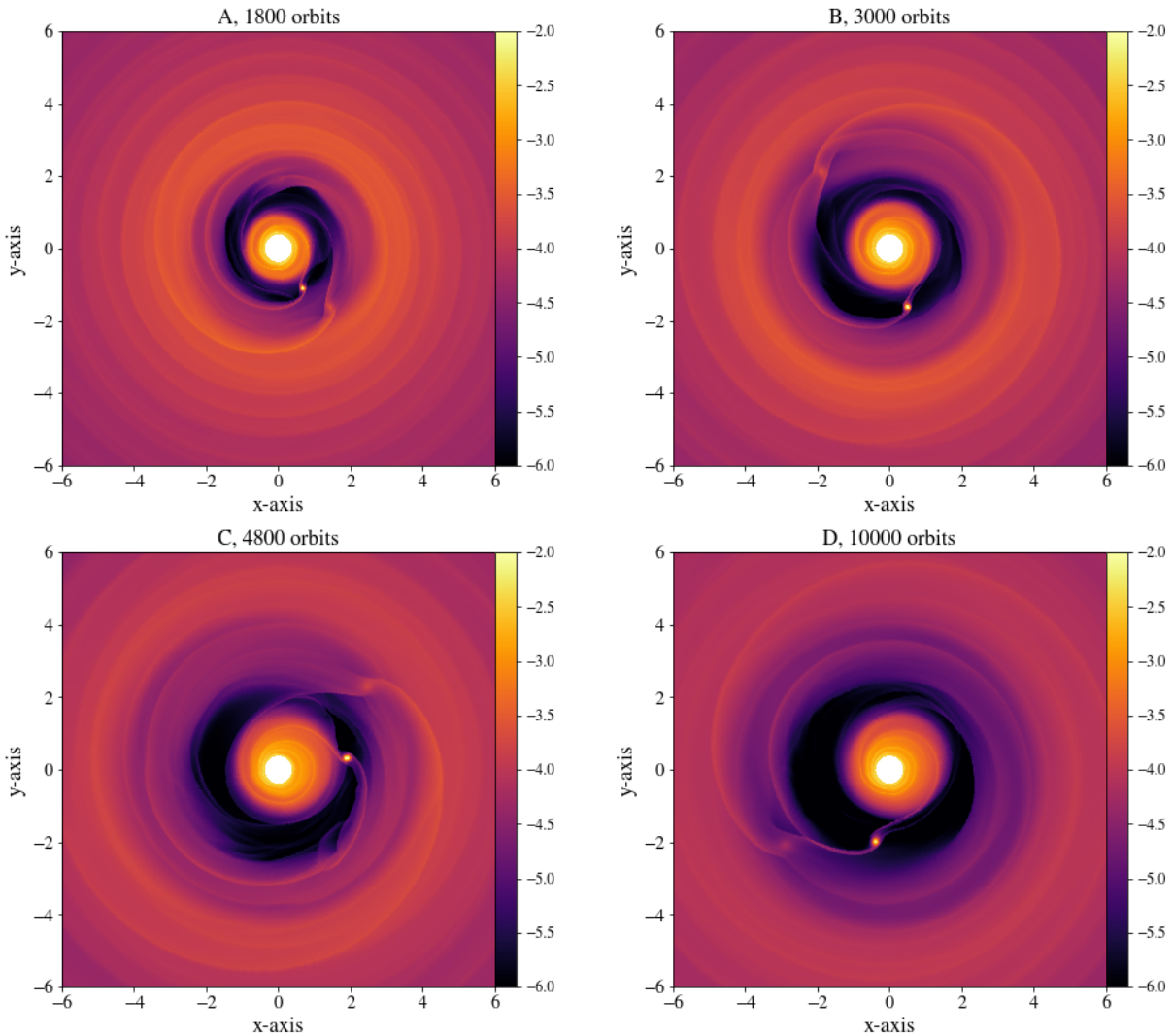


Figure 5.5: Disk surface density in a region from  $[-6,6]$  in x and y direction after different orbits. The surface densities are indicated by the color range, whose values are the exponents for a logscale with the base 10.

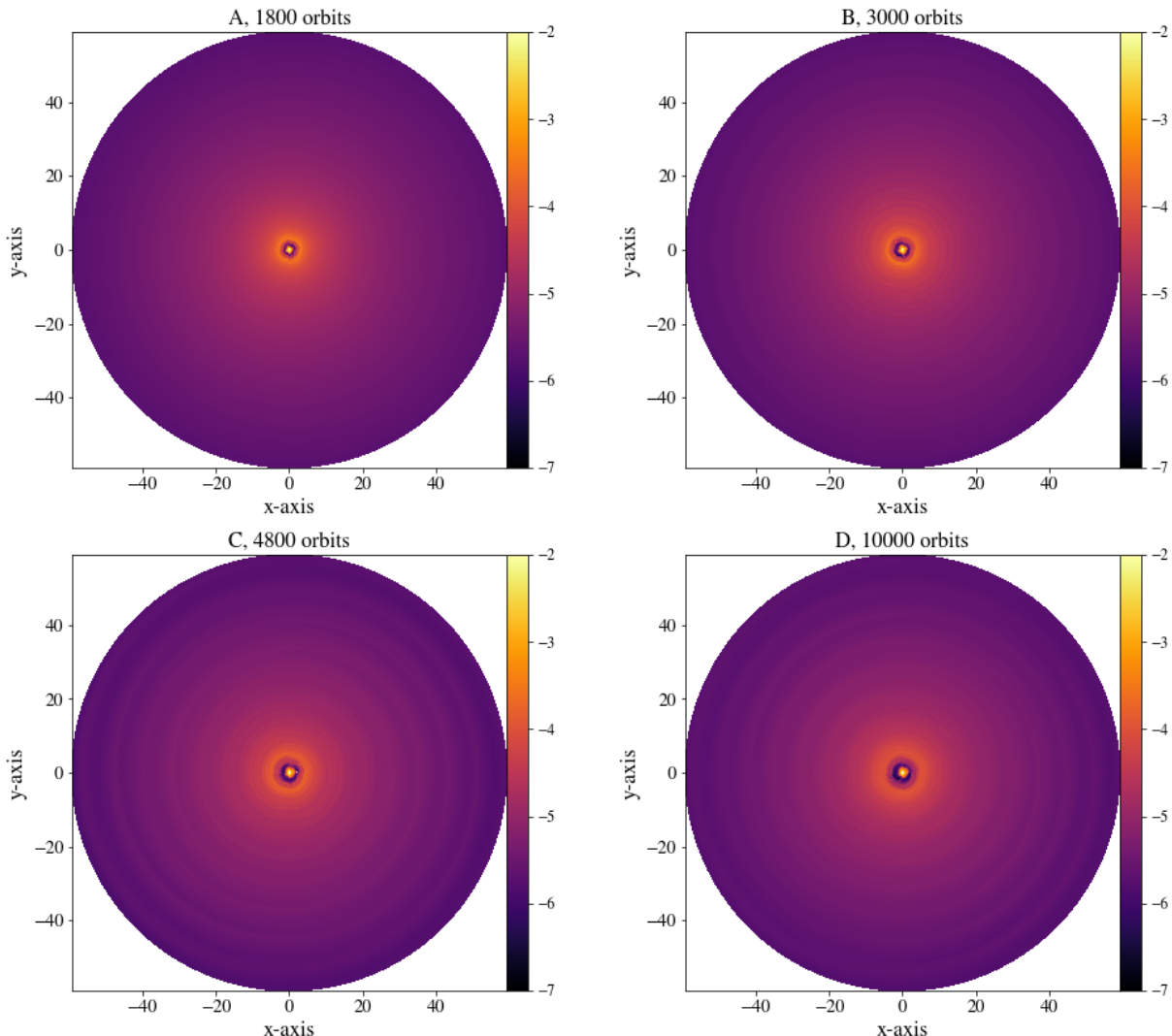


Figure 5.6: Disk surface density after different orbits. The surface densities are indicated by the color range, whose values are the exponents for a logscale with the base 10.

As seen in the evaluation of *theory\_2*, the inner planet migrates outwards while the outer planet migrates inwards as soon as they interact with each other and the disk. They catch up in 2:1 MMR and maintain it from 1400 to 1700 orbits. During this time, the planet's eccentricity grows and librates very rapidly, bringing the planets out of MMR. While the eccentricity very rapidly changes, no MMR can be detected while they migrate outwards. They stop their migration around 5000 orbits, but are not in an MMR during this. During the migration, the disk does not get elliptic and the density spirals exerted at the LR location are visible, as they travel through the disk.

Lastly, *theory\_5* migrates very slowly, but does not experience a migration jump. in Fig. 5.7 to Fig. 5.9 show the semi-major axis, eccentricity and disk surface density.

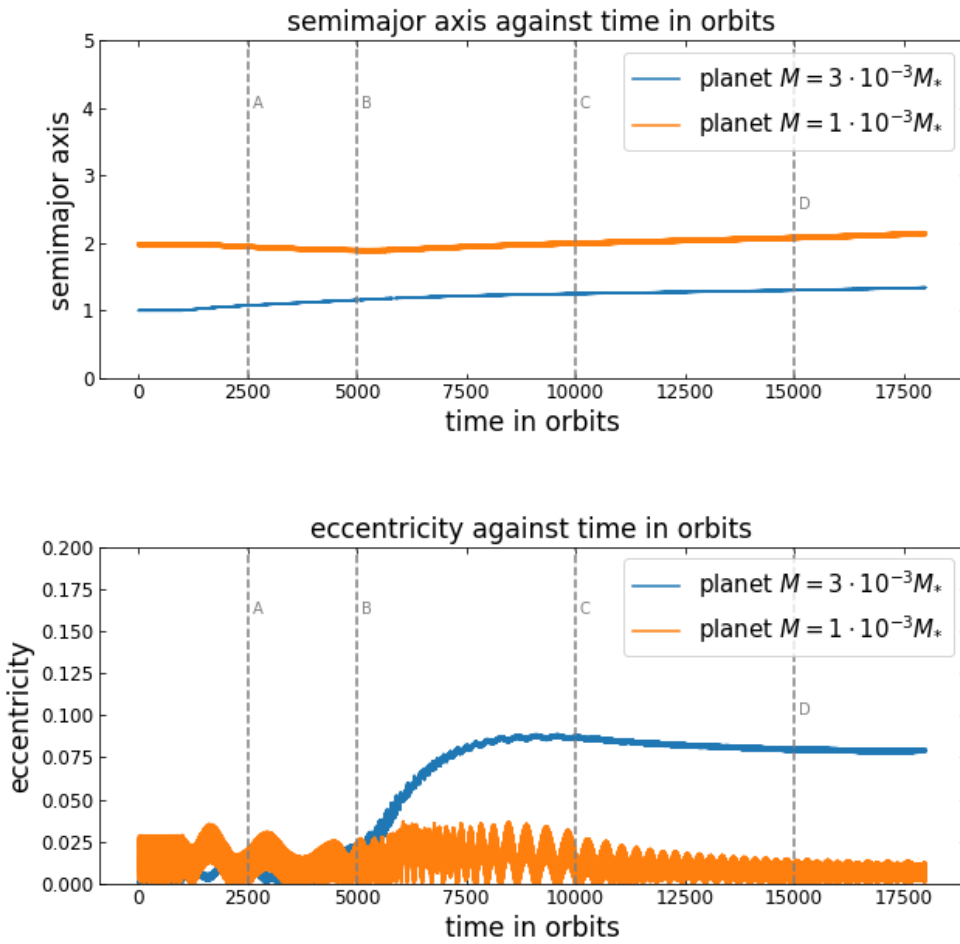


Figure 5.7: Semi-major axis and eccentricity evolution over 18.000 orbits. The dashed lines mark the number of orbits, where the surface density is plotted.

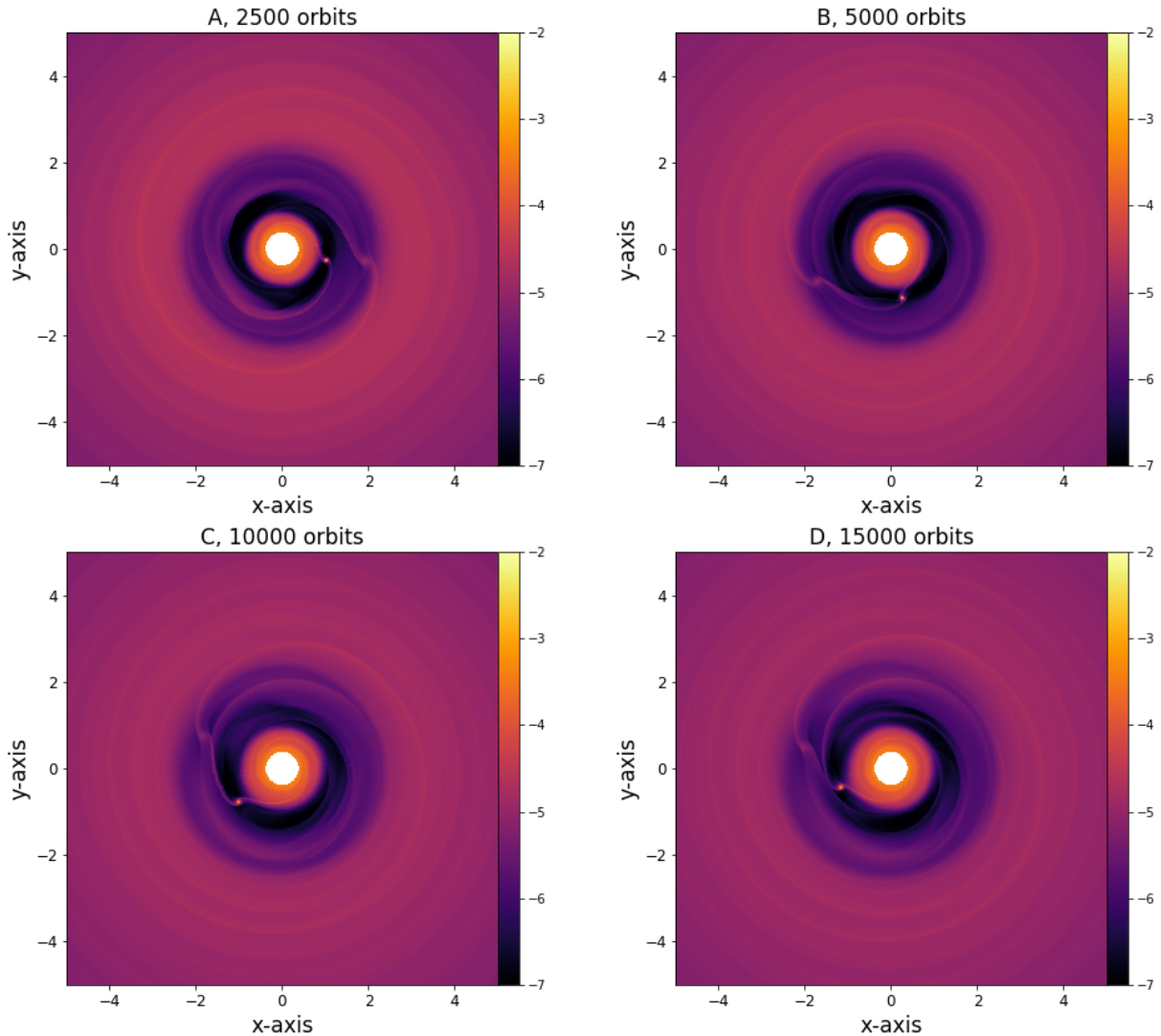


Figure 5.8: Disk surface density in a region from  $[-6,6]$  in x and y direction after different orbits. The surface densities are indicated by the color range, whose values are the exponents for a logscale with the base 10.

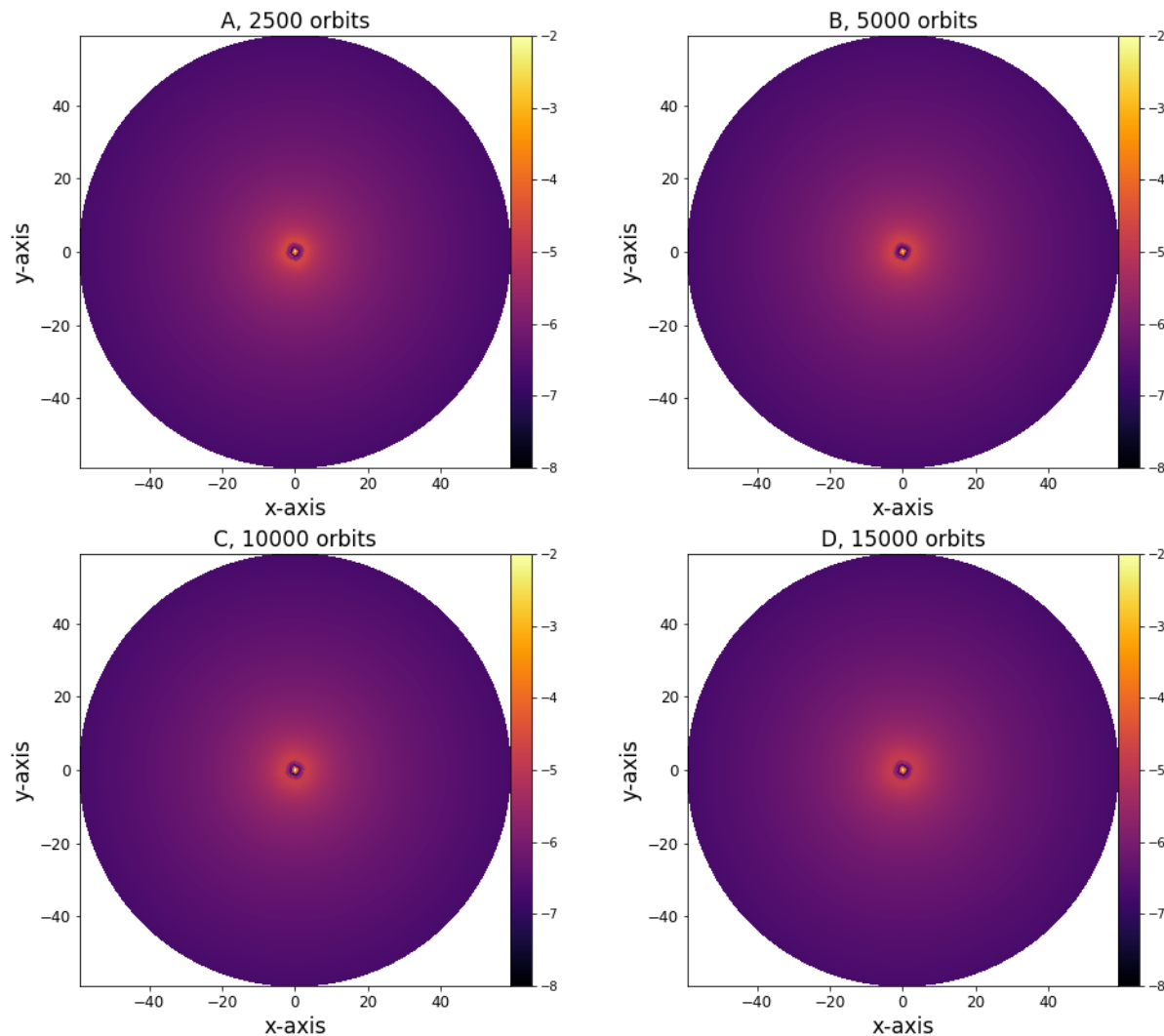


Figure 5.9: Disk surface density after different orbits. The surface densities are indicated by the color range, whose values are the exponents for a logscale with the base 10.

The eccentricity of this system does not change very rapidly, but the inner planet has a constant eccentricity of 0.1 after 5000 orbits. Additionally, they are in a very stable 2:1 resonance since 5000 orbits. The surface density is also not disturbed and the whole system remains very calm.

This analysis shows that higher eccentricities are not the cause of the MMR disturbance, but the rapid eccentricity changes are. The increasingly elliptic disk may be the reason for this. This phenomenon is probably related to the GasIndirectTerm which is activated while the planets migrate. If it is active, the disk also exerts a force onto the star, which leads to a change in the disk's velocity. This could be a self-enhancing effect, leading to an elliptic disk. Still, the GasIndirectTerm can't be left out because the coordinate system would then not be an inertial system anymore. All simulations in this set which ended up in a close encounter, had this encounter during a migration jump. Additionally it was tested if a vortex formed outside the gap before a migration jump. For this, the vortensity of the disk was plotted, defined by:

$$\frac{\omega}{\rho} = \frac{\nabla \times \vec{v}}{\rho} \quad (5.1)$$

[Armitage, 2009], the vorticity<sup>1</sup>  $\omega$  divided by the surface density  $\rho$ . It can be concluded that not for every migration jump a vortex was visible, especially when they had a two migration jumps shortly after each other.

### Comparison of the migration behaviour

Starting the comparison with the LR locations given by  $D$ , their migration behavior did not match the simulations in a single case for the torques given by Ward3 and GT79, because both always predicted an inward migration. The combination of  $D$  and Ward8 matched for  $h_0 = 0.07$  (setup *theory\_4*) and some setups with  $\text{Sigmaratio} = 0.1$ . It also forecasts a stopping of the migration in two instances, which could not be seen in the simulations. In general, the combination of  $D$  and the torques seems to give a poor estimate of the migration's behaviour. Since  $D$  is the LR location equation, which does not consider the disk pressure, it is not surprising that it does not result in good estimates for simulations which contain pressure.

The insertion of  $D_p$  into the different torques never leads to a matching behaviour, because inwards migration is always predicted, whereas the simulation results always show outward

---

<sup>1</sup>describes the tendency of the gas to rotate

migration.

When inserting  $D_K$  into Ward3 leads to an overall matching migration behaviour, especially for  $\text{Sigmaratio} = 0.1$  and  $0.2$ . This is very interesting, because  $D_K$  does not take the orbital frequency change due to the disk pressure into account and assumes a Keplerian disk. For a large planet mass ratio the behaviours differ from the simulations. The insertion into Ward8 always results in inward migration. The usage of GT79 leads to a 4 matching direction, especially for higher planet mass ratios, which is not observed when inserting other LR location equations. Nevertheless, only two of the four calculations showed an overall right behaviour, while the other two predicted an early stopping of migration.

Inserting  $D_{*,p}$  into Ward3 the compared behaviours are almost the same as when inserting  $D_K$ , but with one less match, even though  $D_{*,p}$  is more coherent. The insertion of  $D_{*,p}$  into Ward8, the approximation of Ward3, does in contrary only lead to a few matching behaviours, mainly for  $h_0 = 0.07$ . Using GT79 only predicts inward migration. Furthermore in more calculations was a stopping of the migration predicted, than actually observed in the hydrodynamic simulations.

Lastly, higher orders of the Fourier components of the potential are used, which are proportional to the eccentricity. The average eccentricity for each simulation was determined during the time the planets were in MMR. Then the simulations were compared to the one of the 4 available options,  $e = 0.025, 0.05, 0.075$  or  $e = 0.1$ , for which the simulation's eccentricity was closest to. Nevertheless the behaviour does never match the simulations, since the outer torque given by  $l = m - 1$  is always several orders of magnitude bigger than the inner torque given by  $l = m + 1$  and  $l = m$ .

In conclusion, GT79 does not seem to be able to correctly predict the migration behaviour. Additionally, the LR location equations  $D$  and  $D_p$  are seemingly too simplified to give the correct behaviour. The equation which take the disk pressure fully into account,  $D_{*,p}$ , as well as  $D_K$  give more matching migration behaviours, especially when inserted into the most general torque equation, Ward3. One can conclude, that the consideration of the epicycle frequency change due to the disk pressure is more important than the orbital frequency change. Nevertheless, considering only change in orbital frequency changes the results so that they are less fitting. The approximations done by [Ward \[1997\]](#) to arrive at Ward8 may be applicable with  $D_p$  and  $D_K$ .

For low viscosities the calculated migration behaviour is never correct. The deviation from

the simulations with low  $\alpha$  was to be expected, since several new effects which may influence the migration appear.

### 5.1.2 Comparison of the migration rates

In this section, the simulations migration rates and the theoretical model rates are being compared at one specific  $r_p$  of the inner planet. In order to do that, for each simulation the region of  $r$  in which the planets are locked in an MMR resonance was determined. In this region, the rates were calculated over a span of a few hundred orbits, ranging from 200 to 500. While a span of 500 orbits was aimed at, due to the fact that some simulations are only very shortly in MMR, this was not always possible.

The ratio of the theoretical rate and the one obtained from the simulations are plotted onto a symlog axis, which allows to plot negative ratios on a log scale. The axis is linear in a range from  $-1\%$  to  $1\%$ . This grants the possibility to plot a wide range of ratios while it is still easy to determine if the two rates have the same sign. After analyzing each plot, the calculation whose rate comes closest to the one from the simulations and have the same sign will be listed in a table. For these selected calculations, the difference from the simulations will be given in percentage.

First using the resonant locations given by  $D$ , Fig. 5.10 shows the ratio of the theoretical rates and the rates obtained from the simulations.

It can be observed, that besides the theoretical approach using Ward8 with Sigmaratio = 0.2 and one from Ward3, every other calculation has the wrong sign, meaning they predict the wrong migration direction. The calculations which haven an equal migration direction as the simulations are still often far off. Overall, the calculations using Ward8 with Sigmaratio = 0.2 are most consistently close to the simulations. For *theory\_4*, which has a higher aspect ratio  $h_0 = 0.07$ , Ward8 with Sigmaratio = 0.1 gets closest to the simulation rate, even almost matching it.

In general  $D$  does not assume the disk pressure, but the simulations do, see Eq. (2.6). For this reason, it is not surprising that the usage of  $D$  does not lead to close approximations. Table 5.1 shows the best calculation methods are listed for each simulation. The deviation in percentage is calculated using:

$$\frac{\dot{a}_{\text{result}} - \dot{a}_{\text{simulation}}}{\dot{a}_{\text{simulation}}} \cdot 100. \quad (5.2)$$

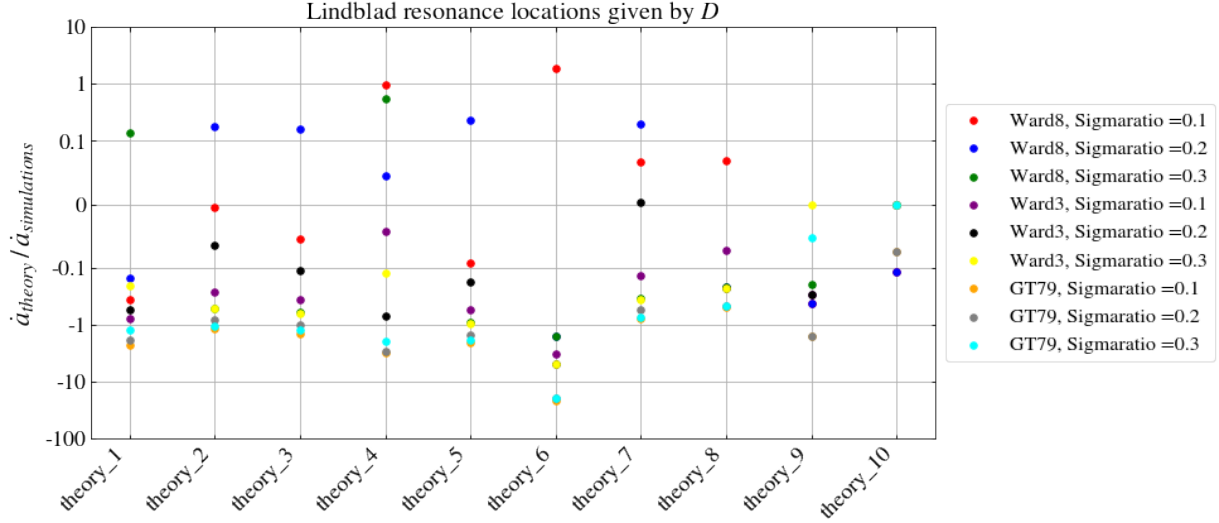


Figure 5.10: Ratio of the migration rates, one given by the author's theoretical approach, the other one from the simulations. The labels give the torque and Sigmaratio used in each calculation.

Table 5.1: Best theoretical rates with the usage of  $D$

simulation name	best calculation method using $D$	deviation [%]
<i>theory_1</i>	Ward8, Sigmaratio = 0.3	86.28
<i>theory_2</i>	Ward8, Sigmaratio = 0.2	82.61
<i>theory_3</i>	Ward8, Sigmaratio = 0.2	83.70
<i>theory_4</i>	Ward8, Sigmaratio = 0.1	2.35
<i>theory_5</i>	Ward8, Sigmaratio = 0.2	77.07
<i>theory_6</i>	Ward8, Sigmaratio = 0.1	88.21
<i>theory_7</i>	Ward8, Sigmaratio = 0.2	80.60
<i>theory_8</i>	Ward8, Sigmaratio = 0.1	93.15
<i>theory_9</i>	-	-
<i>theory_10</i>	-	-

List of calculations, which were closest to the simulation rate for each simulation. This table corresponds to Fig. 5.10

For  $D_p$ , all calculations have the wrong migration direction, performing even worse than the calculations using  $D$ . This may be due to the fact that  $D_p$  only takes the change of orbital frequency. Since there is no calculation resulting in the correct sign, no table listing the best calculations is needed.

Then, using the second equation giving the LR locations with partially considered disk pressure,  $D_K$ , is compared to the simulations. This is shown in Fig. 5.11.

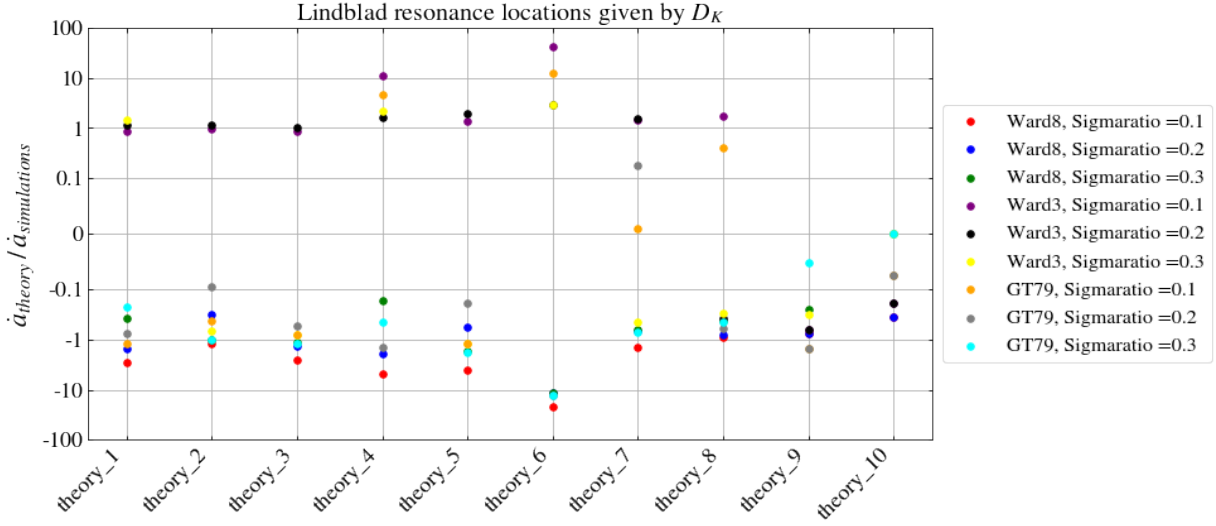


Figure 5.11: Ratio of the migration rates, one given by the author's theoretical approach, the other one from the simulations. The labels give the torque and Sigmaratio used in each calculation.

While inserting  $D_K$  into the torques, using Ward3 almost always provides the right direction of migration, the ones with Sigmaratio = 0.2 and Sigmaratio = 0.1 are closest to most simulations. Additionally, a few calculations using GT79 with Sigmaratio = 0.1 and Sigmaratio = 0.2 have the same direction, which has not been the case for the other LR locations. Moreover, the rates of *theory\_4* and *theory\_6* are overestimated by the model more than the others. Inserting  $D_K$  into Ward8 never gives the correct sign of the rate. Therefore, the approximations done by Ward [1997] to retrieve Ward8 out of Ward3 seems to not produce adequate results in combination with  $D_K$ . In Table 5.2 the calculations, which approximated the value of simulations the best, are listed.

Table 5.2: Best theoretical rates with the usage of  $D_K$ 

simulation name	best calculation method using $D_K$	deviation [%]
<i>theory_1</i>	Ward3, Sigmaratio = 0.1	12.43
<i>theory_2</i>	Ward3, Sigmaratio = 0.1	4.86
<i>theory_3</i>	Ward3, Sigmaratio = 0.2	3.77
<i>theory_4</i>	Ward3, Sigmaratio = 0.2	59.77
<i>theory_5</i>	Ward3, Sigmaratio = 0.1	33.55
<i>theory_6</i>	Ward3, Sigmaratio = 0.3	194.12
<i>theory_7</i>	Ward3, Sigmaratio = 0.1	43.69
<i>theory_8</i>	Ward3, Sigmaratio = 0.1	59.73
<i>theory_9</i>	-	-
<i>theory_10</i>	-	-

List of calculations, which were closest to the simulation rate for each simulation. This table corresponds to Fig. 5.11

Using  $D_{*,p}$  for the LR locations takes the disk pressure fully into account, matches the simulations the most. They are shown in Fig. 5.12.

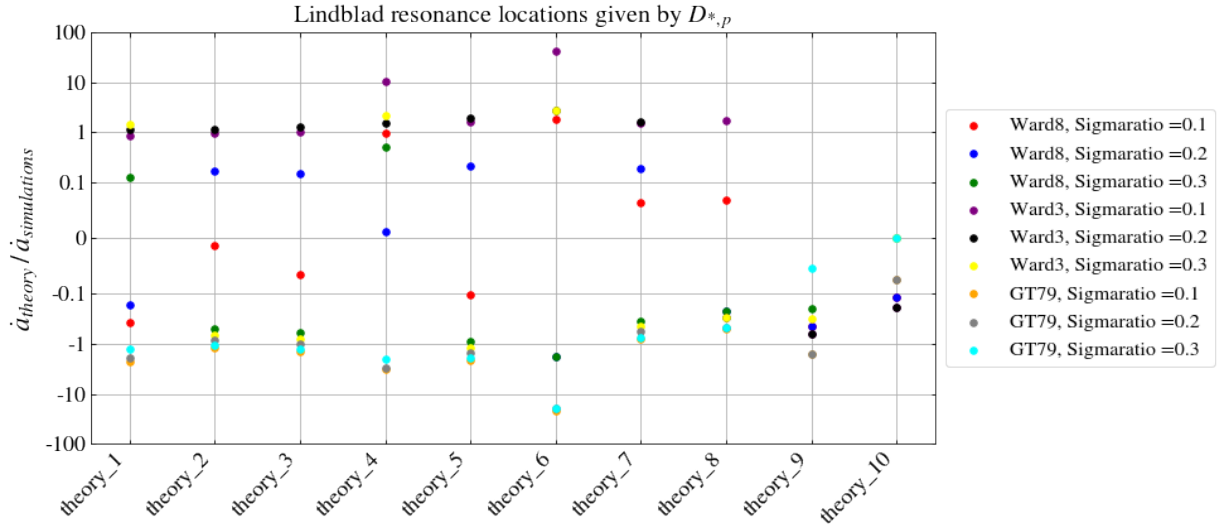


Figure 5.12: Ratio of the migration rates, one given by the authors theoretical approach, the other one from the simulations. The labels give the torque and Sigmaratio used in each calculation.

In contrary to the usage of  $D$  or  $D_p$  and as seen with  $D_K$ , over a third of the calculations rates have the same sign. Especially the rates given by Ward3 with Sigmaratio = 0.1 get consistently very close. Overall, the calculations done by these two give the best approximations for the most simulations. Interestingly, for the simulation *theory\_4*, where  $D$  is very fitting, Ward3 with Sigmaratio = 0.2 overestimates the migration rate. While some rates given by Ward8 also have the correct sign, this does not apply to the usage of GT79. In table 5.3 the best calculations for each simulation are listed.

Table 5.3: Best theoretical rates with the usage of  $D_{*,p}$

simulation name	best calculation method using $D_{*,p}$	deviation [%]
<i>theory_1</i>	Ward3, Sigmaratio = 0.2	11.98
<i>theory_2</i>	Ward3, Sigmaratio = 0.1	6.20
<i>theory_3</i>	Ward3, Sigmaratio = 0.1	2.24
<i>theory_4</i>	Ward8, Sigmaratio = 0.1	1.88
<i>theory_5</i>	Ward3, Sigmaratio = 0.1	58.04
<i>theory_6</i>	Ward8, Sigmaratio = 0.1	81.47
<i>theory_7</i>	Ward3, Sigmaratio = 0.1	52.09
<i>theory_8</i>	Ward3, Sigmaratio = 0.1	73.39
<i>theory_9</i>	-	-
<i>theory_10</i>	-	-

List of calculations, which were closest to the simulation rate for each simulation. This table corresponds to Fig. 5.12

Lastly, higher eccentricities were taken into account while using GT79. For the four eccentricities 0.025, 0.05, 0.075 and 0.1, the orders  $l = m \pm 1$  from Sect. 2.3.2 were included. No rate from the calculations has the correct sign, and they all seem to overestimate the outer torque by a few magnitudes as seen during the comparison of the rates.

For the last two simulations, *theory\_9* and *theory\_10*, with the lower viscosities, every calculation performed badly. This is not surprising, as the disks from these two can be considered close to being inviscid, which adds new effects to the migration of planets. Since the theoretical approach assumes a viscous disk, its results do not fit the simulations.

The presented analyses of the rate at one location and the general migration behaviour can now be compared to each other. By doing so, it can be determined if a migration rate is close to a rate from the simulations due to a coincidence or if the general migration behaviour also fits the simulation. This amounts to a more complete picture whether the theoretical model by the author provides a usable method to predict the migration of two planets. In the following, the rates at a specific location are compared to the overall migration behaviour, for those which have the same sign.

Comparing the analysis of the migration rates at one location and the overall behaviour of the migration, several similarities can be found. In general, for low viscosities neither the rates at one location, nor the general behaviour was correctly observed in any calculation from the theoretical model. This further underlines that the theoretical approach is not capable of showing the very complicated behaviour for low viscosities. Additionally, the partial and incoherent disk pressure consideration in  $D_p$  and the eccentricities incorporation never led to a proper outcome. The latter because of the Laplace coefficient's second derivative diverging.

For  $D$ , most rates at one  $r_p$  had the same behaviour apart for *theory\_4*, *theory\_7*, *theory\_8* and *theory\_1*. For the first two, more rates at one location had the correct sign as there were calculations with the overall fitting migration behaviour. For *theory\_1*, the two analysis results don't match while for *theory\_8* only the predicted migration direction was correct. When using  $D_K$  the general direction of migration matched all the calculations which predicted the migration direction at one location correctly, besides for *theory\_1* and *theory\_7*. For those two the predicted direction of migration at one location agreed more with the hydrodynamic simulations than the overall migration behaviour. Lastly, the LR locations given by  $D_{*,p}$  show a mostly matching overall migration behaviour for the rates at one location, for all simulations except for *theory\_1*, *theory\_7* and *theory\_8*, which showed a matching behavior for fewer calculations.

In conclusion, the two best combinations for calculating the migration rate for two planets, using simulations without the BM08 module, are  $D_{*,p}$  and  $D_K$  with the torque Ward3. For those, the deviation in percentage is plotted for all simulations. Only the calculations where the rate has the correct sign are plotted in Fig. 5.13 and Fig. 5.14.

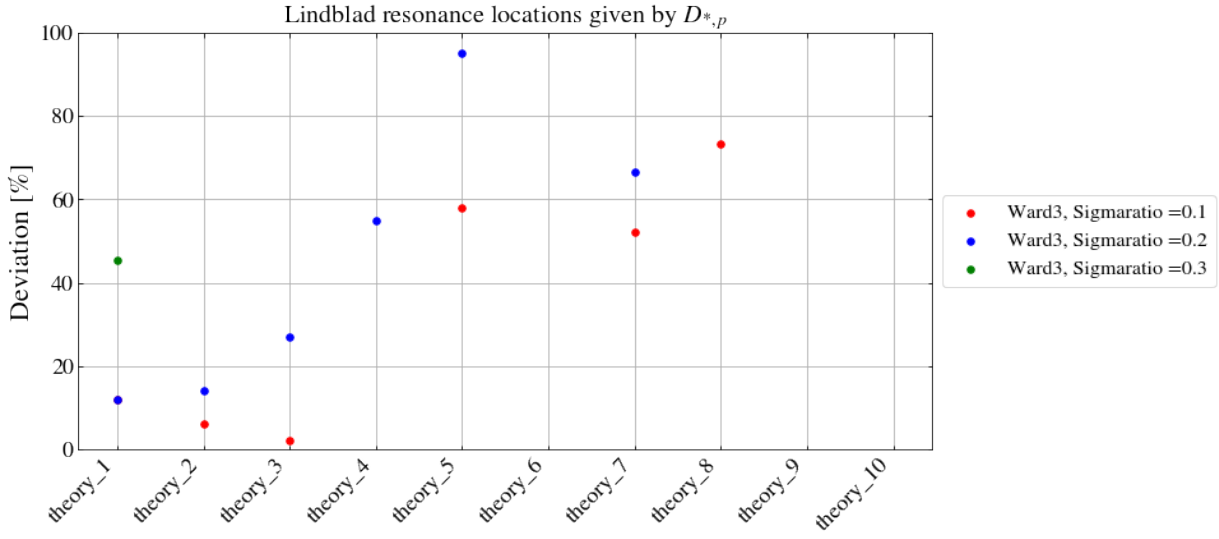


Figure 5.13: Deviation of the calculated migration rate in percentage from each simulation. Only the ones where Ward3 was used and which had the right sign are shown. The labels give the torque and Sigmaratio used in each calculation.

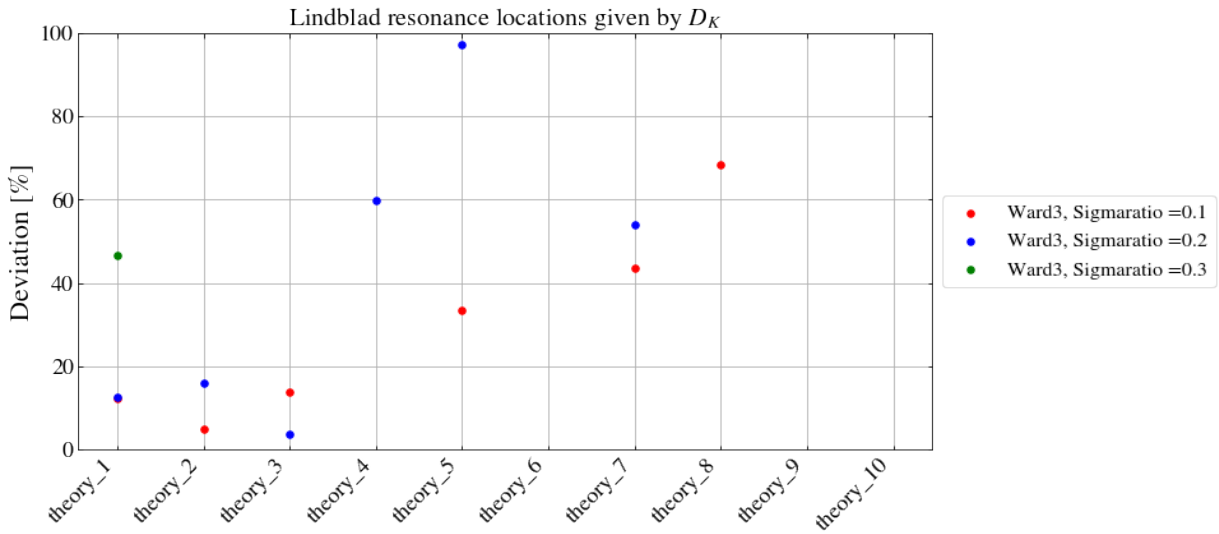


Figure 5.14: Deviation of the calculated migration rate in percentage from each simulation. Only the ones where Ward3 was used and which had the right sign are shown. The labels give the torque and Sigmaratio used in each calculation.

## 5.2 Setups *BM08theory*

### 5.2.1 Comparison of the general outcome of migration

Next, the same migration behaviour analysis will be done for the simulations ran with the BM08 module. Since this module leads to the LR location shift and influences the torque calculation, different outcomes of the simulations are expected.

#### Evaluation of the Simulations

Most simulations with the module stopped migrating and the planets maintained their semi-major axes. Here, they first may overshoot the stopping radius and then they migrate inwards and repeat these steps until their migration rate is slow enough so that they don't over or undershot the stopping radius. As an example of a stalling migration, where they level off, *BM08theory\_2* will be shown in Fig. 5.15 to Fig. 5.17.

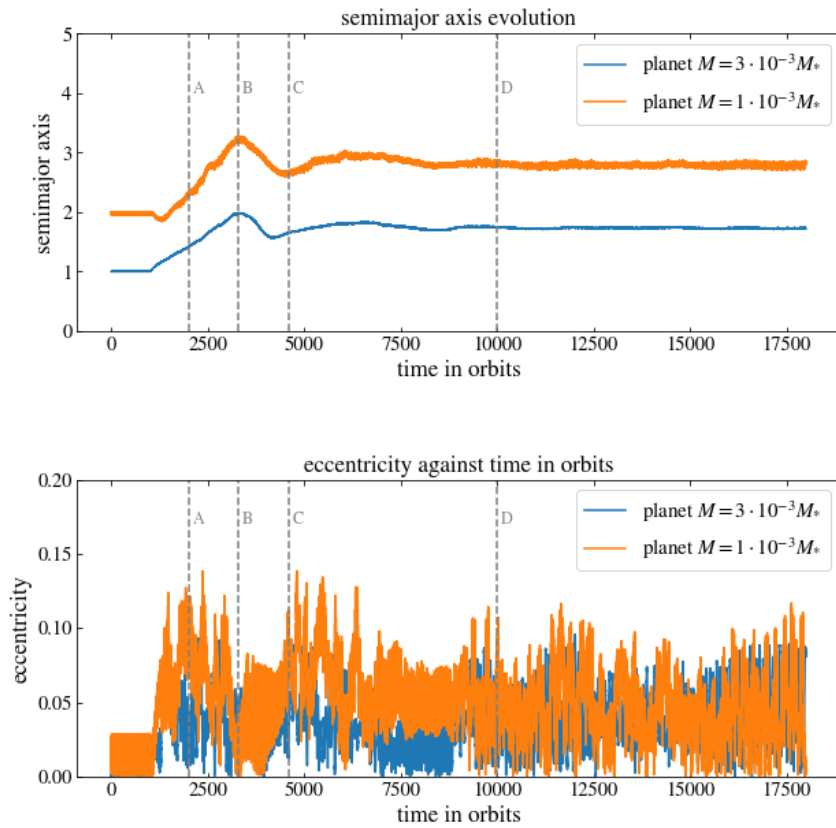


Figure 5.15: Semi-major axis and eccentricity evolution over 18,000 orbits. The dashed lines mark the number of orbits, where the surface density is plotted.

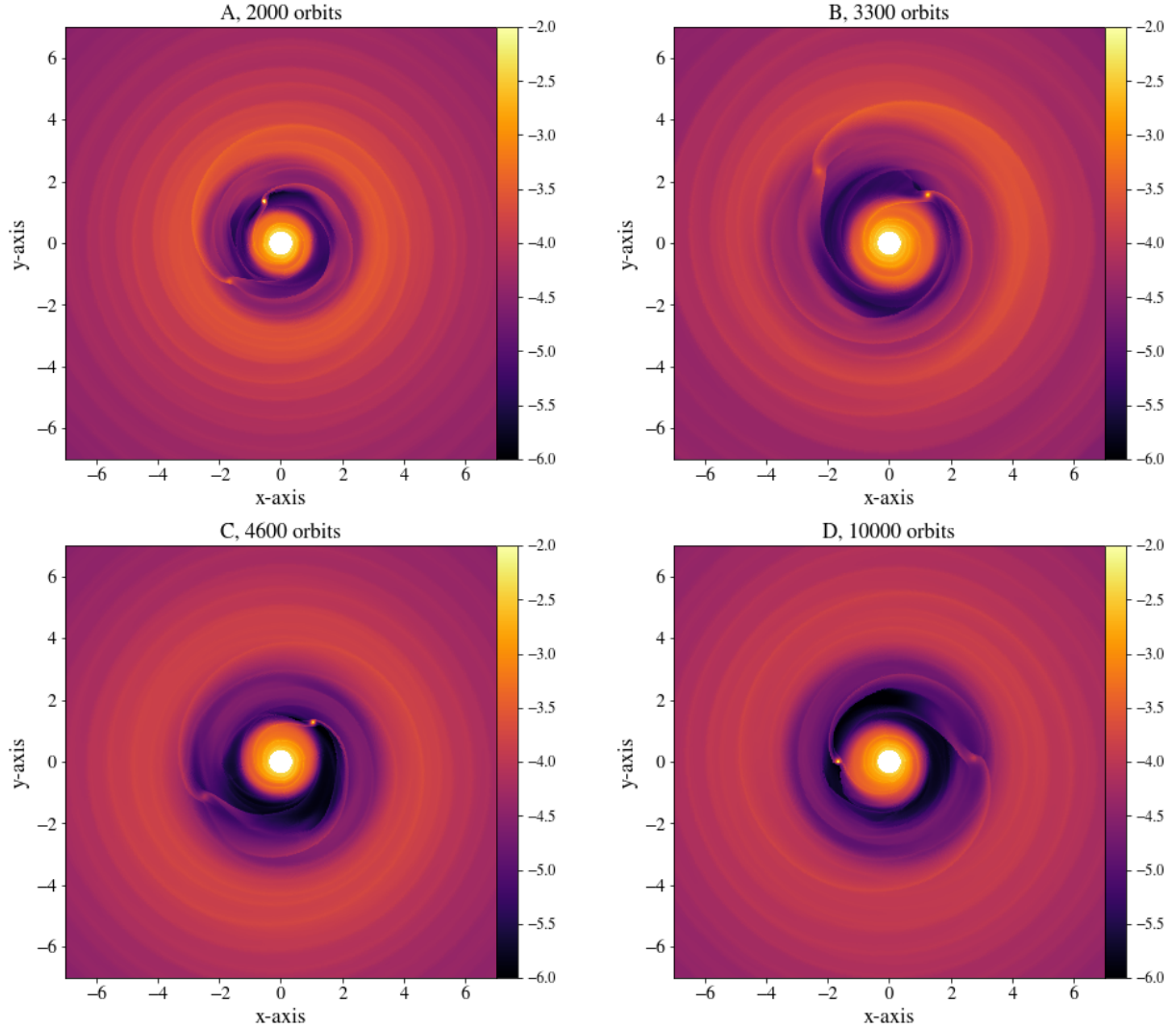


Figure 5.16: Disk surface density in a region from  $[-7,7]$  in x and y direction after different orbits. The surface densities value is indicated by the color range, whose values are the exponents for a logscale with the base 10.

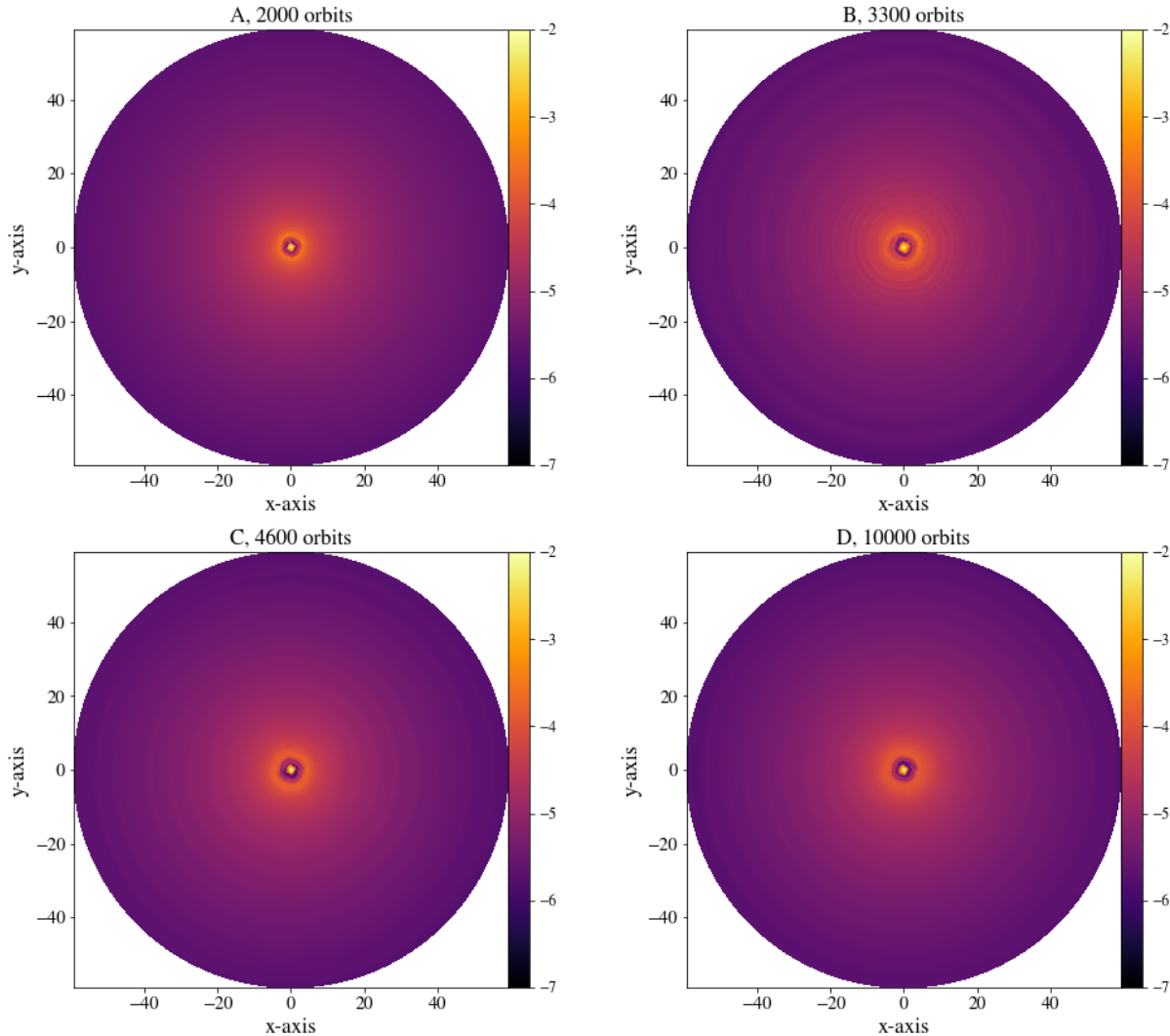


Figure 5.17: Disk surface density after different orbits. The surface densities value is indicated by the color range, whose values are the exponents for a logscale with the base 10. After 3300 orbits, the density waves exerted at the LR locations are visible as they travel throughout the disk.

After 1000 orbits, the inner planet migrates outwards, while the outer planet migrates inwards and catches the inner planet in an MMR resonance after 1300 orbits. Most of the time the planets are locked in a 2:1 MMR during their outward migration. The rapidly librating eccentricity, especially of the outer planets, seems to disturb this. The planets seem to migrate outwards so fast, that they miss the stalling radius the first time and migrate outwards a bit further. After 3300 orbits, they migrate inwards again but they are not locked in an MMR during this. Only after 4500 orbits they are in a 2:1 MMR again, now slowly migrating outwards. This time, the migration rate seems to be slow enough, that they only overshot their stopping radius by a little bit. After undershooting  $r_c$  again around 7500 orbits, they find their equilibrium state around 12000 orbits and stop migrating. Up to 15500 orbits they are still in and out of MMR, but they only change their semi-major axis very slowly, and very little. After 15500 orbits, they are not in MMR anymore. Alternatively the planets stop migrating as shown in Fig. 5.4

The semi-major axis development for *BM08theory\_4* and *BM08theory\_9*, which both experienced close encounters, is very similar to the behaviour shown in Fig. 5.1. An especially interesting behaviour shows *BM08theory\_10* in Fig. 5.18 to Fig. 5.20.

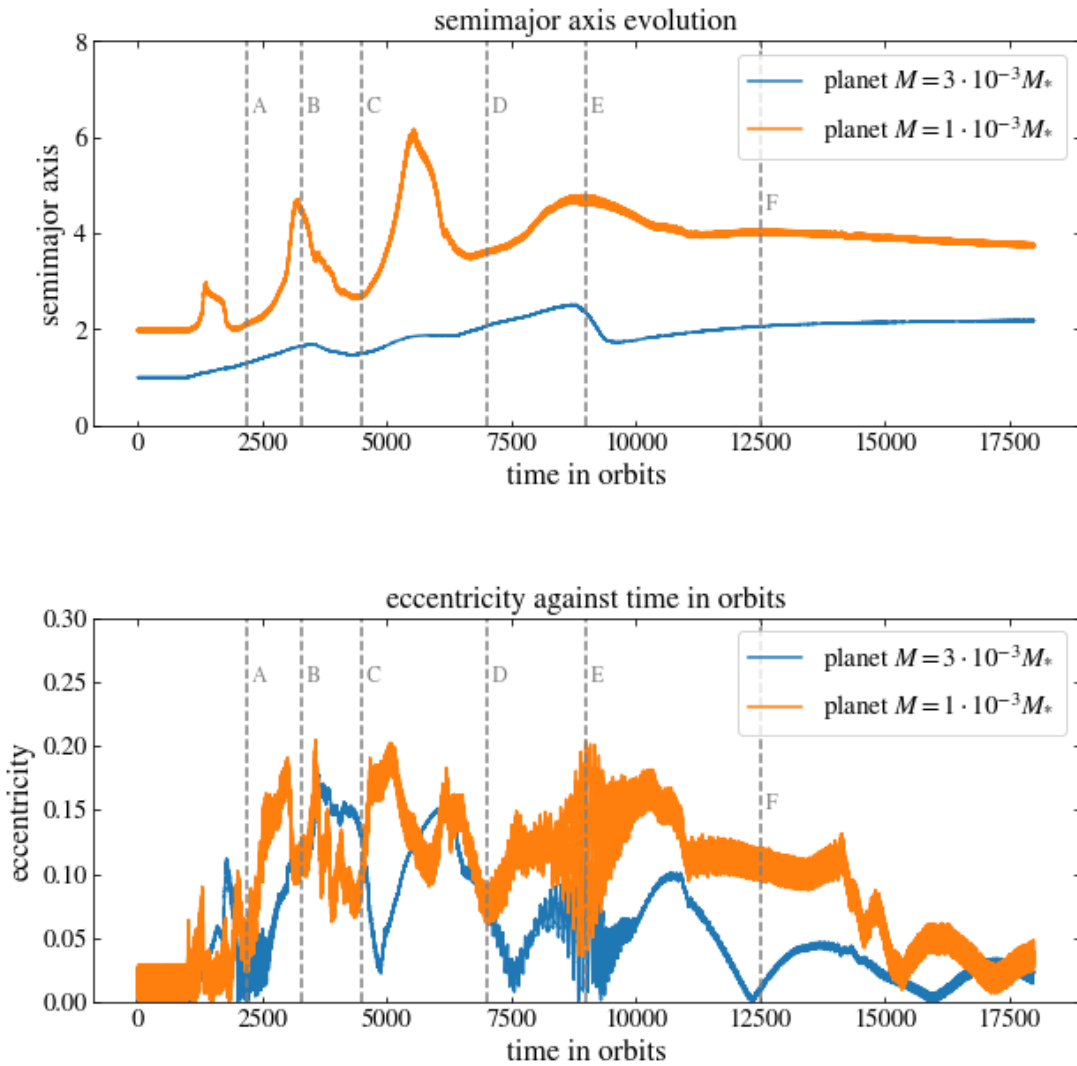


Figure 5.18: Semi-major axis and eccentricity evolution over 18,000 orbits. The dashed lines mark the number of orbits, where the surface density is plotted.

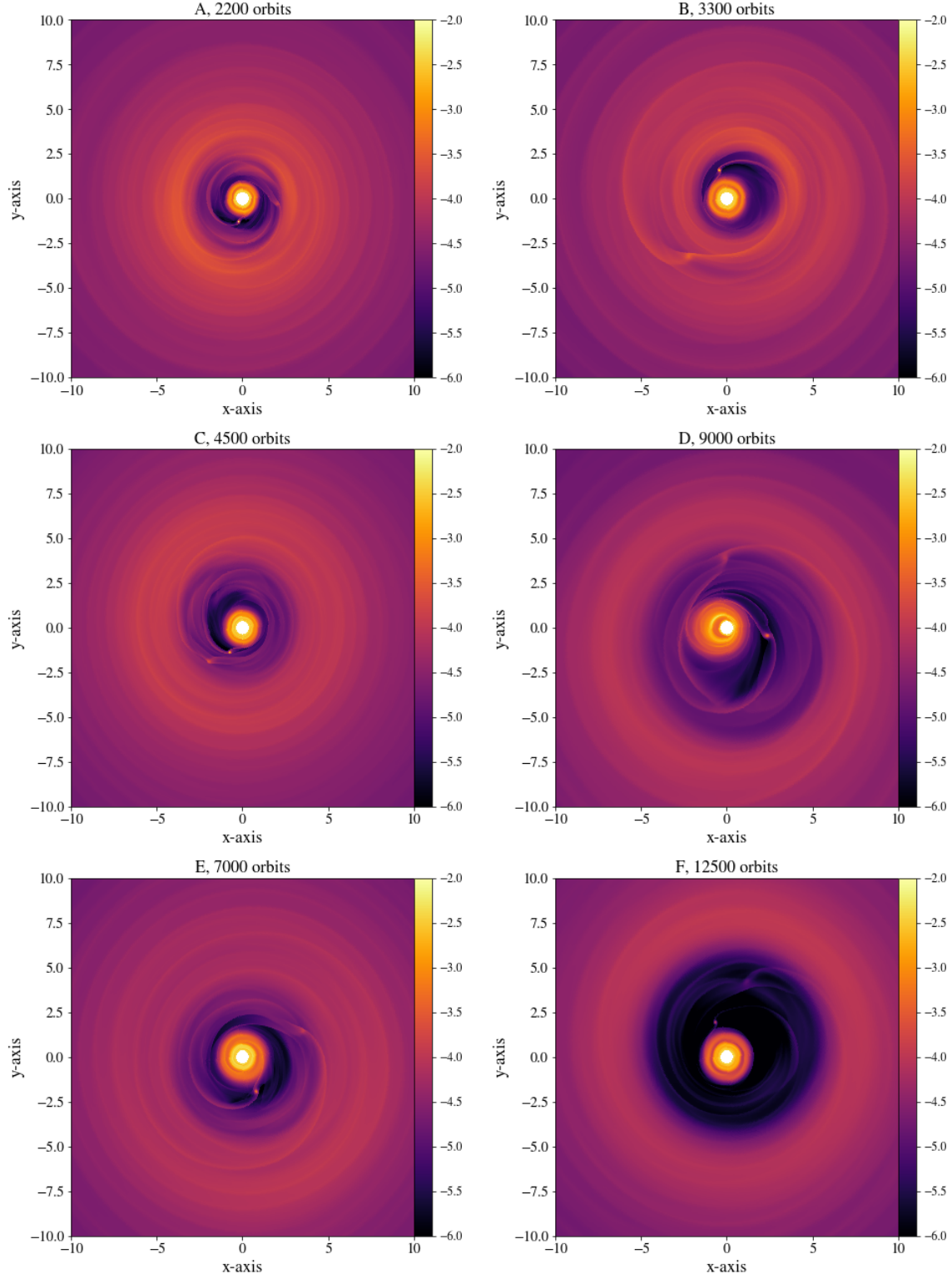


Figure 5.19: Disk surface density in a region from  $[-10, 10]$  in x and y direction after different orbits. The surface densities value is indicated by the color range, whose values are the exponents for a logscale with the base 10. After 3300 orbits, the disk seems to be asymmetric. Around 9000 orbits, the surface density distribution is similar to the one of Fig. 5.16

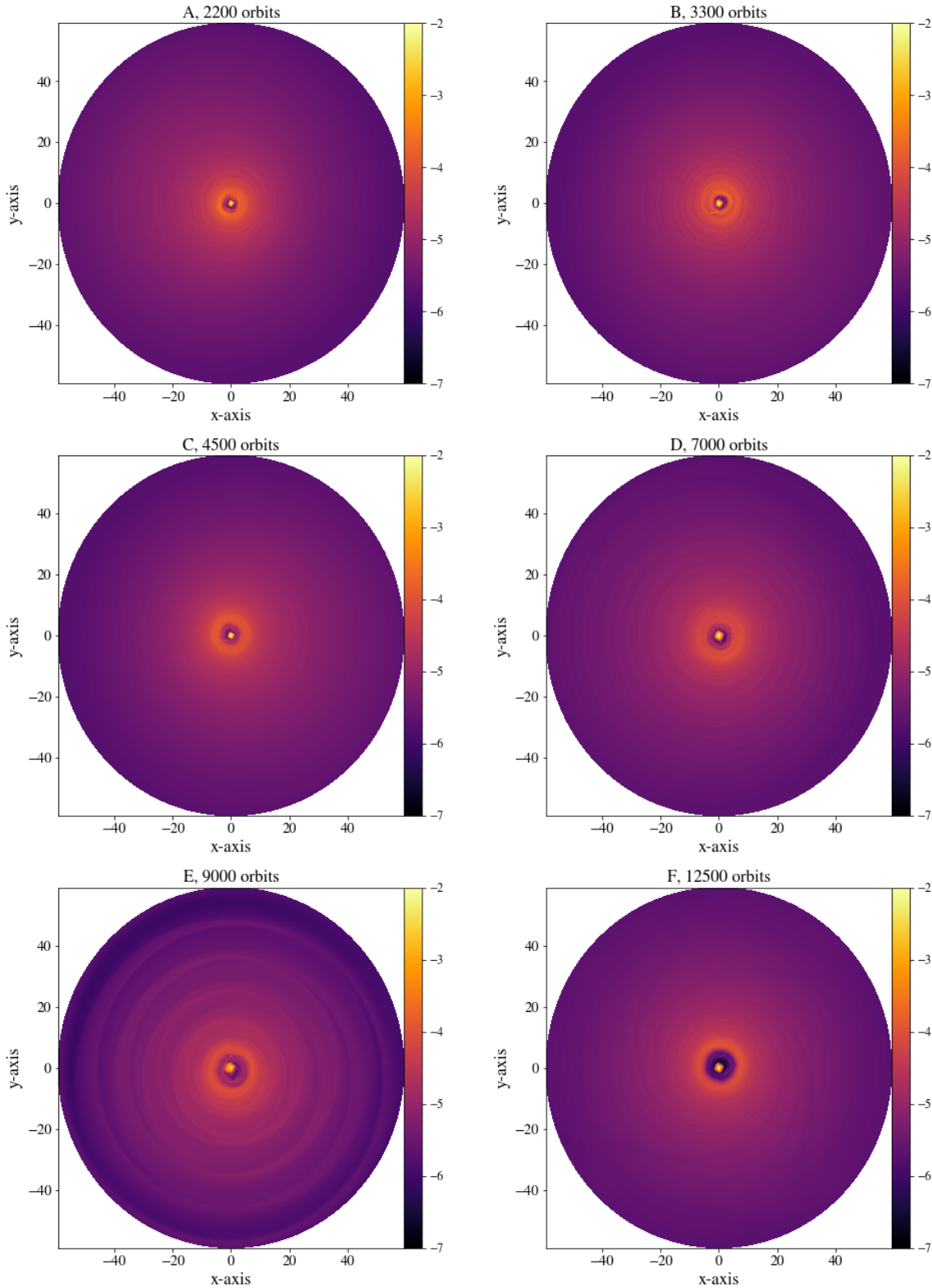


Figure 5.20: Disk surface density after different orbits. The surface densities value is indicated by the color range, whose values are the exponents for a log scale with the base 10. After 3300 orbits, the disk seems to be asymmetric. Around 9000 orbits, the surface density distribution is similar to the one from Fig. 5.16

In contrary to the simulations presented in Sect. 5.1.1, the outer planet does not migrate inwards after the planets can interact with the disk and each other. There is an almost instant migration jump, during which the inner planet migrates outwards. They do three further jumps and generally migrate outwards together, where they were mostly in 2:1 MMR. The resonance disturbances may be caused by the growing and librating eccentricity at times. After the last migration jump, which happens around 9000 orbits, they are mostly in 2:1 MMR resonance. When they are not, no resonance at all could be detected. After 15000 orbits, they are no longer in MMR and it seemingly the distance between the planets slowly gets smaller. Most likely, they would be caught in an MMR again. Furthermore, it can be observed that the eccentricity changes almost periodically, while moving in a range from  $e = 0$  to  $e = 0.2$ . Especially the inner planet's eccentricity follows the described course. The eccentricity does not only change periodically, but it also increases during the 3 migration jumps around 3500, 6000 and 9000 orbits. As a consequence of the jumps, the gas density seems to be disturbed more and more. Around 9000 orbits, the gas density distribution is similar to the one from Fig. 5.16. After the jumps, the common gap is still asymmetric but not as much as at 9000 orbits. Therefore, the disk seems to stabilise itself again, which is also visible in the semi-major axis evolution.

Overall, the systems show a very complex migration behaviour with migration jumps and being in and out of MMR. It was to be expected that during the inward migration they are not locked in an MMR resonance, since they would then migrate outwards together, following the Masset and Snellgrove mechanism.

### Comparison of the migration behaviour

Starting the comparison by using  $D$  for the LR locations and inserting it into Ward3 or GT79 does not lead to a matching migration behaviour. In both cases, inward migration is always predicted. Using Ward8 gives occasional matches, but no clear structure of matching behaviour is visible. Moreover, in only one case the migration stopped in the theoretical approach, which is far from the fifteen expected simulated cases.

Similarly to the simulations without the BM08 module, the insertion of  $D_p$  does not lead to a match in a single case. Again, this is probably on the grounds of the disk pressure's incomplete consideration.

Using  $D_K$  inserted into Ward3 gives a matching conduct for  $h_0 = 0.07$  (setup *BM08theory-4*) and  $\Sigma_0 = 10^{-4}$  (setup *BM08theory-5*) and several other migration directions. Inserting

it into Ward8 predicts inward migration. Using GT79, scattered theoretical calculations show the right migration direction, but end their migration not as seen in the simulations.

Inserting  $D_{*,p}$  into Ward3 is very similar to  $D_K$  with the exception of the setup *BM08theory\_6*. While the migration direction is similar for quite a few simulations, in none of the theoretical calculations a stalling appears while using Ward3. The insertion into Ward8 matches not as many setups as Ward3 and it also forecasts a stopping more often. The torque from [Goldreich and Tremaine \[1979\]](#) underestimates the migration rates, leading to inward migration, which does not match the expectations.

With the consideration of eccentricities, the outer torque is overestimated by a few magnitudes, leading to inward migrations in the theoretical approach which is not reciprocated in the simulations. Additionally, for lower viscosities the theoretical calculations could still not predict the correct migration behaviour, due to the added effects in inviscid disks.

In general, most of the theoretical approached predictions matched the behaviour even less precisely than without the BM08 module. Even though this stabilised the disk in the simulations, and the planets migration direction is predicted correctly, the ending of the migrations is what can't be predicted correctly by the theoretical approach.

### 5.2.2 Comparison of the migration rates

As done with all the simulations without the BM08 module, the calculations from the theoretical approach will be compared to the migrations rates from the simulations. Again, the rate from the simulations was evaluated over a period of 200 to 500 orbits, in which the planets where resonant locked. Like before, these deviations are happening because in some simulations the planets were only very shortly clearly resonance locked. The evaluation structure follows the one presented in Sect. 5.1.

The results of inserting  $D$  into the torques and receiving the migration rates are shown in Fig. 5.21.

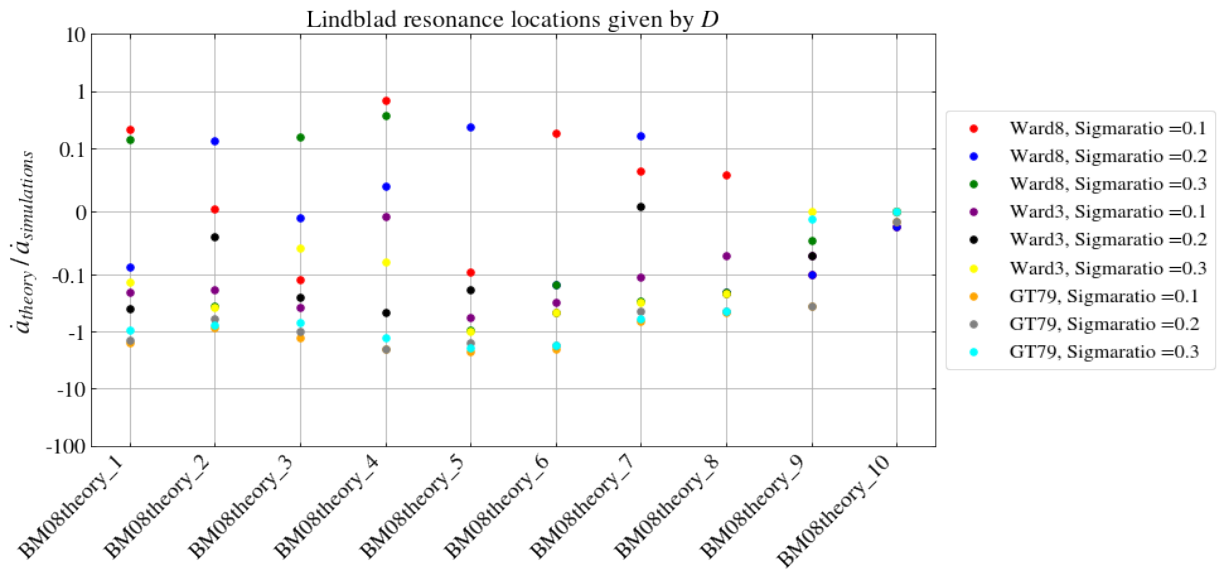


Figure 5.21: Ratio of the migration rates, one given by the author's theoretical approach, the other one from the simulations. The labels give the torque and Sigmaratio used in each calculation.

Almost the only torque equation, which grants the right sign of the theoretical migration rate, is Ward8. The exception is given by Ward3 with  $\text{Sigmaratio} = 0.2$  compared to the rate from *BM08theory\_7*. Even though some calculations have the same sign as the simulations, only when compared to *BM08theory\_4*, the calculated rate gets significantly close. Especially Ward8 with  $\text{Sigmaratio} = 0.1$  rate matches almost exactly. The best rates which are closest to the simulation are listed in table 5.4.

Table 5.4: Best theoretical rates with the usage of  $D$ 

simulation name	best calculation method using $D$	deviation [%]
<i>BM08theory_1</i>	Ward8, Sigmaratio = 0.1	78.95
<i>BM08theory_2</i>	Ward8, Sigmaratio = 0.2	86.72
<i>BM08theory_3</i>	Ward8, Sigmaratio = 0.3	84.64
<i>BM08theory_4</i>	Ward8, Sigmaratio = 0.1	32.85
<i>BM08theory_5</i>	Ward8, Sigmaratio = 0.2	76.39
<i>BM08theory_6</i>	Ward8, Sigmaratio = 0.1	81.70
<i>BM08theory_7</i>	Ward8, Sigmaratio = 0.2	83.25
<i>BM08theory_8</i>	Ward8, Sigmaratio = 0.1	94.27
<i>BM08theory_9</i>	-	-
<i>BM08theory_10</i>	-	-

List of calculations, which were closest to the simulation rate for each simulation. This table corresponds to Fig. 5.21

The equation still does not take the disk pressure into account and since the module BM08 doesn't remove the disk pressure,  $D$  doesn't describe the disks physical conditions very well. Because of that, it is not surprising that most calculated rates don't get closer as 77% to the simulations.

Following, the LR locations given by  $D_p$  are inserted. As seen with the simulations without the BM08 module, every calculation gives the wrong migration direction. Thus no table is needed.

After that, the other derived equation which partially considers the gas pressure,  $D_K$ , is used for the calculation. The results are in Fig. 5.22.

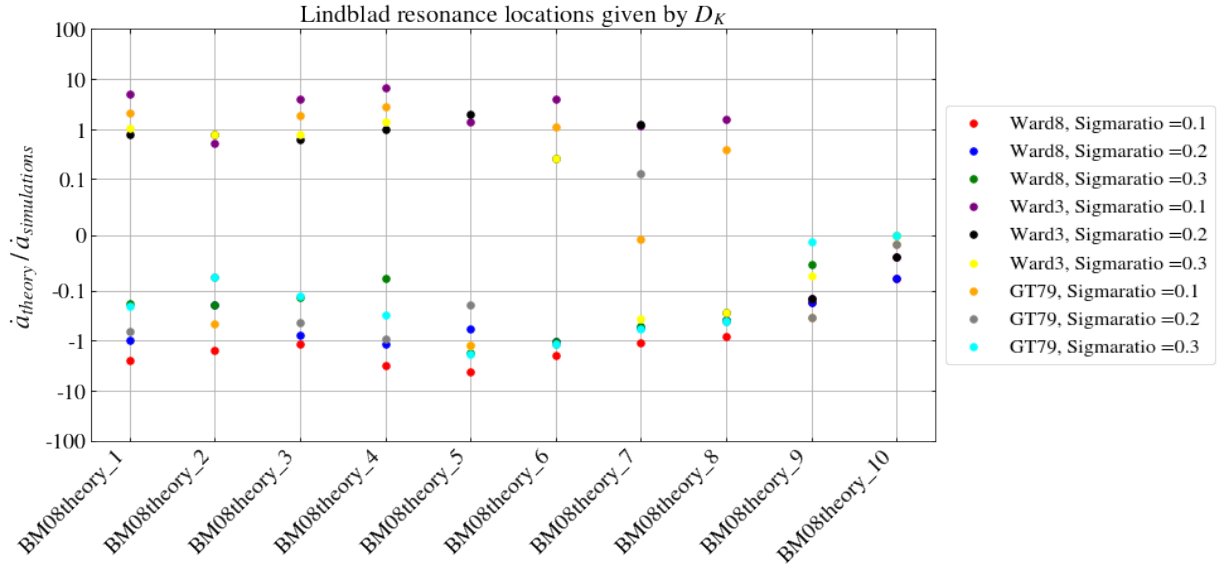


Figure 5.22: Ratio of the migration rates, one given by the author's theoretical approach, the other one from the simulations. The labels give the torque and Sigmario used in each calculation.

It is clearly visible that the calculations which have the same sign mostly overestimate the rate. This seems to be a consequence of an overestimated inner torque. The usage of Ward3 with Sigmario = 0.2 and Sigmario = 0.3 seems to give the rates, which are most consistently close to the simulations. Additionally, Ward3 and GT79 with Sigmario = 0.1 and also produce acceptable rates more often than not. In contrast to the use of other LR location equations, Ward8's rates do not have the anticipated sign. This was also observed without the BM08 module and further strengthens the assumption that the simplifications done to receive Ward8 do not work adequately with  $D_K$ . The best fitting calculations are in table 5.5.

Table 5.5: Best theoretical rates with the usage of  $D_K$ 

simulation name	best calculation method using $D_K$	deviation [%]
<i>BM08theory_1</i>	Ward3, Sigmaratio = 0.3	3.33
<i>BM08theory_2</i>	Ward3, Sigmaratio = 0.3	21.03
<i>BM08theory_3</i>	Ward3, Sigmaratio = 0.3	19.35
<i>BM08theory_4</i>	Ward3, Sigmaratio = 0.2	1.48
<i>BM08theory_5</i>	Ward3, Sigmaratio = 0.1	38.40
<i>BM08theory_6</i>	Ward3, Sigmaratio = 0.1	10.30
<i>BM08theory_7</i>	Ward3, Sigmaratio = 0.1	15.21
<i>BM08theory_8</i>	GT79, Sigmaratio = 0.1	57.13
<i>BM08theory_9</i>	-	-
<i>BM08theory_10</i>	-	-

List of calculations, which were closest to the simulation rate for each simulation. This table corresponds to Fig. 5.22

Lastly inserting  $D_{*,p}$ , considering the disk pressure fully, leads to the results shown in Fig. 5.23.

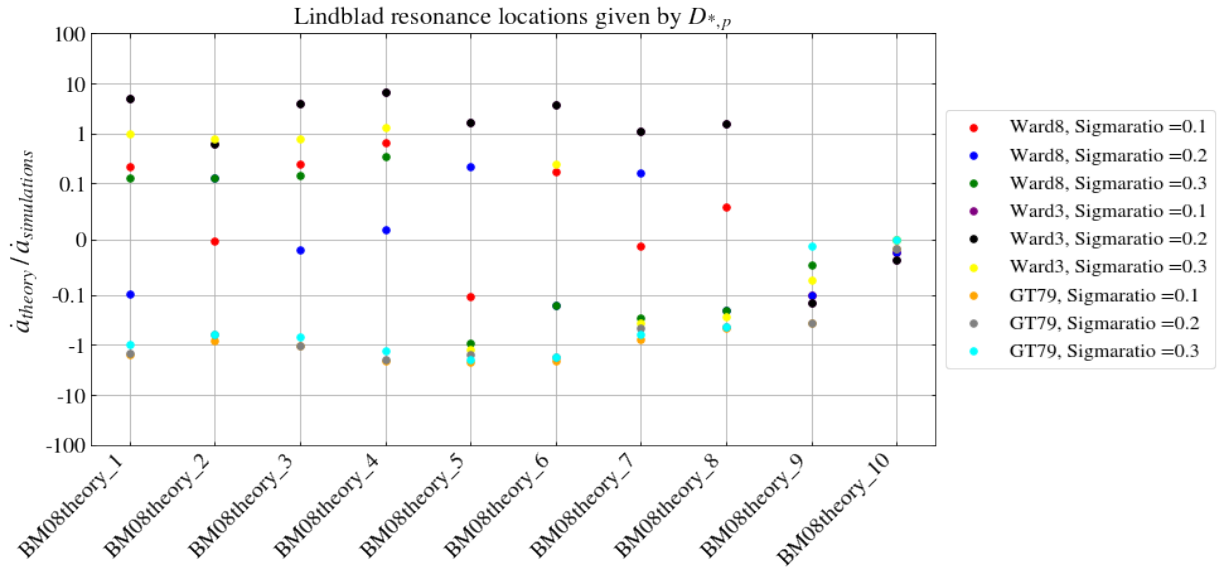


Figure 5.23: Ratio of the migration rates, one given by the author's theoretical approach, the other one from the simulations. The labels give the torque and Sigmaratio used in each calculation.

where roughly a third of the theoretical calculations have the correct sign. Especially Ward3 with Sigmaratio = 0.3 and Sigmaratio = 0.2 deliver these most consistently. Addi-

tionally using Ward8 with Sigmaratio = 0.3 give rates with the same sign for the first four simulations, too. Also Ward8 with Sigmaratio = 0.1 more often than not gives rates with the same sign. It also appears that for higher planet mass ratios than three, which applies to the simulations *BM08theory\_7* and *BM08theory\_8*, and for the simulation with a lower surface density, *BM08theory\_5*, the usage of Ward3 with Sigmaratio = 0.3 performs worse than for previous simulations. The best calculations are listed in table 5.6.

Table 5.6: Best theoretical rates with the usage of  $D_{*,p}$

simulation name	best calculation method using $D_{*,p}$	deviation [%]
<i>BM08theory_1</i>	Ward3, Sigmaratio = 0.3	1.62
<i>BM08theory_2</i>	Ward3, Sigmaratio = 0.3	22.52
<i>BM08theory_3</i>	Ward3, Sigmaratio = 0.3	20.42
<i>BM08theory_4</i>	Ward8, Sigmaratio = 0.1	32.74
<i>BM08theory_5</i>	Ward3, Sigmaratio = 0.2	62.96
<i>BM08theory_6</i>	Ward8, Sigmaratio = 0.3	75.62
<i>BM08theory_7</i>	Ward3, Sigmaratio = 0.2	14.11
<i>BM08theory_8</i>	Ward3, Sigmaratio = 0.2	60.83
<i>BM08theory_9</i>	-	-
<i>BM08theory_10</i>	-	-

List of calculations, which were closest to the simulation rate for each simulation. This table corresponds to Fig. 5.23

Considering the eccentricities leads to the same conclusion as the simulations without the BM08 module. All calculations provide a rate with the wrong sign. Therefore, no table will be provided.

The two presented analyses of the rate at one location and the behaviour are brought together for a complete picture. As seen with the *theory* setup, for low viscosities, the use of  $D_p$  as well as the consideration of higher Fourier orders, no calculation gives an adequate result. As before, the rates which are compared to the migration behaviour in this Section are only the ones which had the correct sign.

When comparing both analyses done for the LR location given by  $D$ , over half of the rates did not show a matching migration behaviour. Only for *BM08theory\_5* two analyses matched, while for *BM08theory\_8* at least the sign of Ward8 with  $\text{Sigmaratio} = 0.1$  at one location is coherent with the overall migration behaviour. For three other calculations the direction also matched the rate at one location, but they are scattered over different simulation setups. The usage of  $D_K$  on the contrary led to a matching migration direction in more than half of the calculations. A fully coherent analysis was only provided by *BM08theory\_4* and *BM08theory\_5*. In general, for all LR location equations more calculations had the right sign at one location then there were calculations with a fitting migration behaviour, or even direction. For the locations by  $D_{*,p}$ , a similar result is observed. The setups *BM08theory\_4* and *BM08theory\_5* had coherent analyses, while for most other calculations even the migration direction does not match.

Hence,  $D_{*,p}$  and  $D_K$  inserted into Ward3 give the best results again. For them, the deviation in percentage is plotted for all simulations in Fig. 5.24 and Fig. 5.25.

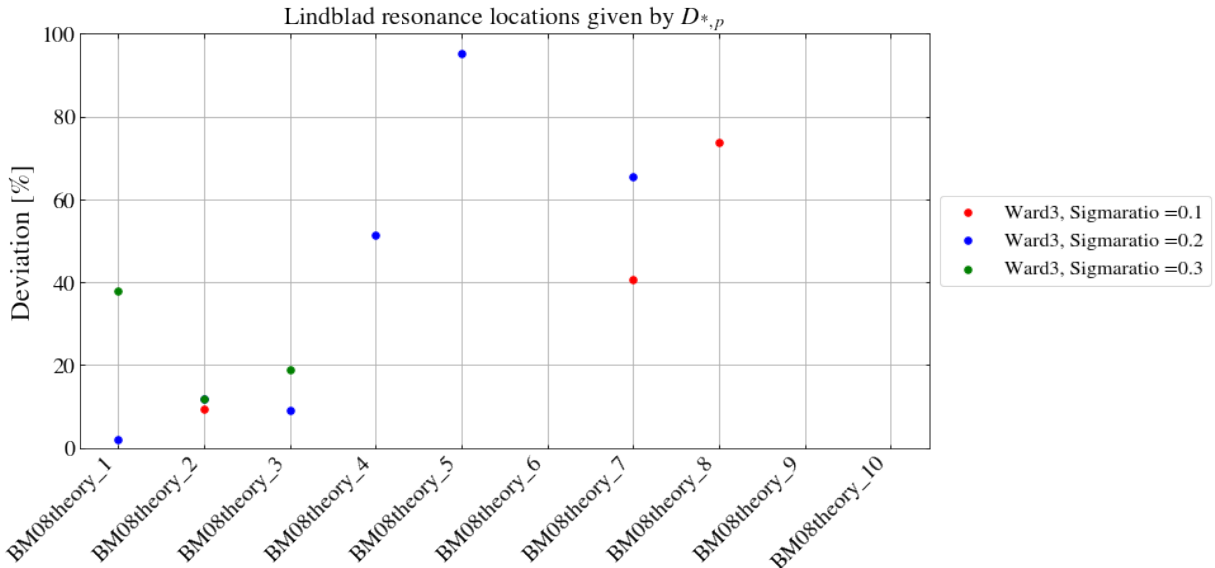


Figure 5.24: Deviation of the calculated migration rate in percentage from each simulation. Only the ones where Ward3 was used and which had the right sign are shown. The labels give the torque and Sigmaratio used in each calculation.

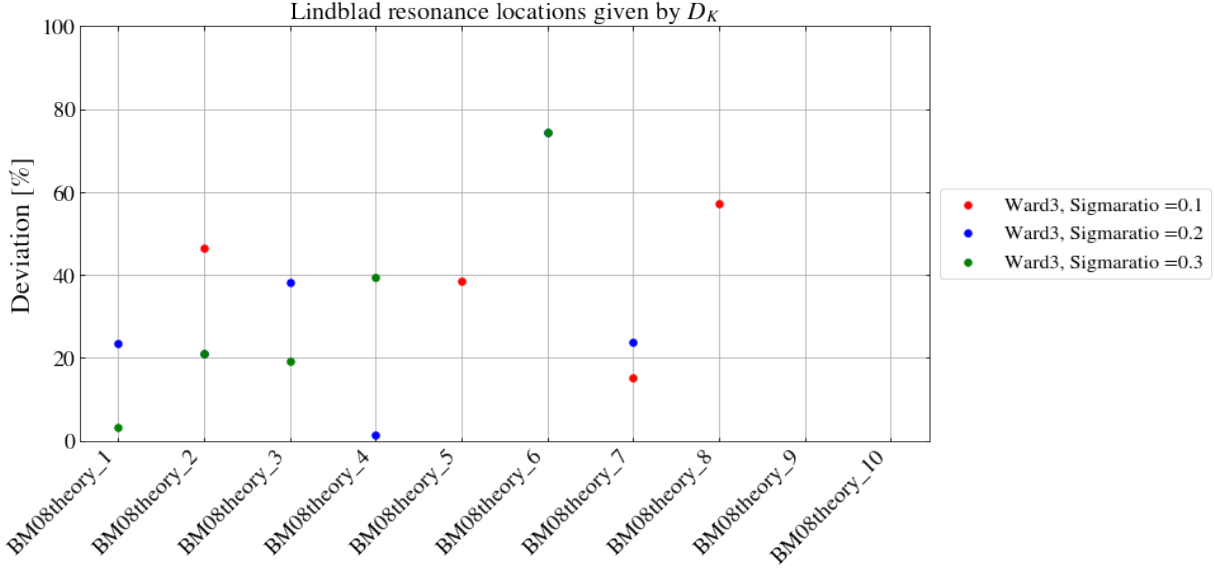


Figure 5.25: Deviation of the calculated migration rate in percentage from each simulation. Only the ones where Ward3 was used and which had the right sign are shown. The labels give the torque and Sigmaratio used in each calculation.

# Discussion and Outlook

In this section, the implications of the comparison between the theoretical approach and the hydrodynamic simulations and the limitations are discussed. The discussion starts with the comparison of the overall migration behaviour with and without the module BM08 (Sect. 5.1.1 and Sect. 5.2.1). Then, the comparison of the migration rate at one given locations for all simulations follows, (Sect. 5.1.2 and Sect. 5.2.1).

In general, the planets were mostly locked in a 2:1 MMR even though a 3:2 MMR predicted by [Masset and Snellgrove \[2001\]](#). Since this work's simulations are different in their boundary condition, smoothing, time the planets develop their gap, the planets in this work migrate more slowly and therefore can be caught in a 2:1 MMR. Additionally [Masset and Snellgrove \[2001\]](#) used FARGO, while FARGO3D was used in this work.

## 6.1 Migration behavior

The simulations with and without the BM08 module migrate outwards, as predicted by the Masset and Snellgrove mechanism. Most disks in the simulations without the module had become elliptic, which made the planets more eccentric and led to a close encounter. The planets became in general eccentric because the LR resonances lead to an eccentricity growth. Therefore, they were less in MMR and consequently less sections of the simulations can be compared to the theoretical approach. In contrary, the disk remained mostly stable with the BM08 module, since the influence of the IndirectTerm is weakened, as not the whole surface density was used to calculate the force. Many simulations experience one or more migration jumps, hence the outer planet was in the regime of Type III migration. The perturbed surface density due to the common gap also enabled the Type III migration [[Kley and Nelson, 2012](#)]. The planets experience less jumps with the module and migrate in general with higher rates. Overall, the theoretical approach predicts less fitting migration behaviours, but quite few fitting migration directions, for the simulations with the BM08 module, even though the planets had less close encounters and stayed longer in MMR without disturbances. This may be due to non linear effects,

which are not considered in the theoretical approach, like the eccentricity, which add up over the course of the simulations. Hence the beginning and direction of the migration can be predicted correctly by the theoretical model. For the simulations without the BM08 module, also quite a few calculations could predict the correct migration behaviour even more often than with the Module. Here, even though non-linear effects also add up over the course of the simulations, the behaviour could still be predicted for certain simulations.

Analyzing the migration behaviour for different LR locations in combination with different torques, the LR locations given by  $D_p$  and the torque GT79 with higher orders of  $l$  did not give similar results as the simulations. First,  $D_p$  only considers the disk pressure's effect on the orbital frequency and not on the epicyclic frequency. Figure 2.2 shows that the inner resonances of  $D_p$  are closest to the planet. Therefore, less inner torques contributed to the net torque, since more were cut off by the gap. Consequently, the migration rate favored inwards migration. While  $D_p$  leads to an underestimation of the inner, GT79 with higher orders of  $l$  leads to an overestimation of the outer torques. The reason is partially given by the behaviour of the second order derivative of the Laplace coefficients. It diverges and consequently the torque contributions can grow very large for close LR locations. GT79 uses the locations given by Eq. (2.21). For  $l = m - 1$ , which contribute to the outer LR, the resonances are located closer to the planet as for  $l = m + 1$  which contribute to the inner LR. Both are, compared to other LR locations, farthest away from the planet, so a cutting off by the gap is most likely not the cause of the torque imbalance. Hence, the closer resonance locations paired with the diverging second order derivative of the Laplace coefficients was probably the reason why the outer torques were overestimated so much. Furthermore, the usage of GT79 did not fulfil the condition  $m \ll \frac{\Omega r}{c}$  given by [Goldreich and Tremaine \[1980\]](#), and hence it was to be expected that GT79 would not give the right predictions with and without higher orders of  $l$  most of the time.

As for the usage of  $D$ , the behaviour of the migration rates can be occasionally similar but only when using the torque Ward8. This applies to the simulations with as well as without the module. Since  $D$  does not take the effects of the gas pressure into account, it does not fit the physical conditions simulations very well. The LR locations are very close to the planet, as can be observed in Fig. 2.1 - Fig. 2.4. Consequently, it is not surprising that only a few calculations managed to predict the right migration behaviour. Nevertheless, it is very interesting that the approximated torque equation, Ward8, may correct some parts of the flawed LR locations by  $D$ .

The usage of  $D_{*,p}$  and  $D_K$  led to very similar results, even though  $D_K$  did only partially

take the disk pressure into account. Hence, the more important correction of the disk pressure had to be the change of the epicycle frequency. The orbital frequency correction also changed the outcome of the theoretical approach, but the difference between  $D_{*,p}$  and  $D_K$  when inserted in Ward3 is rather small. In contrary to the usage of  $D$  and  $D_{*,p}$ , the torque equation Ward8 gives no matching results when combined with  $D_K$  and  $D_p$ .

All LR locations could not give the right sign of the migration rate for the simulations with lower viscosities. For low viscosities additional effects appear, and therefore the theoretical model for a viscous disk this work is based upon cannot provide the correct direction of migration.

Surprisingly, for both simulation types, the insertion of  $D_K$  into GT79 managed to predict the right behaviour, even though the conditions for the usage of GT79 are not met.

## 6.2 Migration rate at one locations

Using the same reasoning why  $D_p$  and GT79 with higher orders of  $l$  didn't predict the migration rates direction correctly, the rate at one point also always had the wrong direction. Interestingly, with the usage of  $D_K$ , GT79 did predict the right direction at one point a few times, even being the best calculation when compared to *theory\_8*. The reasoning is the same as above.

While  $D$  does not consider the gas pressure, the combination with may Ward8 yield the right migration direction. Furthermore, an average deviation of the actual rate around 80% is not good, but one could expect it to perform much worse.

In contrary,  $D_K$  and  $D_{*,p}$  again gave the best approximations while inserted into Ward3, even up to only a few percentage deviation. This is surprising, because the theoretical approach can't consider different effects like vortexes, migrating jumps etc which happen in the simulations. Similarly to the migration behaviour,  $D_K$  inserted into Ward8 never gave the correct sign of the rate at one point.

For lower viscosities of  $\alpha = 10^{-4}$  or  $10^{-5}$ , the disks get inviscid or are close to. Then, more effects appear which influence the migration like vortexes. Furthermore, ignoring self-gravity, which is an inconsistency in itself because a planet feels disk potential but a disk does not feel its own, gets more important for lower viscosities . Hence, it is not surprising that a theory derived for a viscous disk is not capable of describing this very

complicated behaviour.

Finally, the theoretical model could then be used to predict the migration behaviour of existing planetary systems for specific sets of physical parameters. Especially the combination of  $D_K$  and  $D_{*,p}$  with Ward3 give results, that sometimes only deviate a few percentage from the simulations. For both sets of simulations with and without the BM08 module, the rates from  $D_K$  and  $D_{*,p}$  are compared in Fig. 6.1 and Fig. 6.2.

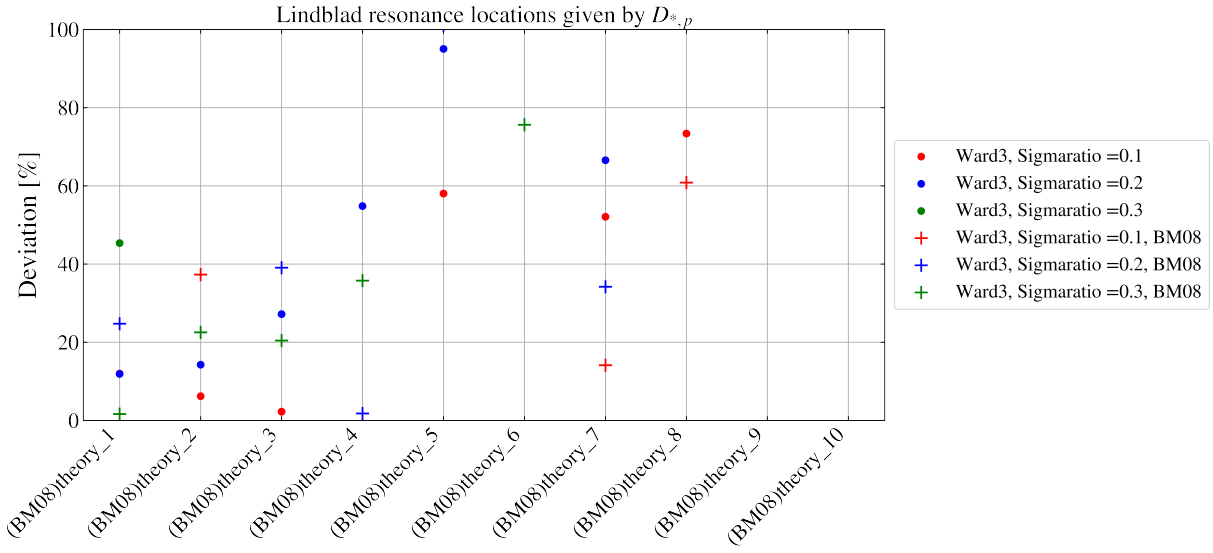


Figure 6.1: Deviation of the calculated migration rate in percentage from each simulation. Only the ones where Ward3 was used and which had the right sign are shown. The labels give the torque and Sigmaratio used in each calculation, as well as if the BM08 module was used.

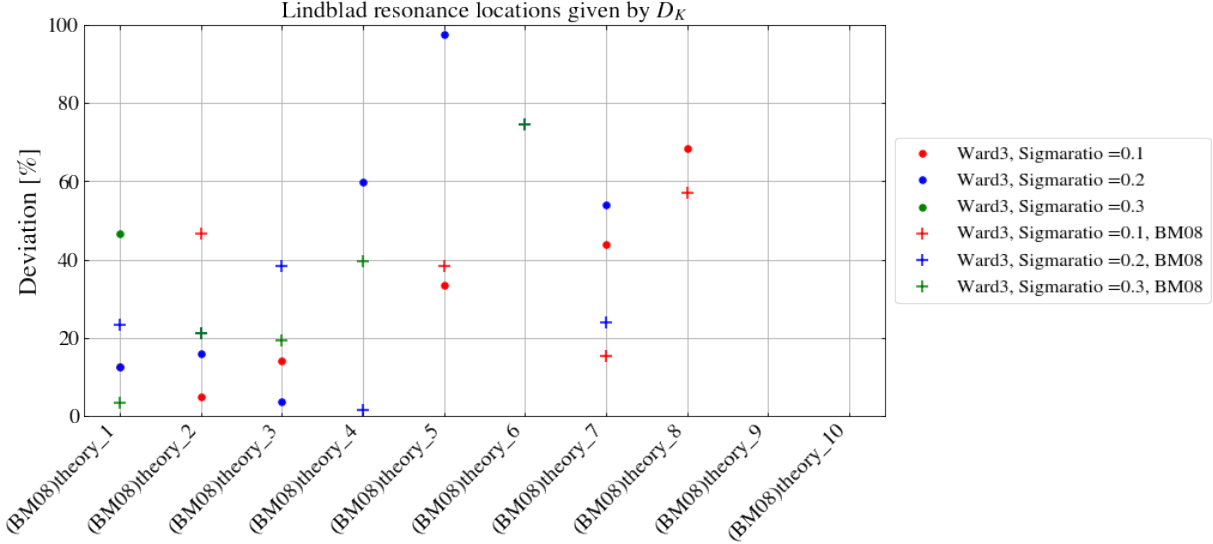


Figure 6.2: Deviation of the calculated migration rate in percentage from each simulation. Only the ones where Ward3 was used and which had the right sign are shown. The labels give the torque and Sigmaratio used in each calculation, as well as if the BM08 module was used.

As seen when comparing the migration rates in Fig. 6.1 and Fig. 6.2, it is observed that the for the simulations with the BM08 module the rates are more often closer to the simulated rate. This is very interesting, because the migration behaviour was less fitting for the simulations with the BM08 module. Therefore in early phases of the simulations, where the migration rates were measured, the theoretical approach can predict the migration rates better for simulations with the BM08 module but the behaviour at the end of the simulations are not predicted as well. This also strengthens the theory, that non linear effects add up over the simulations, leading to outcomes which were not predicted by the theoretical approach.

It also has to be added, that further progress was made relating shape of the gap of massive planets. Duffell [2020] proposed a numerical model which approximates the shape of gaps opened by massive planets more exact than the analytical model proposed by Kanagawa et al. [2017]. While Kanagawa et al. [2017] proposed an expression derived by theoretical calculations, Duffell [2020] measured the gap depth and width continuously while increasing the mass ratio  $q$  adiabatically and used these derived expressions to create a scaling factor. Furthermore, the effects of dust are not included in this analysis.

The next steps would also include a rewriting of the code, so that an evolution of the semimajor axis as a function of time can be calculated. Up to this point, the migration

rate is only given as a function of  $r_p$ , which allows the analysis of the migration behaviour but not to the extend as when the semimajor axis is given as a function of time. Additionally, simulations with an even higher resolution can be started, which could effect the semimajor axe's evolution.

# Summary

In this thesis, a theoretical model for the prediction of the migration behaviour of two large planets migrating outwards using the Masset and Snellgrove mechanism was introduced. For this, different expressions for the LR and the torques exerted at these planets were combined. Further, the gap which the planets open is described by the Kanagawa model [Kanagawa et al., 2017]. With this model, a range of depths at which torques were cut off was determined. Additionally the cutoff of the LR locations proposed by Goldreich and Tremaine [1979] was considered. Lastly, the torques were weighted with the dimensionless surface density model by Kanagawa et al. [2017], before getting the net torque of the planets while they are in MMR. This gave the author 48 possible combinations of the torque, LR location, eccentricity and gap depth were a cutoff would occur. These calculations were compared to simulations ran with FARGO3D, to test their validity.

One set of simulations was run with the BM08 module. This changed the torques exerted on the planet significantly and but theoretical model could predict more often the migration rates at one point but the overall behaviour less correctly. Additionally for simulations without the BM08 module, especially the LR location  $D_{*,p}$  and  $D_K$  gave good predictions, which even sometimes only differed a few percentage from the actual rates of the hydrodynamics simulations. The migration behaviour for the simulations without the BM08 module could be predicted more often than with the module. Using GT79 did not lead to the correct migration behaviour or rate, which indicates that the condition proposed by Goldreich and Tremaine [1980],  $m \ll \frac{\Omega r}{c} = \frac{1}{h}$ , is very important for the usage of GT79, especially when considering higher orders of  $l$ . Without considering the disk pressure, the LR locations obtained by  $D$  could give the right behaviour a few times but only when using the approximated torque Ward8. Nevertheless, the rates at one location were much further off as when using the LR locations  $D_{*,p}$  and  $D_K$  and also the general behaviour was predicted correctly less often. Lastly, the LR location  $D_p$  always gave the wrong migration direction, hence only the consideration of the orbital frequency correction due to the disk pressure alone contributes less to the right migration behaviour than the consideration of the change of the epicyclic frequency.

All in all, the theoretical model can be further improved by using another migration rate [Kanagawa et al., 2018], a better gap model for deep gaps [Duffell, 2020] and simulations with a higher resolution. Additionally, plotting the semimajor axis as a function of time instead of the migration rate as a function of  $r_p$  would further improve the capability to compare the migration behaviour with the simulations.

# Appendix A

The information for this section is taken from [Rometsch \[2022\]](#) if not stated otherwise.

The angular momentum of a single planet is given by

$$L_p = M_p \sqrt{GM_* a_p (1 - e_p^2)} . \quad (8.1)$$

If the eccentricity is negligible, Eq. (8.1) can be written as

$$L_p = M_p \sqrt{GM_* a_p} . \quad (8.2)$$

If the systems contains two or several planets, which are resonant locked, then only one planet semimajor axis is needed to calculate the position of all other resonant locked planets:

$$a_i = a_1 \gamma_i = a_1 \prod_{j=1}^{i-1} \left( \frac{p_j + q_j}{p_j} \right)^{2/3} \quad (8.3)$$

with the integers  $p$  and  $q$  and the mass ratio  $\mu = M_p/M_*$ . Hence

$$L_{\text{tot}}^{\text{circ}} = \sqrt{a_1} \sqrt{GM_*^3} \sum_{i=1}^{N_{pl}} \mu_i \sqrt{\gamma_i} \quad (8.4)$$

gives the angular momentum of the resonant locked system. For two planets  $L$  is

$$L_{\text{tot}}^{\text{circ}} = \sqrt{a_1} \sqrt{GM_*} M_1 (1 + \mu_2 \sqrt{\gamma_2}) . \quad (8.5)$$

The approximation of  $M_1 (1 + \mu_2 \sqrt{\gamma_2}) \sim (M_1 + M_2)$  only deviates from the exact from about 6%. By taking the derivative  $L_{\text{tot}}^{\text{circ}} / dt = \Gamma$  of the approximated angular momentum and rewriting it, the migration rate for two planets can be received:

$$\dot{a}_p = \frac{2 \Gamma_{LR,all}}{\Omega_p a_p (M_{p,inner} + M_{p,outer})} . \quad (8.6)$$

# Appendix B

The angular momentum of a planet neglecting the eccentricity is given by

$$L_p = M_p \sqrt{GM_* a_p}. \quad (9.1)$$

The torque is then defined as

$$\Gamma \equiv \dot{L}_p = \frac{1}{2} M_p \sqrt{\frac{GM_*}{a_p}} \dot{a} = \frac{1}{2} M_p \sqrt{\frac{GM_*}{a_p^3}} a \dot{a} \quad (9.2)$$

which can be reordered

$$\dot{a}_p = \frac{2\Gamma}{\Omega_p a_p (M_p)} \quad (9.3)$$

with the definition of  $\Omega_p$  in Eq. (2.2).

# Appendix C

In this section, the tables for the comparison of the migration development from the theoretical approach to the simulations are listed. To keep a clear structure, the following symbols are introduced:

- ✓ the migration direction matches the one from the simulation
- ✗ the migration direction does not match the one from the simulation
- the migration stopped in the simulations but did not stop in the theoretical approach
- the migration stopped in the theoretical approach but did not stop in the simulations
- ⚡ a close encounter occurred in the simulations
- ↷ a migration jump or several occurred in the simulations

For the LR locations given by  $D_p$  as well for the consideration of higher orders of Fourier components, the migration development given by the python script never matched the observed development in the simulations, for both simulations with and without the BM08 module. The predicted migration direction was always towards the star. Hence, no tables are provided for them.

Table 10.1: Resonance locations given by  $D$ 

name	Sigmaratio	Ward3	Ward8	GT79	simulation
<i>theory_1</i>	0.1	✗	✗	✗	outward migration, ↴ around $r_{in} = 2.3 r_0$
	0.2	✗	✓, ●	✗	
	0.3	✗	✓	✗	
<i>theory_2</i>	0.1	✗	✗	✗	outward migration, ↴ around $r_{in} = 3 r_0$
	0.2	✗	✓	✗	
	0.3	✗	✗	✗	
<i>theory_3</i>	0.1	✗	✗	✗	outward migration, ↴ around $r_{in} = 2.4 r_0, \curvearrowright$
	0.2	✗	✓, ●	✗	
	0.3	✗	✗	✗	
<i>theory_4</i>	0.1	not clear	✗	✗	outward migration, ↴ around $r_{in} = 2.1 r_0, \curvearrowright$
	0.2	✗	not clear	✗	
	0.3	✗	✓	✗	
<i>theory_5</i>	0.1	✗	✓	✗	still migrating outwards at $r_{in} = 1.3 r_0$
	0.2	✗	✓	✗	
	0.3	✗	✗	✗	
<i>theory_6</i>	0.1	✗	✓	✗	outward migration, ↴ around $r_{in} = 2.6 r_0, \curvearrowright$
	0.2	✗	✗	✗	
	0.3	✗	✗	✗	
<i>theory_7</i>	0.1	✗	✓	✗	outward migration, ↴ around $r_{in} = 2.1 r_0, \curvearrowright$
	0.2	✓, ●	✓	✗	
	0.3	✗	✗	✗	
<i>theory_8</i>	0.1	✗, ○	✓, ○	✗, ○	migration stopped at $r_{in} = 2.045 r_0$
	0.2	✗, ○	✗, ○	✗, ○	
	0.3	✗, ○	✗, ○	✗, ○	
<i>theory_9</i>	0.1	✗	✗	✗	outward migration, ↴ around $r_{in} = 1.5 r_0, \curvearrowright$
	0.2	✗	✗	✗	
	0.3	✗	✗	✗	
<i>theory_10</i>	0.1	✗	✗	✗	still migrating outwards at $r_{in} = 1.3 r_0$
	0.2	✗	✗	✗	
	0.3	✗	✗	✗	

In the columns with the torque equation name, it is written down how the general behaviour of the migration was for the given LR location inserted into the torque equation. Since Sigmaratio was a free parameter, each calculation was done for the ratios 0.1, 0.2 and 0.3. In the column simulations, the outcome of the simulations is briefly described.

Table 10.2: Resonance locations given by  $D_{*,p}$ 

name	Sigmaratio	Ward3	Ward8	GT79	simulation
<i>theory_1</i>	0.1	✓	✗	✗	outward migration, ↴ around $r_{in} = 2.3 r_0$
	0.2	✓	✓, ●	✗	
	0.3	✗	✗	✗	
<i>theory_2</i>	0.1	✓	✗	✗	outward migration, ↴ around $r_{in} = 3 r_0$ , ↗
	0.2	✓	✓	✗	
	0.3	✗	✗	✗	
<i>theory_3</i>	0.1	✓	✗	✗	outward migration, ↴ around $r_{in} = 2.4 r_0$ , ↗
	0.2	✓	✓, ●	✗	
	0.3	✗	✗	✗	
<i>theory_4</i>	0.1	✓	✓	✗	outward migration, ↴ around $r_{in} = 2.1 r_0$ , ↗
	0.2	✓	not clear	✗	
	0.3	✓	✓	✗	
<i>theory_5</i>	0.1	✓	✗	✗	still migrating outwards at $r_{in} = 1.3 r_0$
	0.2	✓	✓	✗	
	0.3	✗	✗	✗	
<i>theory_6</i>	0.1	✓	✓, ●	✗	outward migration, ↴ around $r_{in} = 2.6 r_0$ , ↗
	0.2	✓, ●	✗	✗	
	0.3	✓, ●	✗	✗	
<i>theory_7</i>	0.1	✓	✓, ●	✗	outward migration, ↴ around $r_{in} = 2.1 r_0$ , ↗
	0.2	✓	✓	✗	
	0.3	✗	✗	✗	
<i>theory_8</i>	0.1	✓, ○	✓, ○	✗, ○	migration stopped at $r_{in} = 2.045 r_0$
	0.2	✗, ○	✗, ○	✗, ○	
	0.3	✗, ○	✗, ○	✗, ○	
<i>theory_9</i>	0.1	✗	✗	✗	outward migration, ↴ around $r_{in} = 1.5 r_0$ , ↗
	0.2	✗	✗	✗	
	0.3	✗	✗	✗	
<i>theory_10</i>	0.1	✗	✗	✗	still migrating outwards at $r_{in} = 1.3 r_0$
	0.2	✗	✗	✗	
	0.3	✗	✗	✗	

In the columns with the torque equation name, it is written down how the general behaviour of the migration was for the given LR location inserted into the torque equation. Since Sigmaratio was a free parameter, each calculation was done for the ratios 0.1, 0.2 and 0.3. In the column simulations, the outcome of the simulations is briefly described.

Table 10.3: Resonance locations given by  $D_K$ 

name	Sigmaratio	Ward3	Ward8	GT79	simulation
<i>theory_1</i>	0.1	✓	✗	✗	outward migration, ↴ around $r_{in} = 2.3 r_0$
	0.2	✓	✗	✗	
	0.3	✗	✗	✗	
<i>theory_2</i>	0.1	✓	✗	✗	outward migration, ↴ around $r_{in} = 3 r_0$ , ↗
	0.2	✓	✗	✗	
	0.3	✗	✗	✗	
<i>theory_3</i>	0.1	✓	✗	✗	outward migration, ↴ around $r_{in} = 2.4 r_0$ , ↗
	0.2	✓	✗	✗	
	0.3	✗	✗	✗	
<i>theory_4</i>	0.1	✓	✗	✓	outward migration, ↴ around $r_{in} = 2.1 r_0$ , ↗
	0.2	✓	✗	✗	
	0.3	✓	✗	✗	
<i>theory_5</i>	0.1	✓	✗	✗	still migrating outwards at $r_{in} = 1.3 r_0$
	0.2	✓	✗	✗	
	0.3	✗	✗	✗	
<i>theory_6</i>	0.1	✓	✗	✓, ●	outward migration, ↴ around $r_{in} = 2.6 r_0$ , ↗
	0.2	✓, ●	✗	✗	
	0.3	✓	✗	✗	
<i>theory_7</i>	0.1	✓	✗	✓, ●	outward migration, ↴ around $r_{in} = 2.1 r_0$ , ↗
	0.2	✓	✗	✗	
	0.3	✗	✗	✗	
<i>theory_8</i>	0.1	✓, ○	✗, ○	✓, ○	migration stopped at $r_{in} = 2.045 r_0$
	0.2	✗, ○	✗, ○	✗, ○	
	0.3	✗, ○	✗, ○	✗, ○	
<i>theory_9</i>	0.1	✗	✗	✗	outward migration, ↴ around $r_{in} = 1.5 r_0$ , ↗
	0.2	✗	✗	✗	
	0.3	✗	✗	✗	
<i>theory_10</i>	0.1	✗	✗	✗	still migrating outwards at $r_{in} = 1.3 r_0$
	0.2	✗	✗	✗	
	0.3	✗	✗	✗	

In the columns with the torque equation name, it is written down how the general behaviour of the migration was for the given LR location inserted into the torque equation. Since Sigmaratio was a free parameter, each calculation was done for the ratios 0.1, 0.2 and 0.3. In the column simulations, the outcome of the simulations is briefly described.

Table 10.4: Resonance locations given by  $D$ 

name	Sigmaratio	Ward3	Ward8	GT79	simulation
<i>BM08theory_1</i>	0.1	✗, ○	✗, ○	✗, ○	outwards migration stopped at $r_{in} = 1.84 r_0$ , starting $\curvearrowright$ 5000 orbits after
	0.2	✗, ○	✗, ○	✗, ○	
	0.3	✗, ○	✓, ○	✗, ○	
<i>BM08theory_2</i>	0.1	✗, ○	✗	✗, ○	outwards migration stopped at $r_{in} = 1.724 r_0$ , $\curvearrowright$
	0.2	✗, ○	✓, ○	✗, ○	
	0.3	✗, ○	✗	✗, ○	
<i>BM08theory_3</i>	0.1	✗, ○	✗	✗, ○	outwards migration stopped at $r_{in} = 1.788 r_0$ , $\curvearrowright$
	0.2	✗, ○	(✓), ● at 1.75	✗, ○	
	0.3	✗, ○	✗	✗, ○	
<i>BM08theory_4</i>	0.1	not clear	✓	✗	
	0.2	✗	not clear	✗	outward migration, ↴ around $r_{in} = 1.6 r_0$
	0.3	✗	✓	✗	
<i>BM08theory_5</i>	0.1	✗	✗	✗	
	0.2	✗	✓	✗	still migrating outwards at $r_{in} = 1.3 r_0$
	0.3	✗	✗	✗	
<i>BM08theory_6</i>	0.1	✗	✗	✗	outward migration, then inward migration, ↴ around $r_{in} = 2.6 r_0$ , $\curvearrowright$
	0.2	✗	✗	✗	
	0.3	✗	✗	✗	
<i>BM08theory_7</i>	0.1	✗, ○	✓, ○	✗, ○	
	0.2	✓, ●	✓, ○	✗, ○	outward migration stopped at $r_{in} = 2.015 r_0$
	0.3	✗, ○	✗, ○	✗, ○	
<i>BM08theory_8</i>	0.1	✗, ○	✓, ○	✗, ○	
	0.2	✗, ○	✗, ○	✗, ○	outward migration stopped at $r_{in} = 2.050 r_0$ , $\curvearrowright$
	0.3	✗, ○	✗, ○	✗, ○	
<i>BM08theory_9</i>	0.1	✗	✗	✗	outward migration, then inward migration, ↴ around $r_{in} = 1.67 r_0$ , $\curvearrowright$
	0.2	✗	✗	✗	
	0.3	✗	✗	✗	
<i>BM08theory_10</i>	0.1	✗	✗	✗	
	0.2	✗	✗	✗	still migrating outwards at $r_{in} = 2.178 r_0$ , $\curvearrowright$
	0.3	✗	✗	✗	

In the columns with the torque equation name, it is written down how the general behaviour of the migration was for the given LR location inserted into the torque equation. Since Sigmaratio was a free parameter, each calculation was done for the ratios 0.1, 0.2 and 0.3. In the column simulations, the outcome of the simulations is briefly described.

Table 10.5: Resonance locations given by  $D_{*,p}$ 

name	Sigmaratio	Ward3	Ward8	GT79	simulation
<i>BM08theory_1</i>	0.1	✓, ○	✗, ○	✗, ○	outwards migration
	0.2	✓, ○	✓, ● earlier	✗, ○	stopped at $r_{in} = 1.84 r_0$ , starting $\sim 5000$ orbits after
	0.3	✗, ○	✗, ○	✗, ○	
<i>BM08theory_2</i>	0.1	✓, ○	✗, ○	✗, ○	outwards migration
	0.2	✓, ○	✓, ○	✗, ○	stopped at $r_{in} = 1.724 r_0$ , $\sim$
	0.3	✗, ○	✗, ○	✗, ○	
<i>BM08theory_3</i>	0.1	✓, ○	✗, ○	✗, ○	outwards migration
	0.2	✓, ○	✓, ○	✗, ○	stopped at $r_{in} = 1.788 r_0$ , $\sim$
	0.3	✗, ○	✗, ○	✗, ○	
<i>BM08theory_4</i>	0.1	✓	✓	✗	
	0.2	✓	not clear	✗	outward migration, ↴ around $r_{in} = 1.6 r_0$
	0.3	✓	✓	✗	
<i>BM08theory_5</i>	0.1	✓	✗	✗	
	0.2	✓	✓	✗	still migrating outwards at $r_{in} = 1.3 r_0$
	0.3	✗	✗	✗	
<i>BM08theory_6</i>	0.1	✗	✗, ●	✗	
	0.2	✗	✗	✗	outward and then inward migration, ↴ around $r_{in} = 2.6 r_0$ , $\sim$
	0.3	✗	✗	✗	
<i>BM08theory_7</i>	0.1	✓, ○	✓, ● earlier	✗, ○	
	0.2	✓, ○	✓, ○	✗, ○	outward migration stopped at $r_{in} = 2.015 r_0$
	0.3	✗, ○	✗, ○	✗, ○	
<i>BM08theory_8</i>	0.1	✓, ○	✓, ○	✗, ○	
	0.2	✗, ○	✗, ○	✗, ○	outward migration stopped at $r_{in} = 2.050 r_0$ , $\sim$
	0.3	✗, ○	✗, ○	✗, ○	
<i>BM08theory_9</i>	0.1	✗	✗	✗	outward and then inward migration , ↴ around $r_{in} = 1.67 r_0$ , $\sim$
	0.2	✗	✗	✗	
	0.3	✗	✗	✗	
<i>BM08theory_10</i>	0.1	✗	✗	✗	
	0.2	✗	✗	✗	still migrating outwards at $r_{in} = 2.178 r_0$ , $\sim$
	0.3	✗	✗	✗	

In the columns with the torque equation name, it is written down how the general behaviour of the migration was for the given LR location inserted into the torque equation. Since Sigmaratio was a free parameter, each calculation was done for the ratios 0.1, 0.2 and 0.3. In the column simulations, the outcome of the simulations is briefly described.

Table 10.6: Resonance locations given by  $D_K$ 

name	Sigmaratio	Ward3	Ward8	GT79	simulation
<i>BM08theory_1</i>	0.1	✓, ○	✗, ○	✗, ○	outwards migration stopped at $r_{in} = 1.84 r_0$ , starting $\sim 5000$ orbits after
	0.2	✓, ○	✗, ○	✗, ○	
	0.3	✗, ○	✗, ○	✗, ○	
<i>BM08theory_2</i>	0.1	✓, ○	✗, ○	✗, ○	outwards migration stopped at $r_{in} = 1.724 r_0$ , $\curvearrowright$
	0.2	✓, ○	✗, ○	✗, ○	
	0.3	✗, ○	✗, ○	✗, ○	
<i>BM08theory_3</i>	0.1	✓, ○	✗, ○	✗, ○	outwards migration stopped at $r_{in} = 1.788 r_0$ , $\curvearrowright$
	0.2	✓, ○	✗, ○	✗, ○	
	0.3	✗, ○	✗, ○	✗, ○	
<i>BM08theory_4</i>	0.1	✓	✗	✓	outward migration, ↴ around $r_{in} = 1.6 r_0$
	0.2	✓	✗	✗	
	0.3	✓	✗	✗	
<i>BM08theory_5</i>	0.1	✓	✗	✗	still migrating outwards at $r_{in} = 1.3 r_0$
	0.2	✓	✗	✗	
	0.3	✗	✗	✗	
<i>BM08theory_6</i>	0.1	✗	✗	✗, ●	outward and then inward migration, ↴ around $r_{in} = 2.6 r_0$ , $\curvearrowright$
	0.2	✗, ●	✗	✗	
	0.3	✗, ●	✗	✗	
<i>BM08theory_7</i>	0.1	✓, ○	✗, ○	✓, ● earlier	outward migration stopped at $r_{in} = 2.015 r_0$
	0.2	✗, ○	✗, ○	✗, ○	
	0.3	✗, ○	✗, ○	✗, ○	
<i>BM08theory_8</i>	0.1	✓, ○	✗, ○	✓, ○	outward migration stopped at $r_{in} = 2.050 r_0$ , $\curvearrowright$
	0.2	✓, ○	✗, ○	✗, ○	
	0.3	✗, ○	✗, ○	✗, ○	
<i>BM08theory_9</i>	0.1	✗	✗	✗	outward and then inward migration, ↴ around $r_{in} = 1.67 r_0$ , $\curvearrowright$
	0.2	✗	✗	✗	
	0.3	✗	✗	✗	
<i>BM08theory_10</i>	0.1	✗	✗	✗	still migrating outwards at $r_{in} = 2.178 r_0$ , $\curvearrowright$
	0.2	✗	✗	✗	
	0.3	✗	✗	✗	

In the columns with the torque equation name, it is written down how the general behaviour of the migration was for the given LR location inserted into the torque equation. Since Sigmaratio was a free parameter, each calculation was done for the ratios 0.1, 0.2 and 0.3. In the column simulations, the outcome of the simulations is briefly described.

# Acknowledgements

First, I would like to thank Prof. Dr. Cornelis P. Dullemond for giving me the opportunity to write my thesis in his group, and for his constant support. Not only the meetings where he would answer all my questions helped me along, but also by encouraging me in my work he contributed greatly to my interest and motivation. Next, I would like to thank Thomas Rometsch, who guided me through my project and would not only answer my never ending questions regarding the physics of protoplanetary disk, but also helped me with my code, FARGO3D, and proofreading my thesis.

I would like to further thank Andrej Herrmann, for investing a lot of time to answer all my questions regarding FARGO3D, and how to improve my python code. Especially in the first weeks of my internship, it helped me to have a good and fast start into the group. Moreover I would like to thank the group for very warmly welcoming me. I would also like to thank Prof. Dr. Ralf S. Klessen for being the second examiner of this thesis.

Further I want to thank Marleen Maxton, Felix Waldherr and my mother for proofreading my thesis and giving helpful advice. Also my flatmates and family as well as my friends helped me during this time by supporting me, even though it was a very stressful time.

Additionally, I acknowledge support by the High Performance and Cloud Computing Group at the Zentrum für Datenverarbeitung of the University of Tübingen, the state of Baden-Württemberg through bwHPC and the German Research Foundation (DFG) through grant no INST 37/935-1 FUGG.

# Bibliography

Anaconda Software Distribution. <https://docs.anaconda.com/>, 2020.

Philip J. Armitage. *Astrophysics of Planet Formation*. Cambridge University Press, 2009.

C. Baruteau and F. Masset. Type I Planetary Migration in a Self-Gravitating Disk. *The Astrophysical Journal*, 678(1):483–497, may 2008. doi: 10.1086/529487. URL <https://doi.org/10.1086/529487>.

Pablo Benítez-Llambay and Frédéric S. Masset. FARGO3D: A New GPU-oriented MHD Code. *The Astrophysical Journal Supplement Series*, 223(1):11, 2016. URL <http://stacks.iop.org/0067-0049/223/i=1/a=11>.

Aurélien Crida, Frédéric Masset, and Alessandro Morbidelli. Long Range Outward Migration of Giant Planets, with Application to Fomalhaut b. *ApJ*, 705(2):L148–L152, November 2009. doi: 10.1088/0004-637X/705/2/L148.

Paul C. Duffell. An Empirically Derived Formula for the Shape of Planet-induced Gaps in Protoplanetary Disks. *ApJ*, 889(1):16, January 2020. doi: 10.3847/1538-4357/ab5b0f.

Cornelis Petrus Dullemond. Theoretical Models of the Structure of Protoplanetary Disks Les Houches. <https://www.ita.uni-heidelberg.de/~dullemond/lectures/leshouches2013.pdf>, 2013. (accessed: 15.9.2022).

C.P. Dullemond and V. Springel. Lecture numerical fluid dynamics. [https://www.ita.uni-heidelberg.de/~dullemond/lectures/num\\_fluid\\_2009/Intro.pdf](https://www.ita.uni-heidelberg.de/~dullemond/lectures/num_fluid_2009/Intro.pdf), 2012/13.

Simon Glover. Accretion disks. [https://www.ita.uni-heidelberg.de/~mattia/teaching/accretion\\_disks.pdf](https://www.ita.uni-heidelberg.de/~mattia/teaching/accretion_disks.pdf), 2017. (accessed: 14.08.2022).

Philip W. Goetz. *The New Encyclopædia Britannica*. Chicago, Ill. : Encyclopædia Britannica, ©1991., 1991.

P. Goldreich and S. Tremaine. The excitation of density waves at the Lindblad and corotation resonances by an external potential. *ApJ*, 233:857–871, November 1979. doi: 10.1086/157448.

## BIBLIOGRAPHY

---

P. Goldreich and S. Tremaine. Disk-satellite interactions. *ApJ*, 241:425–441, October 1980. doi: 10.1086/158356.

Charles R. Harris, K. Jarrod Millman, Stéfan J. van der Walt, Ralf Gommers, Pauli Virtanen, David Cournapeau, Eric Wieser, Julian Taylor, Sebastian Berg, Nathaniel J. Smith, Robert Kern, Matti Picus, Stephan Hoyer, Marten H. van Kerkwijk, Matthew Brett, Allan Haldane, Jaime Fernández del Río, Mark Wiebe, Pearu Peterson, Pierre Gérard-Marchant, Kevin Sheppard, Tyler Reddy, Warren Weckesser, Hameer Abbasi, Christoph Gohlke, and Travis E. Oliphant. Array programming with NumPy. *Nature*, 585(7825):357–362, September 2020. doi: 10.1038/s41586-020-2649-2. URL <https://doi.org/10.1038/s41586-020-2649-2>.

J. D. Hunter. Matplotlib: A 2D graphics environment. *Computing in Science & Engineering*, 9(3):90–95, 2007. doi: 10.1109/MCSE.2007.55.

K. D. Kanagawa, H. Tanaka, T. Muto, T. Tanigawa, and T. Takeuchi. Formation of a disc gap induced by a planet: effect of the deviation from Keplerian disc rotation. *MNRAS*, 448(1):994–1006, March 2015. doi: 10.1093/mnras/stv025.

Kazuhiro D. Kanagawa, Hidekazu Tanaka, Takayuki Muto, and Takayuki Tanigawa. Modelling of deep gaps created by giant planets in protoplanetary disks. *PASJ*, 69(6):97, December 2017. doi: 10.1093/pasj/psx114.

Kazuhiro D. Kanagawa, Hidekazu Tanaka, and Ewa Szuszkiewicz. Radial Migration of Gap-opening Planets in Protoplanetary Disks. I. The Case of a Single Planet. *ApJ*, 861(2):140, July 2018. doi: 10.3847/1538-4357/aac8d9.

M. Keppler, R. Teague, J. Bae, M. Benisty, T. Henning, R. van Boekel, E. Chapillon, P. Pinilla, J. P. Williams, G. H. M. Bertrang, S. Facchini, M. Flock, Ch. Ginski, A. Juhasz, H. Klahr, Y. Liu, A. Müller, L. M. Pérez, A. Pohl, G. Rosotti, M. Samland, and D. Semenov. Highly structured disk around the planet host PDS 70 revealed by high-angular resolution observations with ALMA. *A&A*, 625:A118, May 2019. doi: 10.1051/0004-6361/201935034.

W. Kley and R. P. Nelson. Planet-Disk Interaction and Orbital Evolution. *ARA&A*, 50: 211–249, September 2012. doi: 10.1146/annurev-astro-081811-125523.

Thomas Kluyver, Benjamin Ragan-Kelley, Fernando Pérez, Brian Granger, Matthias Bussonnier, Jonathan Frederic, Kyle Kelley, Jessica Hamrick, Jason Grout, Sylvain Corlay, Paul Ivanov, Damián Avila, Safia Abdalla, and Carol Willing. Jupyter Notebooks – a publishing format for reproducible computational workflows. In F. Loizides and

- B. Schmidt, editors, *Positioning and Power in Academic Publishing: Players, Agents and Agendas*, pages 87 – 90. IOS Press, 2016.
- Maike Voelkel. The Kanagawa Models of Planetary Gaps in Protoplanetary Disks in Connection with Dust Traps. july 2022.
- F. Masset. FARGO: A fast eulerian transport algorithm for differentiallyrotating disks. *Astronomy and Astrophysics Supplement Series*, 141(1):165–173, January 2000. ISSN 0365-0138, 1286-4846. doi: 10.1051/aas:2000116. URL <http://aas.aanda.org/10.1051/aas:2000116>.
- F. Masset and M. Snellgrove. Reversing type II migration: resonance trapping of a lighter giant protoplanet. *MNRAS*, 320(4):L55–L59, February 2001. doi: 10.1046/j.1365-8711.2001.04159.x.
- F. S. Masset and J. C. B. Papaloizou. Runaway Migration and the Formation of Hot Jupiters. *ApJ*, 588(1):494–508, May 2003. doi: 10.1086/373892.
- F.S. Masset. On the Co-orbital Corotation Torque in a Viscous Disk and Its Impact on Planetary Migration. *ApJ*, 558(1):453–462, September 2001. doi: 10.1086/322446.
- Michel Mayor and Didier Queloz. A Jupiter-mass companion to a solar-type star. *Nature*, 378(6555):355–359, November 1995. doi: 10.1038/378355a0.
- T. W. A. Müller, W. Kley, and F. Meru. Treating gravity in thin-disk simulations. *A&A*, 541:A123, May 2012. doi: 10.1051/0004-6361/201118737.
- Sijme-Jan Paardekooper, Ruobing Dong, Paul Duffell, Jeffrey Fung, Frederic S. Masset, Gordon Ogilvie, and Hidekazu Tanaka. Planet-Disk Interactions. *arXiv e-prints*, art. arXiv:2203.09595, March 2022.
- A. Pierens and S. N. Raymond. Two phase, inward-then-outward migration of Jupiter and Saturn in the gaseous solar nebula. *A&A*, 533:A131, September 2011. doi: 10.1051/0004-6361/201117451.
- A. Pierens and S. N. Raymond. Migration of accreting planets in radiative discs from dynamical torques. *MNRAS*, 462(4):4130–4140, November 2016. doi: 10.1093/mnras/stw1904.
- Thomas Rometsch. The cells-per-scaleheight calculator. <https://rometsch.github.io/cps-calc/> (lastaccessed:20.08.2022). (accessed: 22.09.2022).
- Thomas Rometsch. The rigid resonant chain model. private communication, 2022.

## BIBLIOGRAPHY

---

- Thomas Rometsch, Peter J. Rodenkirch, Wilhelm Kley, and Cornelis P. Dullemond. Migration jumps of planets in transition discs. *A&A*, 643:A87, November 2020. doi: 10.1051/0004-6361/202038311.
- J. Schneider. The extrasolar planets encyclopedia. <http://exoplanet.eu/>, Feb 1995. (accessed: 8.9.2022).
- N. I. Shakura and R. A. Sunyaev. Black holes in binary systems. Observational appearance. *A&A*, 24:337–355, January 1973.
- M. De Val-Borro, R. G. Edgar, P. Artymowicz, P. Ciecielag, P. Cresswell, G. D'Angelo, E. J. Delgado-Donate, G. Dirksen, S. Fromang, A. Gawryszczak, H. Klahr, W. Kley, W. Lyra, F. Masset, G. Mellema, R. P. Nelson, S.-J. Paardekooper, A. Peplinski, A. Pierens, T. Plewa, K. Rice, C. Schafer, and R. Speith. A comparative study of disc-planet interaction. *Monthly Notices of the Royal Astronomical Society*, 370(2):529–558, aug 2006. doi: 10.1111/j.1365-2966.2006.10488.x. URL <https://doi.org/10.1111%2Fj.1365-2966.2006.10488.x>.
- Guido Van Rossum and Fred L. Drake. *Python 3 Reference Manual*. CreateSpace, Scotts Valley, CA, 2009. ISBN 1441412697.
- Pauli Virtanen, Ralf Gommers, Travis E. Oliphant, Matt Haberland, Tyler Reddy, David Cournapeau, Evgeni Burovski, Pearu Peterson, Warren Weckesser, Jonathan Bright, Stéfan J. van der Walt, Matthew Brett, Joshua Wilson, K. Jarrod Millman, Nikolay Mayorov, Andrew R. J. Nelson, Eric Jones, Robert Kern, Eric Larson, C J Carey, İlhan Polat, Yu Feng, Eric W. Moore, Jake VanderPlas, Denis Laxalde, Josef Perktold, Robert Cimrman, Ian Henriksen, E. A. Quintero, Charles R. Harris, Anne M. Archibald, Antônio H. Ribeiro, Fabian Pedregosa, Paul van Mulbregt, and SciPy 1.0 Contributors. SciPy 1.0: Fundamental Algorithms for Scientific Computing in Python. *Nature Methods*, 17:261–272, 2020. doi: 10.1038/s41592-019-0686-2.
- William R. Ward. Protoplanet Migration by Nebula Tides. *Icarus*, 126(2):261–281, April 1997. doi: 10.1006/icar.1996.5647.
- Williams, Jonathan P. and Cieza, Lucas A. Protoplanetary Disks and Their Evolution. *Annual Review of Astronomy and Astrophysics*, 49(1):67–117, 2011. doi: 10.1146/annurev-astro-081710-102548. URL <https://doi.org/10.1146/annurev-astro-081710-102548>.
- A. Wolszczan and D. A. Frail. A planetary system around the millisecond pulsar PSR1257 + 12. *Nature*, 355(6356):145–147, January 1992. doi: 10.1038/355145a0.

# Erklärung

Ich versichere, dass ich diese Arbeit selbstständig verfasst und keine anderen als die angegebenen Quellen und Hilfsmittel benutzt habe.

Heidelberg, den 29.9.2022,

K. Weishopf